UNIVERSITÀ DEGLI STUDI DI MILANO

SCUOLA DI DOTTORATO
FISICA, ASTROFISICA E FISICA APPLICATA

DIPARTIMENTO DI FISICA

CORSO DI DOTTORATO DI RICERCA IN
FISICA, ASTROFISICA E FISICA APPLICATA

CICLO XXIV

Pygmy structures in ^{208}Pb and ^{90}Zr studied with the inelastic scattering of ^{17}O at 20 MeV/u

Settore Scientifico disciplinare FIS/04

Tesi di Dottorato di:
Roberto Nicolini

Supervisore: Prof.sa Angela Bracco

Coordinatore: Prof. Marco Bersanelli

A.A. 2010-2011

Contents

Introduction

Over the last years, the evolution of nuclear structure as a function of the N/Z ratio has become a key question in nuclear physics. Indeed, various theoretical models predict in fact rather similar properties for nuclei close to the valley of stability, while a large disagreement is found for more exotic systems. For this reason the fundamental modes of excitation, vibrations and rotations, are studied in nuclei with growing N/Z asymmetry.

Special attention has been given to the vibrational modes of dipole nature: while most of the strength allowed by sum rule limits is absorbed by the Giant Dipole Resonance (GDR), nuclei with a neutron excess show an increase of dipole strength on the low-energy tail of the GDR, close to the neutron separation energy. This excess of dipole strength, of the order of ~1% of the Energy-Weighted Sum Rule (EWSR) in heavy stable nuclei and of ~10% in exotic neutron-rich nuclei, is possibly associated to a new type of collective motion, called Pygmy Dipole Resonance (PDR) because of the tiny strength it carries compared to the GDR.

The PDR is commonly described as a dipolar vibration of the excess neutrons against an N/Z symmetric core. This picture, well supported by the data, is the basis of several hydrodynamical models, and is consistent with the transition densities obtained through different microscopic approaches.

Nevertheless, various theoretical models disagree on the structure of the wave functions of the pygmy states, and thus on the interpretation of the mode. In particular, it is not obvious that the pygmy structures observed in neutron-rich stable nuclei and in exotic nuclei are really caused by the same mechanism. Furthermore, there is an ongoing debate on whether the PDR can really be seen as a collective mode: while most models agree that the pygmy states involve a large number of particle-hole configurations, the coherence of these configurations is still under discussion.

Besides being intrinsically interesting as new structure phenomena, the pygmy resonance is also expected to play an important role in nuclear astrophysics: it can be seen that the PDR significantly enhances the radiative neutron-capture cross section on neutron-rich nuclei, and this could have a pronounced effect on neutron-capture rates in the r-process nucleosynthesis, and on the calculated elemental abundance distribution.

From the experimental point of view, the PDR has been investigated systematically in a large number of stable nuclei with the photon scattering technique, because the electromagnetic interaction of gamma-rays is well understood, which allows model-independent derivation of absolute transition strengths, and because the method is very selective to E1 transitions. Information on the structure of the PDR in exotic nuclei has been obtained through relativistic Coulomb excitation reactions, in two experiments performed at GSI with ^{68}Ni and ^{132}Sn beams.

Both in stable and in exotic nuclei, however, the use of an electromagnetic probe allows only for the measurement of the transition strength of the resonance. In order to gain more insight in the structure of the PDR, it is necessary to obtain more explicit information also on wave functions and transition densities. To this end one needs to measure the PDR with reactions where the nuclear part of the interaction is involved. Indeed, the PDR states have been shown to possess a mixed nature regarding the isospin, meaning that they can be populated also by isoscalar probes.

This has been done in a series of recent experiments with inelastic scattering of alpha particles and the detection of the subsequent gamma decay from the target nucleus. These experiments, performed at the KVI laboratory on N=82 isotones, have shown a marked splitting of the PDR into two parts with different underlying structure: a low-lying component that is excited by using both alphas and gammas as probes, and a higher energy component that is excited only by the gammas. The low-energy component has been recognized as having a surface-peaked transition density and a predominantly isoscalar nature, while the high-energy component is interpreted as a GDR-like isovector oscillation.

In order to verify if this splitting is a common feature of the pygmy resonance, it is necessary to measure the PDR with isoscalar probes in different mass regions and

with different projectiles. For this reason, an experiment was performed in June 2010 at Legnaro National Laboratories, aimed at the study of highly excited states in the target nuclei, including the pygmy region and up to the giant resonance region.

The resonance states were populated by the inelastic scattering of a ^{17}O beam at the energy of 20 MeV/u, and their subsequent gamma decay was measured with the AGATA (Advanced GAmma-ray Tracking Array) Demonstrator, the new generation HPGe array based on the techniques of pulse shape analysis and gamma-ray tracking. The Demonstrator was coupled to an array of 3 large volume $LaBr_3$:Ce scintillators to increase the total efficiency; the remaining solid angle was covered by 20 BaF_2 scintillators. Two segmented ΔE-E Si telescopes were used to identify of the scattered beam ions and to measure the excitation energy transferred to the target nucleus.

The first aim of the experiment was the measurement of the well known case of the doubly-magic ^{208}Pb, which was studied in the past with the same technique but with a low-resolution detection setup. In contrast to the previous experiment, concentrating mainly on the gamma decay of the giant quadrupole resonance in the 10-13 MeV range, we focused on the measurement of the lower excitation energy region, where pygmy structures have been observed with the nuclear fluorescence technique. Our experiment is the first to successfully measure the gamma decay from pygmy states in ^{208}Pb with a different probe.

As a second case study, we measured the gamma decay from the pygmy region of a ^{90}Zr target, which can offer an important test to theoretical models as it is in a different mass region and with a smaller N/Z ratio, and is also semi-magic. Again, it is the first time that this nucleus is studied with a different probe.

Chapter 1. Giant resonances

As the main physics aim of the experiment described in this thesis is the measurement of the gamma decay from high-energy collective vibrational modes, the main properties of such states we will be recalled in this Chapter: in §1.1 the basic concepts concerning giant resonances are presented, while §1.2, §1.3 and §1.4 define some basic quantities regarding the strength of the resonances and their spatial distribution; §1.5 describes their decay mechanism. Finally, §1.6 focuses on a particular type of collective vibration, called the pygmy dipole resonance.

1.1. General features

Giant resonances are basic modes of excitation of nuclei, corresponding to a collective vibrational motion involving many if not all the nucleons. They are a well known example of the common feature of many-body quantum systems to form collective modes.

Their study over the years has provided useful information on nuclear structure and on the effective nucleon-nucleon interaction, as well as on the bulk properties of nuclear matter such as the compression modulus, the viscosity or the symmetry energy. Their main properties will be now recalled, following [1] and [2].

Giant resonances can be seen as high-frequency, damped, nearly elastic vibrations of the density or shape of the nuclear system around an equilibrium value. The vibration amplitude is small, only a few per cent of the nuclear radius. They can be described with a Lorentzian curve with 3 parameters: the energy E_R, the width Γ_R, and the strength S_R:

$$\sigma(E) = \frac{\sigma_m \Gamma_R^2 E^2}{(E^2 - E_R^2)^2 + \Gamma_R^2 E^2} \qquad (1.1)$$

where σ_m is the cross-section value at the maximum, related to the strength via a normalization factor.

Typically, the centroid energy of a giant resonance lies well above the neutron separation energy (8-10 MeV), with a corresponding vibration frequency of the order of 10^{21} Hz. The width of a giant resonance is of the order of 2-5 MeV, meaning that after only a few vibrations the resonance is completely damped. The strength of a giant resonance is limited by and generally close to the maximum allowed by sum rule considerations: it can in fact be shown that in many quantum systems the sum of all transition strengths for a given set of quantum numbers is limited by basic properties of the system, which would be for example the number of nucleons A and the atomic number Z in the case of a nuclear system.

Since a giant resonance is a collective motion of all nucleons, it is to be expected that its gross features do not depend on the detailed structure of the nucleus, but rather on its bulk structure. In fact, giant resonances of various nature have been observed over the years throughout the mass table, and the parameters of a given resonance have been shown to vary smoothly with the number of nucleons A. It should be noted, though, that the width of a giant resonance is also dependent on the microscopic structure of the nucleus, due to direct particle emission and to the coupling to more complex configurations (see §1.5).

1.1.1. CLASSIFICATION

The first evidence of a giant resonance excitation was found in 1937 in a measurement of the *(γ ,n)* cross-sections of various targets [3]. The phenomenon was interpreted by Goldhaber and Teller [4] and Steinwedel and Jensen [5] as a collective vibration where all the protons move against all the neutrons forming an oscillating electric dipole moment. It is now known that there are many other types of giant resonance, classified according to the multipolarity L, the spin S and the isospin T quantum numbers:

- Electric (ΔS=0) isoscalar (ΔT=0) vibrations where protons and neutrons oscillate in phase according to a multipole pattern defined by λ=0,2,…. To first order the λ=1 vibration corresponds to a translational motion of the nuclear centre of mass and is not an intrinsic excitation; however, there is a higher-order λ=1 vibration.
- Electric (ΔS=0) isovector (ΔT=1) vibrations where protons oscillate against neutrons. For the same multipolarity, isovector modes have a higher

excitation energy due to the extra energy required to separate the protons from the neutrons.

- Magnetic or spin-flip (ΔS=1) isoscalar (ΔT=0) modes where nucleons with spin up oscillate against nucleons with spin down
- Magnetic (ΔS=1) isovector (ΔT=1) modes where protons with spin up oscillate against neutrons with spin down and vice versa.

A schematic view of the various types of resonance for multipolarity λ=0,1,2 is shown in Fig. 1.1.

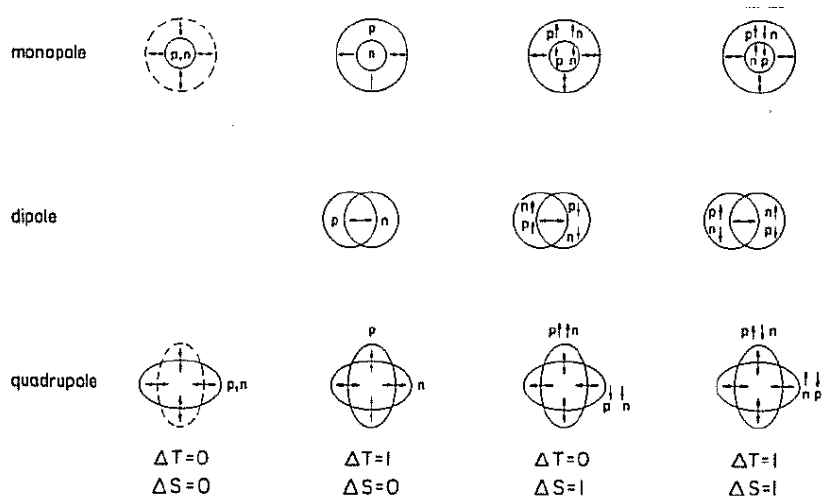

Fig. 1.1 Classification of giant resonances according to the multipolarity and to the spin and isospin quantum numbers, taken from [1].

1.1.2. MICROSCOPIC DESCRIPTION

From a microscopic point of view, giant resonances are commonly described as a coherent superposition of particle-hole excitations coupled to the same angular momentum, spin and isospin of the resonance. The giant resonance state can be seen as resulting from the operation on the ground state of the nucleus of a one-body operator:

$$|\Psi_{\mathrm{GR}}^{\lambda,\sigma,\tau}\rangle = O^{\lambda,\sigma,\tau}|\Psi_{\mathrm{g.s.}}\rangle \qquad (1.2)$$

where λ is the multipolarity of the resonance, σ its spin and τ its isospin. For example, the electric isoscalar transition operator has the form:

$$O^{\lambda,0,0} = \sum_{i=1}^{A} r^{\lambda} Y_{\lambda\mu}(\Omega_i)\,, \lambda \geq 2 \qquad (1.3)$$

where the sum is performed over all the nucleons and the $Y_{\lambda\mu}(\Omega_{\mathrm{i}})$ functions are the spherical harmonics in the coordinates of the nucleon *i*.

Using a schematic shell-model picture for the single-particle motion, we can understand the qualitative features of giant resonances. In this picture, the single-particle wave functions in subsequent shells $N, N+1, N+2, \ldots$ have alternating parity and an energy difference $\Delta E = \Delta N * 1\hbar\omega$. The $O^{\lambda,0,0}$ operator can only induce transitions with $\Delta N \leq \lambda$; parity considerations then imply that dipole ($\lambda = 1$) vibrations are composed by ΔN=1 excitations, while giant resonances with a quadrupole character ($\lambda = 2$), are composed by ΔN=2 excitations; the ΔN=0 excitations correspond to low-lying collective vibrations.

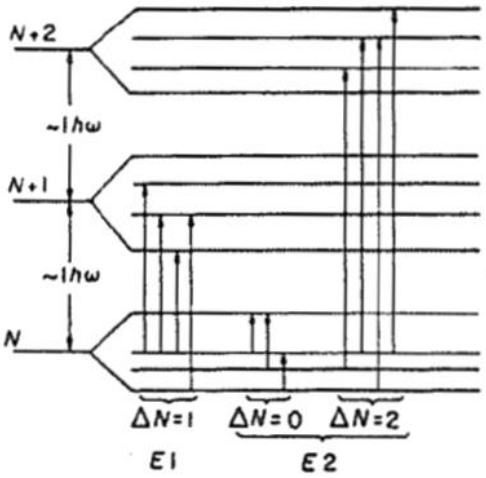

Fig. 1.2 - Schematic representation of E1 and E2 particle-hole states in a shell model picture; taken from [1].

More accurate microscopic descriptions of giant resonances are obtained with mean field models and effective nucleon-nucleon interactions. The most common approach is to describe the ground state of the nucleus with the Hartree-Fock method, generating a self-consistent mean field from the effective two-body interaction. The ground state is then a Slater determinant of single-particle orbitals where all the states below the Fermi surface are fully occupied and all the states above are empty. One can then study the effect of a small-amplitude density

fluctuation around the equilibrium configuration, induced by an external field. The fluctuations can be described with the time-dependent Hartree-Fock equation, and in the small-amplitude limit one can derive the Random-Phase Approximation (RPA) equations, which allow to diagonalize the residual interaction in the complete space of 1p-1h (1 particle - 1 hole) configurations. Second order RPA calculations include 2p-2h to account for the coupling of the resonance to more complex configurations. Other extensions of the RPA can be made to include the coupling to the continuum states (CRPA) or the effects of pairing correlations (QRPA, quasiparticle RPA).

Mean field approaches have been very successful in describing the properties of nuclei near the β-stability valley; the improvement in experimental techniques, however, makes it possible to study nuclei farther from stability, for which Relativistic Mean Field (RMF) approaches have been shown to be able to better reproduce the experimental data, in particular regarding the spin-orbit term (which is a parameter in non-relativistic approaches and is naturally derived from the Lagrangian in RMF approaches). It is also possible to build a self-consistent Relativistic RPA (RRPA) on top of a RMF description of the ground state, in order to study collective vibrations in a relativistic framework. RRPA can be extended to include the coupling to continuum states (CRRPA), which is very important with weakly bound exotic nuclei, and to include the pairing effect (QRRPA).

1.2. TRANSITION STRENGTHS

The reduced transition strength for the gamma decay between an excited state $|\mathrm{J_i}\rangle$ and a lower energy state $|\mathrm{J_f}\rangle$ is defined as:

$$B(\pi\lambda)\downarrow = \sum_{\mu,m_f} \left|\langle \mathrm{J_f} m_f | \hat{M}(\pi\lambda\mu) | \mathrm{J_i} m_i \rangle\right|^2 = \frac{1}{2J_i+1} \left|\langle \mathrm{J_f} \| \hat{M}(\pi\lambda) \| \mathrm{J_i} \rangle\right|^2 \quad (1.4)$$

where $\hat{M}(\pi\lambda\mu)$is the electromagnetic transition operator of parity π, (for electric transitions, $\pi_i\pi_f = (-)^{\lambda}$, for magnetic transitions $\pi_i\pi_f = (-)^{\lambda+1}$), multipolarity λ and magnetic component $\mu = m_i - m_f$.

The matrix element of $\hat{M}(\pi\lambda)$ is calculated between the initial and final states of the nuclear wave function. The reduced transition strength thus depends on the

structure of the nucleus, and is a quantity that can be calculated theoretically for comparison with the experimental data, in particular when $|J_f\rangle$ is the ground state.

The reduced transition strength is closely related to the width of the transition (and to the lifetime $\tau = \hbar/\Gamma$) by the following equation:

$$\Gamma = 8\pi \sum_{\pi,\lambda} \frac{\lambda+1}{\lambda((2\lambda+1)!!)^2} \left(\frac{E_\gamma}{\hbar c}\right)^{2\lambda+1} B(\pi\lambda)\downarrow \qquad (1.5)$$

The transition strength of an electromagnetic excitation is related to that of the gamma decay by:

$$B(\pi\lambda)\uparrow = \frac{2J_i+1}{2J_f+1} B(\pi\lambda)\downarrow \qquad (1.6)$$

The maximum possible value of the strength of a transition can be derived from sum rule arguments; giant resonances have strength close to that limit.

1.3. SUM RULES

Sum rules are a general feature of quantum systems, from atomic physics to particle physics, as they can be derived only from algebraic relations between the transition operators and powers of the Hamiltonian. The power of sum rule identities is that they encode a large amount of information about the energy spectrum and energy eigenfunctions of the system in a compact form, often in a way that is easily compared to experimental data. From a conceptual point of view the sum rule method provides a natural link between the quantum description of the collective phenomenon given by microscopic calculations and its macroscopic structure contained in classical models, emphasizing the crucial role played by bulk and/or surface parameters of the nuclear medium (incompressibility, symmetry energy, etc.). Many reviews of sum rules are available in literature, see for example [6]; we will give here only a brief summary, starting from the nuclear strength function

$$S_F(E) = \sum_{n\neq 0} \left|\langle 0|\hat{F}|n\rangle\right|^2 \delta(E - E_{n0}) \qquad (1.7)$$

where n labels the complete set of eigenstates of the Hamiltonian $\hat{H}$, $|0\rangle$ being the ground state, and E_{n0} are the energies of such states relative to the ground state

($E_{n0} = E_n - E_0$); $\hat{F}$ is the transition operator. One can define the moment of order k of the strength function as

$$M_k = \int_0^\infty S_F(E) E^k dE = \langle 0 | \hat{F}^\dagger (\hat{H}^k - E_0) \hat{F} | 0 \rangle \qquad (1.8)$$

In principle, the infinite set of moments ($-\infty < k < \infty$) determines the exact strength function; in the case of resonance phenomena, however, one only needs a few moments to obtain ad adequate description of $S_F(E)$.

Of particular importance is the first moment, also called the Energy-Weighted Sum Rule (EWSR) of the operator $\hat{F}$, as it is easy to see that expression 1.8 reduces to the sum over all the eigenstates of $\hat{H}$ of their energy weighted by their matrix element:

$$M_1 = \sum_n |\langle 0 | \hat{F} | n \rangle|^2 (E_n - E_0) = \frac{1}{2} \left\langle 0 \middle| \left[\hat{F}, [\hat{H}, \hat{F}] \right] \middle| 0 \right\rangle \qquad (1.9)$$

In the case of atomic nuclei, in general one can assume that $\hat{F} = \sum_k F(\vec{r}_k)$ is a one-particle operator depending only on the spatial coordinates (which is true for electric transitions, $\hat{F} = \hat{M}(E\lambda\mu)$), and if the Hamiltonian is velocity-independent (which is true for most effective interactions), one obtains from commutation rules that:

$$\sum_n |\langle 0 | \hat{F} | n \rangle|^2 (E_n - E_0) = \frac{\hbar^2}{2m} \int |\vec{\nabla} \hat{F}|^2 \varrho(\vec{r}) d\vec{r} \qquad (1.10)$$

where $\varrho(\vec{r})$ is the nucleon density in the ground state of the nucleus. This result can be understood intuitively when considering that an impulsive field $\hat{F}$ transfers a momentum $\vec{\nabla} \hat{F}$ to the particles which were on average at rest, meaning that they gain an average energy of $\hbar^2 |\vec{\nabla} \hat{F}|^2 / 2m$. This is consistent with the fact that the EWSR does not depend on the interaction among the nucleons, because the energy is absorbed before the system is disturbed from equilibrium.

1.4. TRANSITION DENSITIES

Giant resonances are described as vibrational states, meaning that an oscillation of the nucleon density around the ground state density $\rho^0(\vec{r})$ is expected. If we

consider an excited vibrational state $|\nu\rangle$, the corresponding time-dependent wave-function is

$$|\Psi(t)\rangle = |0\rangle + c_\nu|\nu\rangle e^{-iE_\nu t/\hbar} \qquad (1.11)$$

and the corresponding nucleon density is given by

$$\rho(\vec{r},t) = \langle\Psi(t)|\sum_{i=1}^{A}\delta(\vec{r}-\vec{r}_i)\,|\Psi(t)\rangle = \rho^0(\vec{r}) + \delta\rho(\vec{r},t) \qquad (1.12)$$

with

$$\delta\rho(\vec{r},t) = \langle 0|\sum_{i=1}^{A}\delta(\vec{r}-\vec{r}_i)\,|\nu\rangle\, e^{-iE_\nu t/\hbar} + c.c. \qquad (1.13)$$

The transition density is the time-independent part of $\delta\rho(\vec{r},t)$, that is

$$\rho^\nu(\vec{r}) = \langle 0|\sum_{i=1}^{A}\delta(\vec{r}-\vec{r}_i)\,|\nu\rangle \qquad (1.14)$$

Transition densities can be used to have an insight in the structure of a vibrational state, in particular regarding the spatial distribution of the oscillations, and can be easily calculated theoretically.

From an experimental point of view, it is difficult to probe the transition density directly. One can consider, however, that photon wavelengths of energies up to ~20 MeV are larger than the typical values of nuclear radii, meaning that a photon excitation involves the whole volume of the nucleus. In the case of peripheral collisions with hadronic probes, instead, the excitation is mainly superficial, because of the short range of the strong interaction, and states with transition densities peaked on the surface are favoured.

1.5. DECAY MECHANISM OF GIANT RESONANCES

As mentioned in §1.1.2, giant resonances can be described as a well-ordered, collective motion of all the nucleons, that is a coherent sum of many 1 particle-1 hole (1p-1h) excitations. The decay of a giant resonance is explained by more concurring mechanisms, each causing a part of the total width of the resonance. The contributions to the total width Γ are:

- $\Gamma^{\downarrow}$: damping width, caused by the coupling of the 1p-1h state of the giant resonance to more complex configurations; it is the dominant contribution to the total width
- $\Gamma^{\uparrow}$: escape width, which accounts for the direct emission of particles, since the 1p-1h state lies above the particle emission threshold; typically $\Gamma^{\uparrow}/\Gamma \sim 10^{-1}$
- Γ^{γ}: photon emission width, which is a much smaller contribution than the escape width because particle emission is favoured; $\Gamma^{\gamma}/\Gamma \sim 10^{-4}$

The damping of giant resonances is a prime example of how a well-ordered collective excitation dissolves into a disordered motion of internal degrees of freedom in fermionic quantum many-body systems.

At the high excitation energy of the giant resonance, in fact, there is a high density of 2p-2h configurations with the same spin and parity as the resonance. The 1p-1h state can mix with 2p-2h states, which in turn mix to 3p-3h, states, in a process that goes up in a hierarchy of complexity that ends in a state in which the excitation energy has been spread over all degrees of freedom and a compound nucleus is eventually formed.

This scheme implies a hierarchy of time scales, corresponding to the lifetimes characteristic for each coupling step, and corresponding energy scales ranging from the total width of the resonance, of the order of some MeV, to the width of compound nuclear states of the order of some eV. The search for experimental evidence of this picture is a long-standing problem.

1.5.1. FINE STRUCTURE OF GIANT RESONANCES

The presence of a fine structure superimposed on the broad bump of the Isoscalar Giant Quadrupole Resonance (ISGQR) in ^{208}Pb has been known for decades, first from high-resolution inelastic electron scattering [7], then from proton scattering [8]. This is shown for example in Fig. 1.3 for recent *(e,e')* and *(p,p')* experiments: all spectra show remarkable fluctuations of the resonance strength; the almost peak-to-peak correspondence of the fluctuations with different probes and experimental setups confirms that they are of physical, rather than statistical, nature.

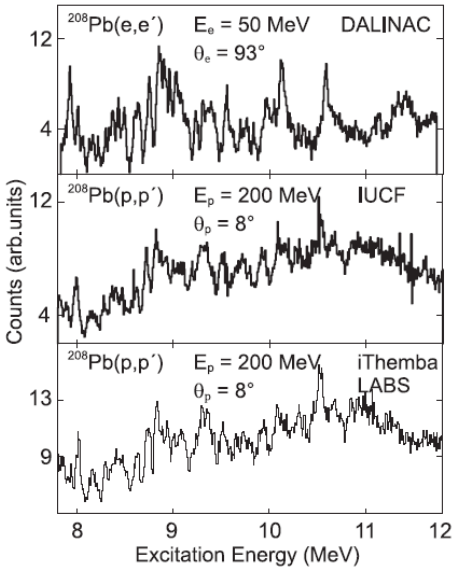

Fig. 1.3 - Excitation spectra of the ISGQR in ^{208}Pb, measured with high-resolution electron and proton scattering; the spectra show a fragmentation of the strength in a fine structure, with an almost peak-to-peak correspondence between the different measurements. Taken from [9].

Over the years, high-resolution *(p,p')* and *(e,e')* experiments have shown this fine structure to be a global feature of the ISGQR over a wide range of nuclei, such as ^{166}Er, ^{120}Sn, ^{90}Zr, ^{89}Y, ^{58}Ni [9], [10]; the excitation spectra for some of these nuclei are shown in Fig. 1.4, and all show the strong fluctuations associated to this phenomenon.

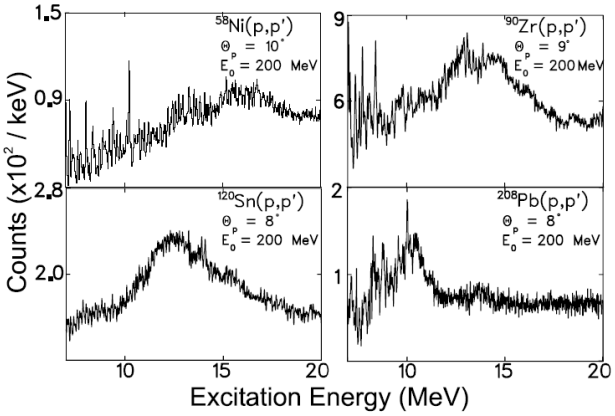

Fig. 1.4 - Excitation spectra of the ISGQR in various nuclei, studied with high-resolution proton scattering; all spectra show strong fluctuations superimposed on the resonance peak, associated to its fine structure. Taken from [15].

Fine structures have also been observed in other types of resonances such as the Isovector Giant Dipole Resonance (IVGDR) [11], [12], the magnetic quadrupole resonance [13], and the spin-isospinflip Gamow-Teller mode [11], [14], and are now established as a general property of giant resonances.

Different techniques have been used to extract the energy scales associated to the fine structure, such as local scaling dimension [16], [17], the entropy index method [18], [19], and continuous and discrete wavelet transforms [9], [15], [20]. Comparison with second-RPA calculations indicates that the energy scales can indeed arise from the first step of the damping mechanism, that is the coupling of the 1p-1h states to the 2p-2h states. A review of this kind of studies can be found in [9] and [10].

1.6. THE PYGMY DIPOLE RESONANCE

It is well known that nearly all of the electric dipole (E1) isovector EWSR is concentrated in the Isovector Giant Dipole Resonance (IVGDR), located in the energy range between 10 and 20 MeV. However, in the low energy tail of the GDR, close to the neutron separation energy (S_n), an excess of E1 strength is found, taking up to 1% of the EWSR in stable nuclei; this excess is commonly called Pygmy Dipole Resonance (PDR). The strength of the PDR is fragmented in a number of individual 1^- states spanning across an energy region of some MeV, with a typical separation of ~10-20 keV, and their combined contribution makes up the bulk behaviour of a resonance.

In the recent years, the study of the PDR has attracted a great deal of interest in the nuclear structure community, as there are still many open questions regarding its nature in stable and unstable neutron-rich nuclei. In fact, many different models have been used to describe the resonance, and while they all reproduce qualitatively and, at least in part, quantitatively the data, the predicted structure of the wave functions and thus the interpretation of the mode are different. Moreover, some question the actual collectivity of the resonance: while it is described microscopically as a sum of a large number of particle-hole excitations, the coherence of these excitation is in doubt.

In particular, strong pygmy structures (up to ~10% of the EWSR) have been observed in exotic nuclei [21-23], and it is not obvious that they are generated by the same mechanism as the PDR found in nuclei close to the valley of stability. This is important because it has been shown that the PDR strength can be related to the neutron skin thickness and can be used as a probe of the density dependence of the nuclear symmetry energy [24-26]. The study of the PDR is also important for explosive nucleosynthesis models, as the increase of E1 strength at low energies in neutron-rich nuclei could affect drastically the thermal equilibrium of *(γ,n)* and *(n, γ)* reactions along the r-process path [27-29].

1.6.1. EXPERIMENTAL INVESTIGATION

The most widely used technique to study the PDR in stable nuclei is the Nuclear Resonance Fluorescence (NRF) or real photon scattering. The target is probed by a beam of bremsstrahlung photons up to energies of ~10 MeV, and the scattered gamma-rays are detected with HPGe detectors. The NFR technique is very selective for E1 excitations, and is able to extract in a model-independent way the excitation energies and the lifetime of the states, and therefore the B(E1) values. The *(γ,γ')* technique was successfully used to collect systematic measurements of the PDR along the whole chart of nuclides, in particular around the Z = 20 [30], N = 50 [31], N = 82 [32], [33] and Z = 82, N = 128 [34], [35] shell closures.

The PDR excitation has also been measured with intermediate-energy inelastic scattering of protons at high resolution at 0°. The technique has been used so far only on ^{208}Pb, and has confirmed the NRF measurement of the B(E1) transition strength of known 1^- levels; it has the advantage of measuring equally well the E1 response above and below the particle threshold. This is important because the *(γ,γ')* technique is limited only to states below S_n and *(γ,n)* measurements are possible only above S_n, and both techniques suffer from large uncertainties near the S_n threshold.

Another method used to study the PDR is the inelastic scattering of alpha particles and the coincidence measurement of scattered alphas and de-excitation gamma-rays. The *(α,α'γ)* technique was used to study the PDR in ^{140}Ce [36], [37] and ^{138}Ba [38], as well as ^{124}Sn [39]. All these measurements show the same behaviour: up to a certain energy, all the states observed with *(γ,γ')* are confirmed, but for higher

energies the states observed with *(γ,γ')* could not be populated by the alpha scattering.

The results point to a splitting of the PDR in two structures: a low-energy one populated equally well by photons and alpha particles, and a high-energy one populated much better by photons. It is thought that this splitting reflects a different underlying structure: the low-energy states are of isoscalar nature and their transition density is peaked on the surface, while the high-energy states are of isovector nature and are associated to a transition towards the IVGDR. This picture is supported by relativistic quasiparticle random phase approximation calculations based on the relativistic Hatree-Bogoliubov model [40] and by relativistic quasiparticle time-blocking approximation calculations [39].

It can be shown that the PDR states can be excited also by the inelastic scattering of heavier ions; by tuning the beam energy, one can also change the relative population of the PDR with respect to the GDR, which is useful to disentangle the actual PDR contribution to the dipole strength from the tail of the GDR [41]. The experiment described in this thesis is the first to successfully study the PDR by means of inelastic scattering of heavy ions, establishing the feasibility and the validity of the technique.

1.6.2. THEORETICAL MODELS

The PDR can be described in the most simple way as an out of phase vibration of a N=Z core against a skin formed by the excess neutrons. This picture can be used for simple hydrodynamical models which involve classical oscillations of the nucleon fluids, such as the three-fluid (protons, neutrons in the same orbitals as protons and excess neutrons) model [42] based on the Steinwedel-Jensen model [43], [44], and the two-fluid (core and skin nucleons) model [45]. These models however predict a too low value of the strength of the resonance.

A microscopic description of the PDR can be obtained with density functional theory approaches [46] or with the HF+RPA approach using various effective interactions [47-49], as well as quasiparticle-RPA (QRPA) and quasiparticle phonon model (QPM) [50], [51] and CRPA approaches. Relativistic descriptions have also been developed, which are important in particular when going towards very n-rich nuclei;

see [52] for a review paper on RRPA [32], RQRPA [53], as well as continuum QRRPA [54] techniques; another successful approach is the relativistic quasiparticle time blocking approximation (RQTBA) [55]. All these approaches predict the presence of low-lying states with similar strengths and transition densities, but there is still an open discussion on whether this strength corresponds to a collective mode [52], in particular regarding the coherence of the particle-hole states that contribute to the resonance [56].

In general, all microscopic descriptions of the PDR states agree on the fact that it is mainly caused by a neutron vibration peaked on the surface: this can be seen clearly with transition density calculations, such as the one shown in Fig. 1.5, taken from [34]. The continuous line represent the neutron transition density, while the dashed line represents the proton transition density. While in the case of the IVGDR a clear opposition of the neutron and proton densities is visible, for the PDR protons and neutrons move in phase in the nucleus interior, representing a predominantly isoscalar nature of the excitation, while at the surface only neutrons contribute.

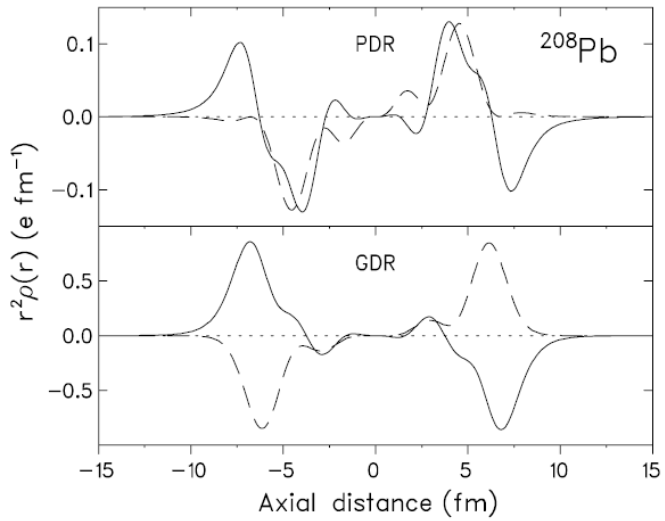

Fig. 1.5 - Transition densities calculated for the ^{208}Pb PDR (top panel), with energy between 7 MeV and 8 MeV, and GDR (bottom panel), with energy above 8 MeV, within the QPM; taken from [34].

Chapter 2. Inelastic scattering of heavy ions

In the experiment described in this thesis, an ^{17}O beam at the energy of 20 MeV/u in the laboratory frame was used to populate highly excited states in the target nuclei, including the pygmy resonance and giant quadrupole resonance states, through inelastic scattering, and the gamma decay from such states was measured. In §2.1 a small overview of a previous measurement employing the same technique will be given. §2.2 will describe the Distorted Wave Born Approximation (DWBA), which can be used to give a simple but effective theoretical description of the inelastic scattering of heavy ions. In §2.3 more details on the effective interaction between projectile and target nuclei used for the DWBA calculations performed with the PTOLEMY code [57-59] will be given. Finally, in §2.4 the results of such calculations for the estimate of the excitation cross section of the ISGQR state in ^{208}Pb and ^{90}Zr will be shown.

2.1. INELASTIC SCATTERING OF HEAVY IONS AS A TOOL FOR THE STUDY OF GIANT RESONANCES

Giant resonances have been studied over the years with many different probes, going from electrons and protons up to heavy ions. The main advantage of heavy ions compared to other probes is that they can provide much larger cross-sections and a better peak-to-continuum ratio due to a decrease of knock-out reactions compared to protons [60].

One problem encountered when using heavy-ion scattering to study giant resonances is that the angular distributions of the cross sections for the excitation of nuclear states are not very sensitive to the angular momentum transfer. For this reason it is useful to detect the de-excitation gamma-rays together with the scattered ions, since photon selection rules are very sensitive to angular momentum.

Another problem encountered when using heavy ions to populate high-energy states in the target nuclei is that projectile excitation can become a major source of background, forming broad structures superimposed on those caused by target

excitation [60], [61]. For this reason, it is useful to use a projectile with a small neutron separation energy (S_n), such as ^{13}C (S_n=4.9 MeV) or ^{17}O (S_n=4.1 MeV): in this way, if an excitation energy above S_n is transferred to the projectile, the neutron emission channel becomes dominant and the event is removed from the inelastic scattering channel.

Fig. 2.1 shows the difference between the excitation spectra of a ^{208}Pb target, bombarded with an ^{17}O (left panel) or a ^{16}O (right panel) beam; the energy region highlighted in blue is dominated by projectile excitation in the case of ^{16}O and is very clean in the case of ^{17}O.

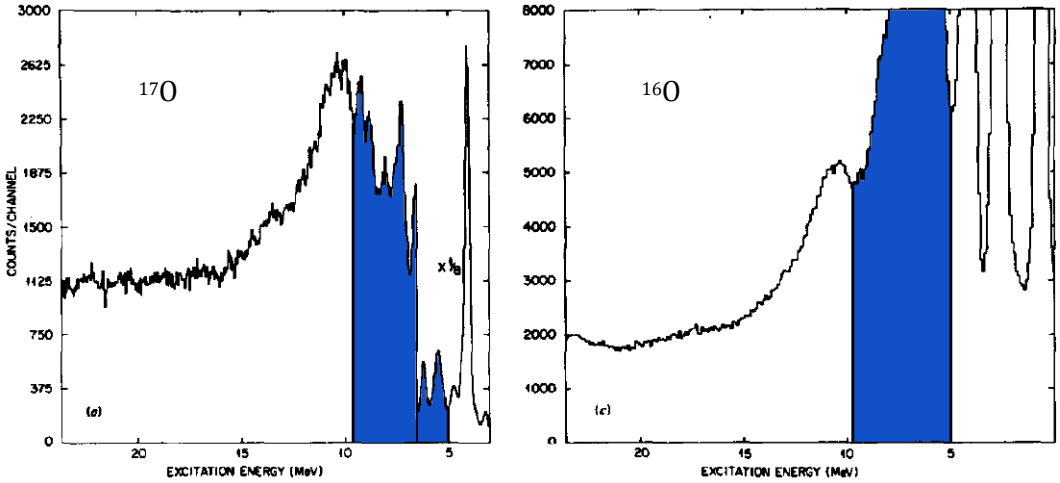

Fig. 2.1 - Inelastic scattering spectra for a ^{208}Pb target bombarded with an ^{17}O (left panel) and a ^{16}O (right panel) beam; the broad structure in the highlighted area of the ^{16}O spectrum is caused by projectile excitation and is completely removed with the ^{17}O beam. Adapted from [60].

The inelastic scattering of an ^{17}O ion at the energy of 22 MeV/u was used to study the gamma decay of the ISGQR of ^{208}Pb, in an experiment that successfully measured the strength of the resonance and its coupling with low-lying collective states [62]. The same technique was used at higher beam energy, 84 MeV/u, to study the Coulomb excitation of the IVGDR as well as the ISGQR [63].

These measurements were performed at Oak Ridge National Laboratories in the '80s with the spin spectrometer [64]. Our experiment employs the same experimental technique but can take advantage of improved experimental

conditions. In particular, the gamma ray detection is performed with the AGATA Demonstrator [65], [66], that is the first step of the new generation segmented HPGe gamma-ray spectrometer AGATA, and by an array of $LaBr_3$:Ce and BaF_2 scintillator detectors. While the solid angle covered by our setup is smaller compared to the spin spectrometer, we can take advantage of a much better energy resolution for the measurement of gamma-ray energies. The detection of the scattered ^{17}O ions is performed with two segmented Si telescopes, covering a large solid angle which compensates for the lost efficiency in the gamma detection. See Chapter 3 for more details on the experimental setup.

2.2. The Distorted Wave Born Approximation

Inelastic scattering of heavy ions at intermediate energies (10-100 MeV/u) can be well described within the Distorted Wave Born Approximation (DWBA). We used DWBA calculations both for obtaining cross-section estimates in preparation of the experiment and for the analysis of the PDR excitation (see §6.7). The main features of the DWBA will now briefly be recalled, following [67]. See also [68] for a more detailed treatment.

The underlying assumption of all distorted wave theories is that elastic scattering and absorption are the most important events to occur when two nuclei collide. These two phenomena can be represented by the use of a complex optical potential; the elastic scattering is then described exactly (within the limitations of optical models) and the other reaction channels are treated as perturbations.

The collision between two nuclei can be seen as a wave process in which a plane wave (the projectile nucleus) hits an absorbing target nucleus creating a spherical scattered wave. Consider the following binary reaction

$$A + a \longrightarrow B + b \qquad (2.1)$$

where a is an incoming beam ion, A is a target nucleus, and the reaction products are a beam-like ejectile b and target-like recoil B.

The system before the scattering can be described by the following wave function in the centre of mass frame of reference

$$\psi_i = N e^{i\vec{k}_\alpha \vec{r}_\alpha} \psi_a \psi_A \qquad (2.2)$$

where ψ_a and ψ_A are the wave functions describing the internal degree of freedom of the two nuclei, while $\vec{r}_\alpha$ and $\vec{k}_\alpha$ are respectively

$$\vec{r}_\alpha = \vec{r}_a - \vec{r}_A \qquad (2.3)$$

$$\vec{k}_\alpha = \frac{m_a\vec{k}_a - m_A\vec{k}_A}{m_a + m_A} \qquad (2.4)$$

It will also be convenient to introduce the reduced mass

$$\mu_\alpha = \frac{m_a m_A}{m_a + m_A} \qquad (2.5)$$

After the collision the total wave function will have a scattered component for each possible reaction channel, that is

$$\psi_{tot} = Ne^{i\vec{k}_\alpha\vec{r}_\alpha}\psi_a\psi_A + \sum_\beta \psi_{scatt,\beta} \qquad (2.6)$$

The scattered wave function is spherical, and has the form

$$\psi_{scatt,\beta} = Nf_\beta(\vartheta,\varphi)\,\frac{e^{i\vec{k}_\beta\vec{r}_\beta}}{r_\beta}\psi_b\psi_B \qquad (2.7)$$

where the factor $f_\beta(\vartheta,\varphi)$ is called scattering amplitude and modulates the amplitude of the wave function as a function of the scattering angle and the bombarding energy, and ψ_b and ψ_B are the wave functions describing the internal state of the reaction products.

Each nucleus moves away from the target with a relative velocity v_β, meaning that the total number of particles emitted in a solid angle $d\Omega$ is $v_\beta\left|Nf_\beta(\vartheta,\varphi)\right|^2$; dividing by the incident flux $v_\alpha|N|^2$ one obtains the differential cross-section for the reaction channel β:

$$\frac{d\sigma_\beta}{d\Omega} = \frac{v_\beta}{v_\alpha}\left|f_\beta(\vartheta,\varphi)\right|^2 \qquad (2.8)$$

In order to give an expression for the scattering amplitude, one must solve the time-dependent Schrödinger equation with a solution of the form of Eq. 2.6 and Eq. 2.7.

For a single particle of mass m, with no internal degrees of freedom, which scatters from a fixed potential $U(\vec{r})$, the Schrödinger equation is

$$\left(-\frac{\hbar^2}{2m}\nabla^2 + U(\vec{r})\right)\chi(\vec{r}) = E\chi(\vec{r}) \qquad (2.9)$$

In a realistic case, though, both target and projectile nuclei actually have internal degrees of freedom, and $U(\vec{r})$ can excite one or both. The internal wave functions ψ_a and ψ_A are solutions to:

$$H_a\psi_a = \epsilon_a\psi_a \; H_A\psi_A = \epsilon_A\psi_A \qquad (2.10)$$

where H_a and H_A contain a kinetic term and an interaction term. The final Schrödinger equation to be solved is therefore:

$$\left(H_a + H_A - \frac{\hbar^2}{2\mu_\alpha}\nabla_\alpha^2 + U_\alpha(\vec{r}_\alpha)\right)\psi_{tot} = E\psi_{tot} \qquad (2.11)$$

where E is the total energy of the system, and ψ_{tot} has the form described in Eq. 2.6 and Eq. 2.7. The general solution of Eq. 2.11 has the form

$$\psi_{tot} = \sum_{b,B} \chi_{b,B}(\vec{r}_\alpha)\psi_b\psi_B \qquad (2.12)$$

We now focus only on the relative motion of the nuclei and ignore the internal degrees of freedom, in order to find an integral solution to Eq. 2.9 and determine the scattering amplitude. A more detailed description should also include the internal degrees of freedom and therefore solve Eq. 2.11.

The general solution to Eq. 2.9 is given by the incident plane wave plus the scattered wave and it can be written as

$$\chi(\vec{k},\vec{r}) = e^{i\vec{k}\vec{r}} - \frac{1}{4\pi}\int \frac{e^{ik|\vec{r}-\vec{r}'|}}{|\vec{r}-\vec{r}'|}U(\vec{r}')\chi(\vec{k},\vec{r}')d\vec{r}' \qquad (2.13)$$

which, evaluated at large $|\vec{r}|$ becomes

$$\chi(\vec{k},\vec{r}) = e^{i\vec{k}\vec{r}} - \frac{e^{i\vec{k}\vec{r}}}{4\pi r}\int e^{i\vec{k}\vec{r}'}U(\vec{r}')\chi(\vec{k},\vec{r}')d\vec{r}' \qquad (2.14)$$

From this, one obtains a scattering amplitude

$$f_\beta(\vartheta,\varphi) = -\frac{1}{4\pi}\int e^{i\vec{k}\vec{r}'}U(\vec{r}')\chi(\vec{k},\vec{r}')d\vec{r}' \qquad (2.15)$$

Of course, this is only a formal solution since it contains the unknown wave function $\chi(\vec{k},\vec{r}')$. Some approximations are necessary in order to solve the equation. In the DWBA approach, it is assumed that the potential U can be written as $U = U_1 + U_2$ and that the exact solution $\chi_1(\vec{k},\vec{r})$ of Eq. 2.9 for U_1 is known. Typically, U_1 is the

optical potential which causes the elastic scattering, while U_2 is the potential that induces non-elastic transitions, and can be treated as a perturbation.

One can distinguish two types of solution, one given by a plane wave and a scattered wave in the exit channel, $\chi_1^{(+)}(\vec{k},\vec{r})$, and one with a scattered wave in the entrance channel, $\chi_1^{(-)}(\vec{k},\vec{r})$; the two solutions are one the time inverse of the other:

$$\chi_1^{(-)}(\vec{k},\vec{r}) = \chi_1^{(+)}(-\vec{k},\vec{r})^* \qquad (2.16)$$

The two waves are called distorted waves.

The full scattering amplitude is the sum of a contribution given by U_1 and a term concerning U_2:

$$f(\vartheta,\varphi) = f_1(\vartheta,\varphi) - \frac{1}{4\pi}\int \chi_1^{(-)}(\vec{k},\vec{r}')^* U_2(\vec{r}')\chi(\vec{k},\vec{r}')d\vec{r}' \qquad (2.17)$$

If U_2 is treated as a perturbation of U_1, one can approximate the unknown $\chi(\vec{k},\vec{r}')$ with $\chi_1^{(+)}(\vec{k},\vec{r})$ in Eq. 2.17; the resulting amplitude is

$$f_{DWBA}(\vartheta,\varphi) = f_1(\vartheta,\varphi) - \frac{1}{4\pi}\int \chi_1^{(-)}(\vec{k},\vec{r}')^* U(\vec{r}')\chi_1^{(+)}(\vec{k},\vec{r}')d\vec{r}' \qquad (2.18)$$

The generalized expression for the DWBA transition amplitude for the reaction A(a,b)B, that is the solution of Eq. 2.11, is given by

$$f_{DWBA}(\vartheta,\varphi) = -\frac{1}{4\pi}\iint \chi_\beta^{(-)}(\vec{k}_\beta,\vec{r}_\beta)^* \langle b,B|U_2|a,A\rangle \chi_\alpha^{(+)}(\vec{k}_\alpha,\vec{r}_\alpha)d\vec{r}_\alpha d\vec{r}_\beta \qquad (2.19)$$

where χ_α and χ_β are the generalization of χ_1 describing the elastic scattering in the entrance and exit channel respectively, while the matrix element $\langle b,B|U_2|a,A\rangle$ takes into account the non-elastic channels and the internal structure of the nuclei.

2.3. Effective interaction between heavy ions

The nuclear potentials discussed in the previous section represent the interaction between two nuclei when they collide. Such potentials are made by the sum of the long range Coulomb potential, due to the presence of protons, and a short range potential due to the nuclear force.

The nuclear potential depends on the nucleon-nucleon interaction which can be parameterized by several models. In a heavy ions reaction the nuclear potential is

given by the integral over all the interactions between nucleons present both in the projectile nucleus and in the target nucleus. It can be written as:

$$U(\vec{r}) = \iint \rho_p(\vec{r}_p)\rho_t(\vec{r}_t)\, v(\vec{r}_{tp}) d\vec{r}_p d\vec{r}_t \qquad (2.20)$$

where $\rho_p(\vec{r}_p)$ and $\rho_t(\vec{r}_t)$ represent the projectile nucleon density in the point $\vec{r}_p$ and the target nucleon density in the point $\vec{r}_t$, and $v(\vec{r}_{tp})$ is the nucleon-nucleon interaction, with $\vec{r}_{tp} = \vec{r}_t - \vec{r}_p$, as shown in Fig. 2.2.

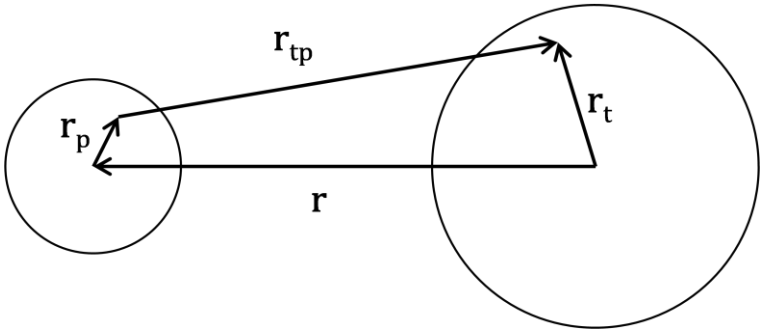

Fig. 2.2 - Coordinates of the integral of Eq. 2.20

Typically, $U(\vec{r})$ has a Woods-Saxon form whose depth (around -50 MeV for a single nucleon potential) depends on the number of nucleons and on the model used to describe the nucleon-nucleon interaction. The potential has a real part, that describes the elastic scattering process, as well as an imaginary part:

$$U(r) = V(r) + iV_I(r) \qquad (2.21)$$

where $V(r)$ is a Woods-Saxon potential with depth V, radius $R = r_0 A^{1/3}$ and diffusiveness a, and $V_I(r)$ is the imaginary component of the potential, with depth V_I (typically a fraction of V), radius $R_I = r_{I0} A^{1/3}$ and diffusiveness a_I:

$$V(r) = \frac{V}{1 + e^{\frac{r-R}{a}}} \quad V_I(r) = \frac{V_I}{1 + e^{\frac{r-R_I}{a_I}}} \qquad (2.22)$$

The imaginary part of the potential accounts for the absorption of the incident wave caused by non-elastic processes: in a heavy ion reaction there are many open channels, and if an internal excitation or a particle transfer occurs, the system does not return to the entrance channel and the projectile is absorbed.

This optical potential accounts for the dominant part of the interaction between the two nuclei, and corresponds to the U_1 term in the discussion above. In order to

calculate the reaction cross section for an inelastic scattering process, however, it is also necessary to describe the residual interaction that corresponds to the U_2 term in the discussion above.

All DWBA calculations for our experiment were carried out with the PTOLEMY code [57-59], which was developed specifically to treat heavy-ion inelastic scattering and transfer reactions. PTOLEMY calculates the inelastic cross sections using an effective interaction of the form:

$$H_l(r) = H_{l,C}(r) + H_{l,N}(r) \qquad (2.23)$$

where l is multipolarity of the transition (which must be greater than 0), $H_{l,C}(r)$ is the Coulomb part of the interaction and $H_{l,N}(r)$ is the nuclear component; spin-orbit forces are neglected. The nuclear term is given by:

$$H_{l,N}(r) = -\frac{\beta_l}{\overline{\beta_l}}\left(R'\frac{dV(r)}{dr} + iR'_I\frac{dV_I(r)}{dr}\right) \qquad (2.24)$$

where $V(r)$ and $V_I(r)$ are the real and imaginary parts of the optical potential, and the radii R' and R'_I are the radii of the excited nucleus:

$$R' = r_0 A'^{1/3} \; R'_I = r_{I0} A'^{1/3} \qquad (2.25)$$

with $A' = A$ for target excitation and $A' = a$ for projectile excitation. $\overline{\beta_l} = (\beta_l + \beta_{l,C})/2$ is the average between the nuclear deformation parameter β_l and the Coulomb deformation parameter $\beta_{l,C}$, and serves as a normalization for the two components of the interaction.

The Coulomb part of the effective interaction is derived from the multipole expansion of the potential between a point charge and a uniformly charged sphere, and can written as:

$$H_{l,C}(r) = \frac{\beta_{l,C}}{\overline{\beta_l}} R'_C \frac{3Z_a Z_A e^2}{(2l+1)} \begin{cases} \dfrac{r^l}{R_C^{l+2}} & r < R_C \\ \dfrac{R_C^{l-1}}{r^{l+1}} & r > R_C \end{cases} \qquad (2.26)$$

where Z_a and Z_A are the atomic numbers of the two nuclei, R'_C is the Coulomb radius of the excited nucleus, $R'_C = r_{C0} A'^{1/3}$, while R_C is the Coulomb radius of the optical potential, $R_C = r_{C0}\left(a^{1/3} + A^{1/3}\right)$.

The Coulomb deformation parameter $\beta_{l,C}$ is also related to the reduced transition rate of the transition (see also §1.2):

$$B(El)\uparrow = \left|\frac{3Z}{4\pi}R_C^l\beta_{l,C}\right|^2 \frac{(2J_f+1)}{(2J_i+1)(2l+1)} \qquad (2.27)$$

where J_i and J_f are the angular momenta of the initial and final states. The relation can be inverted to obtain the deformation parameter of a state with known strength:

$$\beta_{l,C} = \frac{4\pi}{3Z}\sqrt{B(El)\uparrow}\, R_C^l \sqrt{\frac{(2J_i+1)(2l+1)}{(2J_f+1)}} \qquad (2.28)$$

In the case of the excitation of giant resonances, the strength of the resonance is commonly given as a fraction of the Energy Weighted Sum Rule (EWSR). It is then possible to calculate the corresponding deformation parameter by scaling appropriately the deformation length corresponding to the sum rule limit, which has the following expression for transitions with $l \geq 2$:

$$(\beta_l R)^2 = l(2l+1)\frac{2\pi\hbar^2}{3AmE} \qquad (2.29)$$

where m is the nucleon mass and E is the energy of the state. This means that if a state has a strength equivalent to a fraction f of the EWSR, the corresponding deformation parameter is given by

$$\beta_l = \sqrt{f * l(2l+1)\frac{2\pi\hbar^2}{3AmR^2E}} \qquad (2.30)$$

2.4. CROSS SECTION CALCULATIONS

As mentioned above, all the inelastic scattering cross section calculations for our experiment were performed in the DWBA approximation by the PTOLEMY code [57-59]. The inputs required by the code are:

- the entrance and exit channels of the reaction
- the beam energy
- the energy, spin and parity of the excited state
- the nuclear deformation parameter
- the Coulomb deformation parameter; the reduced transition strength can also be given instead

- the depth, radius and diffusiveness for both the real and the imaginary part of the optical potential
- the range of scattering angles (in the centre-of-mass frame of reference) for which to perform the calculations

If the $B(El)$ of the state is given as an input, PTOLEMY proceeds to calculate $\beta_{l,C}$ by using Eq. 2.28. If only one between β_l or $\beta_{l,C}$ is given as an input, the other is calculated by the code with the requirement that the two deformation lengths must be equal:

$$\beta_l r_0 = \beta_{l,C} r_{C0} \qquad (2.31)$$

Note that the output files of the PTOLEMY code give the differential cross sections in the centre-of-mass frame of reference, while we need them in the laboratory frame of reference to decide the positioning of the detectors; the transformation of the cross sections from one frame of reference to the other was performed with Eq. A.12; see Appendix A for more details.

Since the main aim of our experiment was to study the gamma decay from the ISGQR of ^{208}Pb and ^{90}Zr, the first calculations we performed were for the population of that state in both nuclei. We used the optical potential parameters taken from [61] and [62], and used Eq. 2.30 to calculate the deformation length from the strength reported in literature.

The differential cross sections for the population of the ISGQR state in ^{208}Pb and ^{90}Zr, at the beam energy used in the experiment (20 MeV/u), are shown in Fig. 2.3. Note how the ^{208}Pb cross section is peaked around 14°, while the ^{90}Zr cross section is stronger at smaller angles: this is mainly because of the different kinematics, ^{90}Zr being much lighter. For this reason, the Si telescopes used to detect the scattered beam ions have been placed at different angles for the two measurements (see also §3.2); the vertical lines mark the angular range covered by the detectors during our experiment.

In order to study the energy dependence of the cross section, we also performed the calculation at various beam energies, from 19 MeV/u to 21 MeV/u. The differential cross sections we obtained are shown in Fig. 2.4 for the ^{208}Pb and for the ^{90}Zr GQR

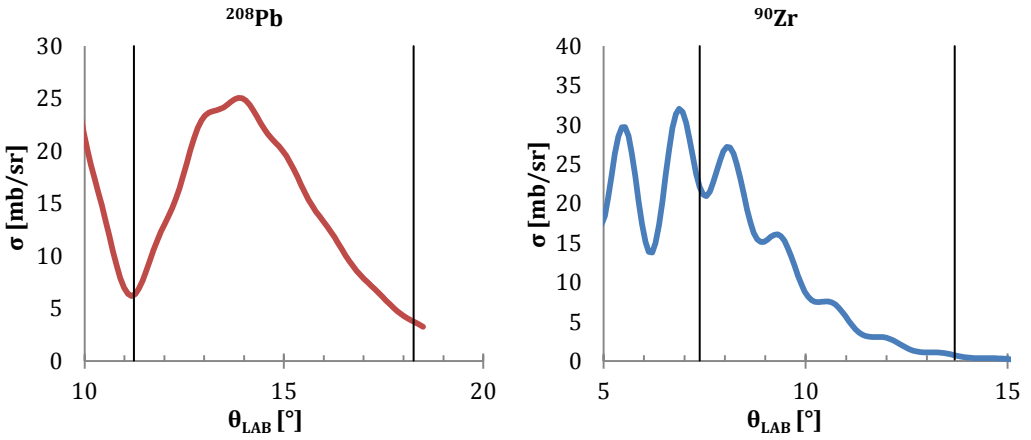

Fig. 2.3 - Cross section calculations performed with PTOLEMY for the population of the ISGQR state in ^{208}Pb (left panel) and ^{90}Zr (right panel) with an ^{17}O beam at the energy of 20 MeV/u.

excitation. For increasing beam energy, the cross section increases and becomes more focused towards smaller angles. The trade-off is that the cross-section of the elastic scattering channel increases very quickly at smaller angles: if we had performed the experiment at a higher energy, we would have had to move the detectors closer to the beam direction, and this would have caused a much higher counting rate in the detectors because of the elastic channel.

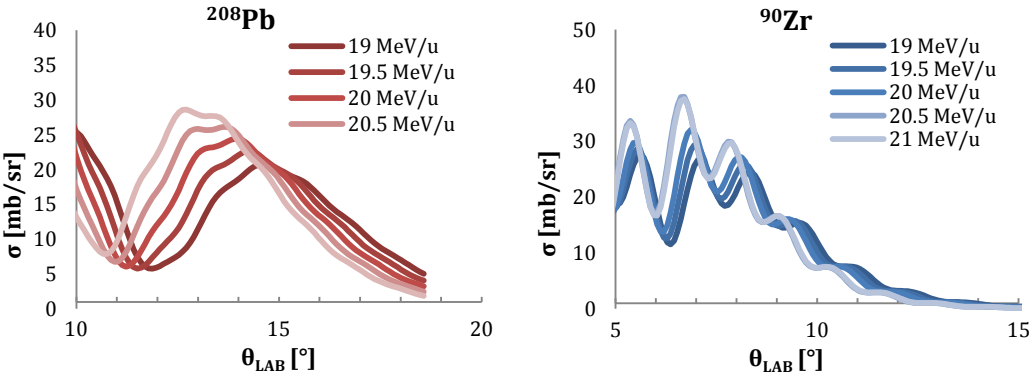

Fig. 2.4 - Cross section calculations performed with PTOLEMY for the population of the ISGQR state in ^{208}Pb (left panel) and ^{90}Zr (right panel) with an ^{17}O beam at energies from 19 MeV/u to 21 MeV/u.

Chapter 3. Experimental Setup

The experiment described in this thesis was performed at the Legnaro National Laboratories (LNL), in Italy, in summer 2010. The experimental setup was designed to measure gamma-rays of energies up to ~12-15 MeV in coincidence with scattered ^{17}O ions at an energy of 20 MeV/u.

The beam was produced with the PIAVE-ALPI accelerator system of the Legnaro National Laboratories [69]. PIAVE is a superconducting radio-frequency quadrupole, and was used as an injector for the superconducting linear accelerator ALPI. The average beam current was around 0.5 pnA and was limited by the counting rate on the AGATA detectors. The targets were a ^{208}Pb foil with a thickness of 2.6 mg/cm^2, and a ^{90}Zr foil with a thickness of 2 mg/cm^2; both targets were enriched to 99%.

The detection of the gamma-rays was performed with the AGATA (Advanced Gamma Tracking Array) Demonstrator, that is the first implementation of the AGATA spectrometer [65], [66], [70], the new generation gamma detector based on the techniques of pulse shape analysis and gamma-ray tracking. More details on the Demonstrator will be given in §3.1.

The aim of the experimental campaign of the AGATA Demonstrator at LNL is to validate the gamma tracking concept in actual physics experiments to demonstrate the capabilities of the instrument. In particular, several experiments of the campaign coupled the Demonstrator to the PRISMA magnetic spectrometer [71] to study the gamma decay from nuclei produced by multi-nucleon transfer and deep inelastic reactions, making use of the ion tracking capabilities of PRISMA to perform a better Doppler correction. PRISMA was not suitable for our experiment, however, since it is designed for reactions with heavier beams at lower energies. For this reason, we used segmented Si telescopes for the detection of the scattered ions; a description of these telescopes will be given in §3.2.

The AGATA Demonstrator was also coupled to the large volume $LaBr_3$:Ce scintillators from the HECTORplus array, which will be described in §0. The

remaining solid angle, limited by the presence of the PRISMA spectrometer on one side, was covered with the BaF_2 clusters of the HELENA array, which will be described in §3.4.

Two Data AcQuisition (DAQ) systems were running in parallel during the experiment: one for the AGATA Demonstrator, based on NARVAL [72], and one for the ancillary detectors, based on KMAX [73]. Both will be described in §3.5. Finally, the trigger condition for the experiment will be described in §3.6.

3.1. THE AGATA DEMONSTRATOR

AGATA is a project, within an European collaboration, aimed at developing, building and employing a 4π gamma-ray tracking array for nuclear spectroscopy. The principle of gamma-ray tracking is to reconstruct the sequence of interactions of each gamma-ray inside the array, in order to achieve a good suppression of the Compton background and a high efficiency, overcoming the limits of Compton-suppressed HPGe arrays.

The present phase of the AGATA project is the so called AGATA Demonstrator, an array composed by 15 HPGe detectors organized in 5 triple-clusters. The Demonstrator has been employed from the beginning of 2009 to the end of 2011 in an experimental campaign at Legnaro National Laboratories, in order to validate the feasibility of the whole tracking process in real experimental conditions.

At the time of our experiment, however, one of the triple-clusters was not yet installed at LNL because of delays with the production of the detectors, and another was not available because the cryostat was broken; therefore, we had to perform the measurement with 3 triple-clusters, for a total of 9 HPGe detectors.

The main components of the AGATA project will be now briefly described; more details can be found for example in [66] and [70].

3.1.1. CONCEPTUAL DESIGN OF AGATA

The geometrical structure of AGATA is designed with the aim of maximising solid angle coverage while minimizing development and maintenance cost; in particular, the solid angle had to be covered with few elementary shapes and the detectors had

to be grouped in clusters to increase modularity. As discussed in more detail in [74], GEANT4 simulations were used to decide the best performing configuration, that is based on the geodesic tiling of a sphere with 12 regular pentagons and 180 hexagons. Owing to the symmetries of this specific buckyball construction three slightly different irregular hexagons are needed (see Fig. 3.1); the three shapes are indicated by the colours red, green, and blue. The detectors are grouped in 60 identical triple-clusters, each containing a red, a green, and a blue crystal arranged in one cryostat (see Fig. 3.3); the pentagonal detectors are individually canned.

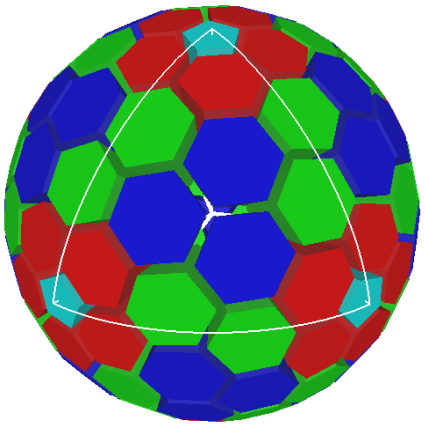

Fig. 3.1 - Schematic view of the full AGATA detector; the different colours represent the different shapes of the detectors.

The inner radius of the array is 23.5 cm. The total solid angle covered by HPGe material is close to 80% and the photo peak efficiency is as high as 50% for individual 1 MeV gamma rays.

The design performance of the AGATA array has been evaluated with GEANT4 simulations [74] considering the actual shape of the crystals and the dead materials from the encapsulation and the canning into triple clusters. In Tab. 3.1 the obtained photopeak efficiency and peak-to-total ratio are compared with the performance of an "ideal shell" of HPGe and of EUROBALL, which was a state-of-art Compton-suppressed HPGe array [75]. Even if a realistic detector can achieve only about 50% of the performance of the ideal shell, the efficiency gain with respect to EUROBALL is evident. In particular for high multiplicity experiments, one obtains an increase in selectivity of several orders of magnitude.

ARRAY	Number of crystals	Amount of HPGe [kg]	ε_{ph} [%] ($M_\gamma = 1$)	ε_{ph} [%] ($M_\gamma = 30$)	P/T [%] ($M_\gamma = 1$)	P/T [%] ($M_\gamma = 30$)
EUROBALL	239	210	9	6	56	37
AGATA	180	320	38	24	53	44
Ideal shell	1	233	65	36	58	60

Tab. 3.1 - Estimated performances of AGATA at E_γ= 1 MeV, compared to those of an ideal shell of HPGe and those of EUROBALL; ε_{ph} is the photopeak efficiency and P/T is the "peak to total ratio" . Taken from [70].

A key feature of AGATA is the capability to determine the emission direction of the detected gamma-rays with a precision of ~1°. This corresponds to an effective solid angle granularity of $5*10^4$ (unachievable with individual germanium crystals) and ensures an energy resolution better than 0.5% for transitions emitted by nuclei recoiling at velocities as high as 50% of the speed of light. This value is only a factor of two bigger than the intrinsic resolution of HPGe detectors and is comparable with the values currently observed at 10 times smaller recoil velocity.

3.1.2. *HIGH-FOLD SEGMENTED DETECTORS*

In order to match the requirements of tracking algorithms, the positions where the gamma rays interact inside the detector volume should be determined with an accuracy of ~5 mm at an energy of 1 MeV. While it is impossible to achieve such granularity by a physical segmentation of the crystal, pulse-shape analysis methods (PSA) can provide this position accuracy; they require in any case a medium level segmentation of the outer detector contact into 20 - 40 segments.

The AGATA array is composed of large volume 36-fold segmented n-type germanium detectors in the semi-coaxial geometry, such as the one depicted in Fig. 3.2. The detectors are produced by the French company Camberra and have a length of 90 mm, a diameter of 80 mm at the rear, and a tapering to a irregular hexagonal shape with an angle of 10° at the front. The sector-wise segmentation goes through the middle of each hexagonal side, the longitudinal segmentation forms rings of varying thickness, optimised for a uniform distribution of the gamma-ray interactions. Because of their complexity and the need of packing them very close to each other, these detectors use the encapsulation technology developed for the clusters of EUROBALL.

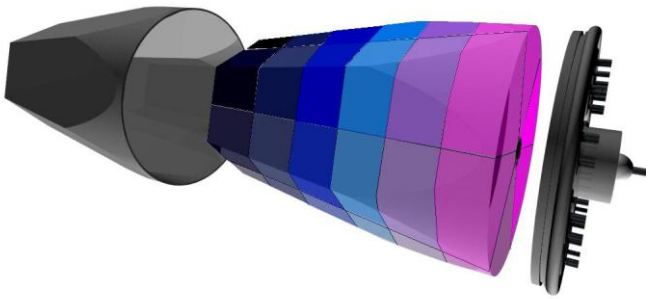

Fig. 3.2 - The 36-fold encapsulated segmented detector for the AGATA array, together with the its aluminium can.

For each crystal, there are 37 wires (36 segments + the central contact) passing very close to each other and to the crystal surface, so that shielding of the individual channels against cross-talk is of crucial importance; a ceramic material was used to isolate the core contact, which is used to apply the bias voltage and to obtain the core energy signal.

As mentioned in 3.1.1, the AGATA detectors are arranged in triple-clusters containing one of each type of hexagonal crystals. All three detectors are placed inside a single cryostat and are cooled to 90 K with a liquid nitrogen system. The preamplifiers for all segment and core signals are also cooled to 130 K; even though the power dissipated by each preamplifier is rather small, the sum of all 111 channels in a triple-cluster builds up to ~2.3 W.

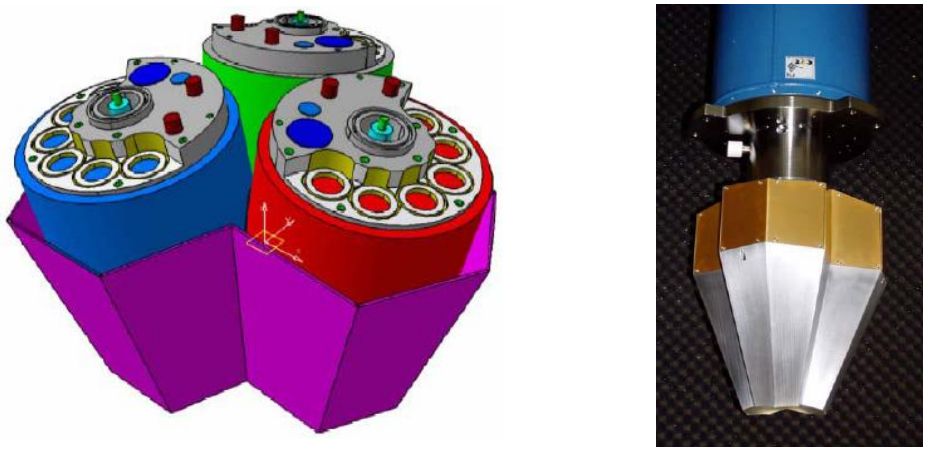

Fig. 3.3 - Left panel: technical drawing of an AGATA triple-cluster. Right panel: photo of a single AGATA triple-cluster.

3.1.3. *DIGITAL ELECTRONICS*

The use of Pulse Shape Analysis (PSA) techniques obviously requires that the shape of each pulse in the detector is recorded and processed digitally. For this reason, all 37 signals from each detector are digitised at 100 MHz immediately after the preamplifiers by high-resolution (14 bits) fast ADCs. Using the digitized signals the energy, time and position of each gamma ray interaction are then extracted using digital processing techniques. These data are associated with an unique timestamp and an unique positional label which will be used by the data acquisition processors to associate data produced by the same event.

Digital processing allows to use filters that have no analog counterpart such as the Moving Window Deconvolution algorithm [76] to reconstruct the original charge collection by removing the effect of the preamplifier response. A good energy resolution can be achieved with shorter shaping time; in this way the array is able to sustain a counting rate per detector 5 times higher than the "traditional" apparatuses (50 kHz per detector instead of 10 kHz).

3.1.4. *PULSE SHAPE ANALYSIS*

Simulations show that in order to reach a satisfactory efficiency, tracking algorithms have to be provided with information on the gamma interaction localization with a precision of at least 5 mm. Since it is technically unfeasible to obtain such a level of voxelization by physically segmenting the HPGe detector electrode, this information has to be extracted analysing the shape of the detector signal; Pulse Shape Analysis (PSA) is therefore crucial for determining the final tracking efficiency.

All pulse shape analysis techniques involve the comparison of the digitised pulses with a basis of reference signals, each of them corresponding to a well localised single interaction point. In fact, the input data for the PSA process for an AGATA detector consist in 37 signals $S_j(E,t)$, with $j = 0,1,\dots,36$, sampled at the output of the HPGe detector preamplifiers (36 segments + core). Since the detector response is linear, $S_j(E,t)$ can be written as the superposition of the signals associated to the single hits of the gamma $S_j(x_i,y_i,z_i,t)$ weighted by their energy release E_i:

$$S_j(E,t) = \sum_{i=1}^{N} E_i S_j(x_i, y_i, z_i, t) \qquad (3.1)$$

where N is the number of interactions inside the segment and $E = \sum_{i=1}^{N} E_i$.

In the case where $N = 1$, Eq. 3.1 reduces to

$$S_j(E,t) = E S_j(x_i, y_i, z_i, t) \qquad (3.2)$$

Solving this equation means finding the interaction point x_i, y_i, z_i that better reproduces the measured signal shape $S_j(E,t)$. This is done by comparing the measured signal shape with a set of shapes corresponding to known interaction points, called signal basis. In order to achieve a good position resolution, it is not sufficient to compare the net-charge signal of a segment with the basis, but the transient shapes in the neighbouring segments must also be compared to a basis for transient signals. If $N > 1$, there is the added complication of disentangling the single interactions of each segment, all with an unknown energy deposit and unknown position.

The comparison of waveforms is a very demanding task if performed in a naive way, more so if a decomposition of each signal shape in multiple interaction points is needed, because it requires a large quantity of memory and of CPU time; fast and efficient PSA algorithms are therefore needed. Many approaches to the "PSA problem" have been proposed: adaptive grid search [77], neural networks, matrix inversion [78], genetic algorithms [79], recursive subtraction [80], etc.

In the present experimental campaign, it has been decided to use a grid search algorithm because it is the only one with processing times small enough to be used in real-time applications. A basic assumption for this algorithm is that the size of a segment is small enough that multiple interactions inside the same segments can be ignored, so that the PSA is performed under the simpler case of Eq. 3.2 (N=1). While it is known that it is not a very realistic approximation, the effect on the overall performance of the detector has been found negligible [77].

Independently of the chosen algorithm, the quality of the PSA also depends critically on the signal basis that is used for the decomposition of the measured shapes. There is a large effort in the community to build an experimental signal basis [81-83], but it is not yet available due to the long times needed to build up the necessary

statistics while achieving a good precision on the reference positions. The basis used at the moment is obtained via detailed calculations of the charge transport through the detector [84], [85].

The reconstruction of the signal shape performed by PSA algorithms can also be used to increase the time resolution of a HPGe detector, compared with that obtained with a common approach based on a constant fraction discriminator. While such possibilities are under study [86], they were not employed for the present analysis.

3.1.5. GAMMA-RAY TRACKING ALGORITHMS

Typically, the distances between gamma-ray interaction points inside an HPGe detector are of some cm or less, and the time resolution of such a detector is of some ns: all interactions of a single gamma with the detector are therefore seen as simultaneous.

The task of a tracking algorithm is to time order the gamma interactions and to reconstruct the path of a gamma ray inside the detector, in particular with the Compton scattering formula. There are two main types of tracking algorithms, called forward tracking and backtracking, which we will now describe shortly.

In the forward tracking algorithm the first step is the identification of clusters of interaction points that may belong to a single gamma-ray. Looking at the forward peaking of Compton scattering cross-section, clusters are identified as a set of interaction points with an angular distance $\leq \theta_0$ between each other (link algorithm) or with respect to a given point (leader algorithm).

Secondly, each cluster is evaluated to determine whether it contains all the interaction points belonging to a single gamma-ray with the following criteria:

1: Do the interaction points satisfy the Compton scattering formula? In this case, the tracking algorithm uses the angle-energy relation of Compton scattering to determine the most likely scattering sequence from the position and energy of the interaction points:

$$\chi^2 = \sum_{j=i}^{N-1} W_j \left(\frac{E_{\gamma\prime} - E_{\gamma\prime}^{pos}}{E_\gamma} \right)_j^2 \qquad (3.3)$$

where E_γ is the sum of the deposits from j to $N-1$, and $E_{\gamma\prime}^{pos}$ is the energy of the scattered photons according to the Compton scattering formula. For a cluster of N interaction points, the $N!$ permutations are tested, and the cluster is defined as "good" if the χ^2 is below a predetermined threshold.

2: If the cluster is composed by a single interaction point, does the energy satisfy photoelectric conditions? The algorithm evaluates if

$$depth \leq k\,\lambda(e_1) \qquad (3.4)$$

where λ is the free mean path, and e_1 is the energy deposited. In this case, a Monte Carlo-like approach is taken to decide if to consider the interaction point as an actual photoelectric event or if to discard it as an isolated Compton scattering event.

3: Do the interaction points correspond to a pair production event? If there are two gamma-rays of energy equal to 511 keV and an interaction point in the middle with energy greater than 1022 keV, the three energies are summed and considered as a single gamma-ray.

The algorithm tries to recover some of the wrongly identified clusters. For example, one type of incorrectly identified cluster comes from a single gamma-ray being separated into two clusters. This gamma-ray can be correctly identified by tracking together all pairs of bad clusters. When the result gives a small χ^2 , the gamma-ray is recovered by adding the two clusters.

The clusters which do not satisfy any of the above criteria are rejected, thus improving the P/T (peak to total) ratio of the spectra without the need for Compton suppression shields. If a large solid angle is covered with segmented germanium detectors, the combination of PSA and gamma-ray tracking allows for a very high photopeak efficiency together with a good P/T ratio.

An example of this method is represented in figure 1.16, where a high-multiplicity event is considered: the coloured dots represent single interaction points of gamma-rays inside a 4π detector shell; the red circles correspond to clusters of interaction

points identified by the tracking as belonging to a single gamma-ray, while the green squares correspond to clusters that are discarded.

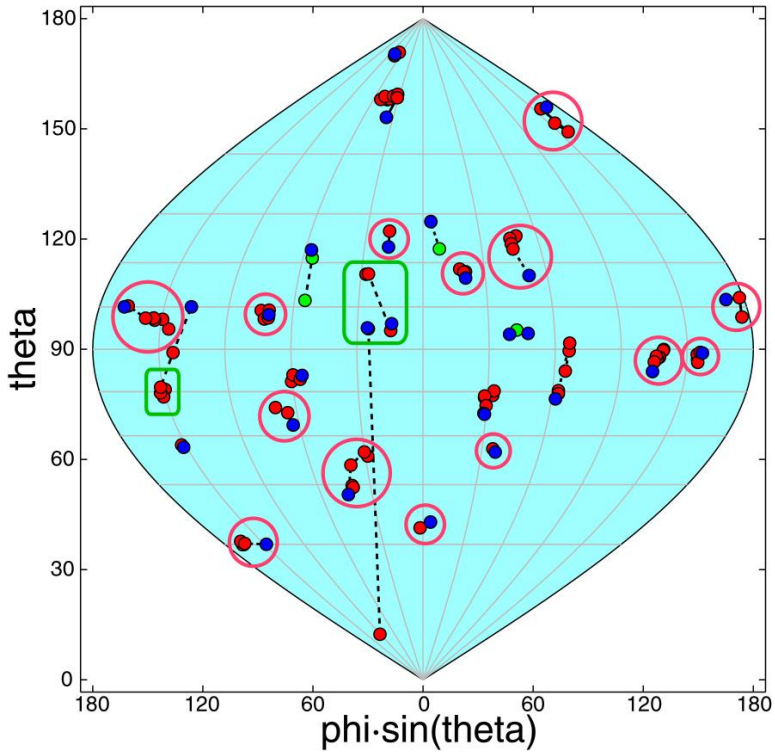

Fig. 3.4 - Plot of all interaction points in a 4π HPGe shell from a simulated event with 30 gammas of 1.3 MeV; red circles represent clusters which are identify as belonging to a single gamma-ray, while green squares represent clusters that are discarded by the tracking.

The forward tracking algorithm is the basis for the Mars Gamma-ray Tracking (MGT) code [70] that was used both for the experimental data and the GEANT4 simulations.

The backtracking algorithm [87] is based on the fact that the photoelectric energy deposition is almost independent from the incident energy and is peaked around 100-250 keV; it assumes that the interaction points within a given deposited energy interval $e_{min} \leq e_i \leq e_{max}$ are the last interaction (in time) of a fully absorbed gamma-ray; the algorithm then finds the closest interaction to the photoelectric one, it computes the scattering angle using the incident and the scattered energies and, finally, it searches for the other previous interactions along this direction; such process is iterated until the direction points directly to the target. This algorithm,

however, was found to be less efficient and showed a worse P/T in the reconstructed spectra [88], and was therefore not used for our analysis.

3.1.6. THE DEMONSTRATOR PHASE OF AGATA

It has been planned by the international collaboration that the development of AGATA will proceed in stages, with the construction of the full array preceded by a final R&D phase aimed at building a subsystem of 5 triple clusters, called the Demonstrator.

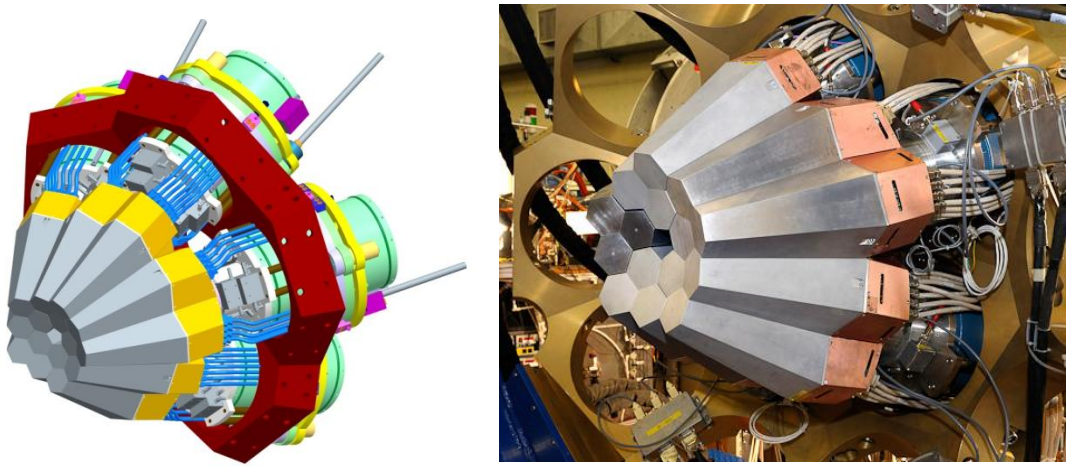

Fig. 3.5 - Left panel: technical drawing of the AGATA Demonstrator. Right panel: photo of the AGATA Demonstrator installed at Legnaro National Laboratories.

The Demonstrator, together with its digital electronics, DAQ and full on line processing of the digitized data, has been installed in LNL in 2008 and has been used in various physics experiments from 2009 to 2011. The aim of the experimental campaign of the Demonstrator is to confirm the effectiveness of the gamma-tracking concept in real measurement conditions. A technical drawing of the full Demonstrator can be seen in the left panel of Fig. 3.5, together with a photo of the Demonstrator installed at LNL in the right panel.

In a conventional array of germanium detectors, a collimator is placed in front of each detector in order to minimize the scattering of photons between different crystals. Therefore, only a small region around the target position is actually visible from the detectors. In the case of the AGATA Demonstrator, no collimators are present, and thus it is possible to modify the position of the detectors with respect to

the target position. In particular, due to the lack of spherical symmetry of the Demonstrator, it is feasible to place the detectors closer to the target position compared to the reference 23.5 cm distance of the full AGATA array and cover a larger solid angle. The simulated photopeak efficiency as a function of the shift towards the geometrical centre is shown in Fig. 3.6. In the case of the experiment described in this thesis, a shift of 10 cm was applied, that is the maximum allowed by mechanical constraints (in particular, because the outer radius of the scattering chamber is 13 cm).

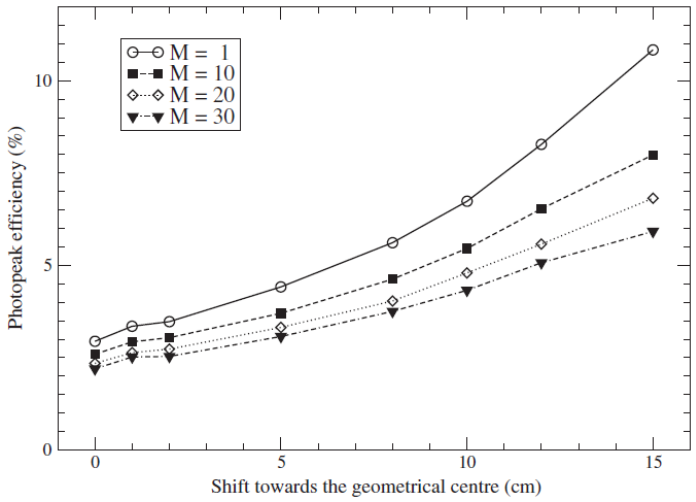

Fig. 3.6 - Photopeak efficiency of the AGATA Demonstrator as a function of the distance of the detectors from the reference position. Taken from [74].

3.2. THE SILICON TELESCOPES

Two ΔE-E silicon telescopes were used for our experiment, each with a thin "ΔE" detector in front of a thick "E" detector. The ΔE detectors were 200 μm thick, corresponding to an energy loss of about 70 MeV for an ^{17}O ion of 340 MeV (20 MeV/u). The E detectors were 1 mm thick, enough to stop the ^{17}O ions completely.

Each detector is segmented in 60 pads of 4 x 4 mm^2, for an active area of 20 x 48 mm^2. The large active area allows for a good solid angle coverage, and the segmentation for a higher counting rate limit. Furthermore, the detectors have for each pad a much better energy resolution compared to a non-segmented Si detector of the same total area: the electrical noise of a solid-state detector is proportional to

its capacity, which is in turn proportional to the detector surface area for a planar geometry.

It should be noted that for each detector we have a total of 61 output channels: one for each pad, and one from the non-segmented "back" side. For 4 detectors, we therefore would need the rather large number of 244 channels of front-end electronics. However, due to physical constraints, the detectors can only be placed inside the scattering chamber at a distance of ~ 7 cm from the target, covering a solid angle of ~100 msr per telescope and an angular range of about 25°. As the DWBA calculations show (see §2.4), such angular range is much larger than the one needed to detect the Giant Quadrupole Resonance in ^{208}Pb and ^{90}Zr.

For this reason, an ad-hoc adapter board was built, which selects the 32 pads closest to the beam direction (as shown Fig. 3.7, right panel) and connects them to the charge pre-amplifiers and to the rest of the electronics: in this way, we reduced by a factor of 2 the number of electronics channels needed, without losing efficiency in the region of interest. Fig. 3.7, left panel, shows a photograph of one of these adapter boards: to the left are two input connectors for high-density (68 pin) cables, carrying each 32 signals, corresponding to all the pads and the back signal; to the right is the output connector which carries only the signals of the selected pads and the back.

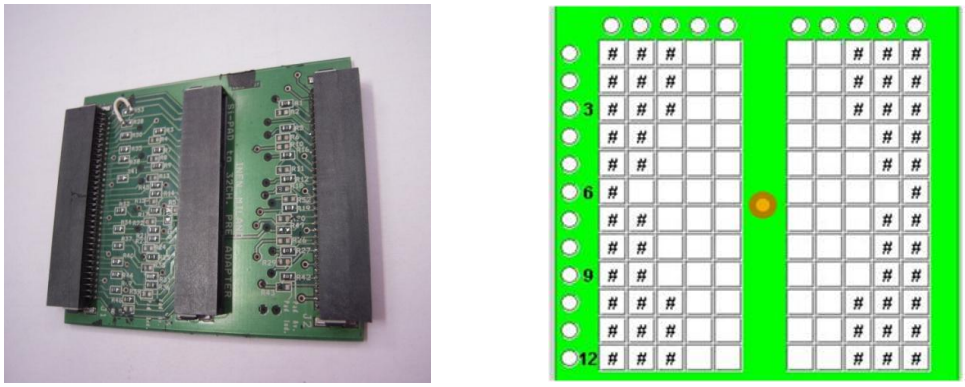

Fig. 3.7 - Left panel: photograph of one adapter board, which selects the signals corresponding to the pads closest to the beam direction out of all the pads of one Si detector. Right panel: schematic view of the detector pads connected to the DAQ. The spot in the centre represents the beam position. Note that the 2 pads in the column farthest from the beam were connected together, in order to leave 1 channel free for the "back" signal.

Each detector was connected to a custom 32-channels charge preamplifier. The preamplifiers were mounted as close to the detectors as possible, exploiting the space normally occupied by the MCP detector of the PRISMA magnetic spectrometer [71]. The preamplifiers were placed on a metallic board to favour heat dispersion, as seen in Fig. 3.8, right panel; the left panel shows a single 32-channel preamplifier board.

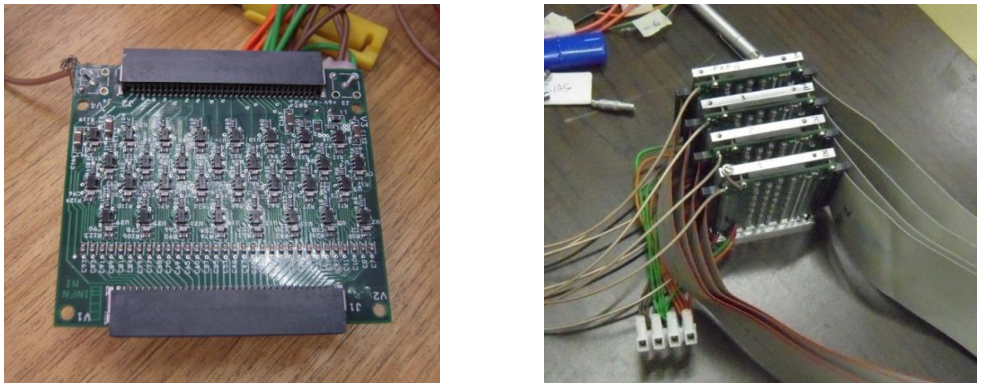

Fig. 3.8 - Left panel: photograph of one of the 32-channel preamplifiers used for the Si telescopes. Right panel: photograph of all 4 preamplifiers, mounted on a metal plate to favour heat dispersion. The flat cables on one side connect the preamplifiers each to a detector, the cables on the other side connect them with the flange. The yellow cables are for the test signals and for the detector bias. The red, green and brown cables are for the power of the preamplifiers.

The preamplifiers were under vacuum, and were connected through high-density cables to a flange and from the flange to an active circuit splitting the signals of each into 2 standard flat cables. Each of these cables was the input of a CAEN N1568 16-channel spectroscopic amplifier, set with a shaping time of 2 μs. The output of the amplifiers was then sent to the CAEN V879 ADCs (Analog to Digital Converters) for data acquisition. Each amplifier channel also had a built-in CFD (Constant Fraction Discriminator), that was sent to the CAEN V878 TDCs (Time to Digital Converters). Finally, the amplifiers also have a "OR" output that is the logical "OR" of all the 16 CFD channels, and is used to build the trigger condition (see §3.5).

The detectors were mounted on a mechanical support that allowed to change angular position of both telescopes with respect to the beam direction, due to the different requirements of the ^{208}Pb and ^{90}Zr targets (see also Fig. 2.3). The minimum

angle covered by the detectors varied from 8° to 17°, measured in the centre of the first column of pads. The distance between the target centre and the ΔE detectors was ~7 cm. The detectors can be seen mounted in the scattering chamber in Fig. 3.9.

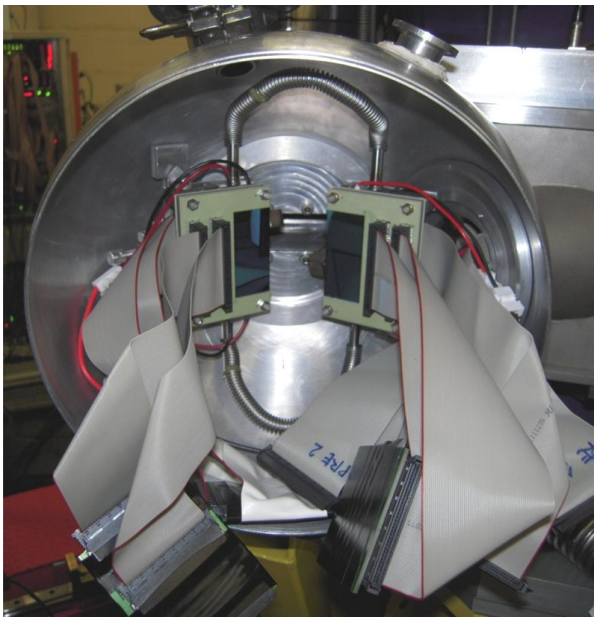

Fig. 3.9 - Photograph of the TRACE telescopes inside the scattering chamber; only the back contact of the ΔE detectors is visible. The high-density flat cables are also visible, in grey, as well as the pipes for the cooling system. The adapters of Fig. 3.7 can be seen at the bottom, covered in insulating black tape.

Two Peltier cells were placed behind each of the telescopes in order to cool them to a temperature of about -20 °C. In order to guarantee a good heat transfer, the detectors were mounted in aluminium oxide PCBs (Printed Circuit Boards) and brass dices were used to fix the ΔE detector to the E detector. The hot side of the Peltier cells was in turn cooled by a refrigerant liquid kept at ~10 °C by a chiller system; the pipes of the cooling system can be seen clearly in Fig. 3.9.

The detectors used for this experiment are the prototypes for the TRacking Array for light Charged particle Ejectiles (TRACE), a 4π array of segmented E-ΔE silicon telescopes, designed for the detection of protons and alpha particles in experiments with fusion-evaporation and direct reactions.

3.3. THE $LaBr_3$:CE SCINTILLATORS

Ever since they were first produced in 2001, $LaBr_3$:Ce detectors have attracted a great deal of attention in the gamma spectroscopy community, because they couple the best properties of inorganic scintillators (high efficiency, good time resolution) with an energy resolution surpassed only by that of germanium detectors.

For these reasons, the gamma spectroscopy group of the University of Milan has been working on the development of such detectors [89-94], in particular concerning the front-end electronics. For our experiment, one cylindrical 3" x 3" and two cylindrical 3.5" x 8" $LaBr_3$:Ce detectors were used.

The principal reason for the good energy resolution of $LaBr_3$:Ce detectors is the high light yield (63 photons/keV, compared to 38 photons/keV of NaI). This unfortunately also causes a saturation of the PhotoMultiplier Tube (PMT) for high-energy signals, which in turn brings to a nonlinearity of the detectors. Our group is working on ad-hoc electronics to prevent the problem [93], but at the time of the experiment its development was still at the early stages. For this reason, we acquired both the signal from the anode of the PMT and from one of the dynodes: the signal at the dynode received less amplification and has therefore a worse signal-to-noise ratio but a better linearity.

The anode signals were sent to the BaFpro shaping amplifier (see §3.4), 3 channels of which were adapted for $LaBr_3$:Ce detectors, while a standard NIM electronics chain was used for the dynode signals. Both types of energy signal were sent to a CAEN V879 ADC. The time signals from the BaFpro module were sent to a CAEN V878 TDC.

The detectors used for our experiment are now part of a larger array of $LaBr_3$:Ce crystals, called HECTORplus, being intended as an upgrade of the HECTOR array [95]. The full HECTORplus will be composed by 10 $LaBr_3$:Ce detectors of 3.5" x 8".

3.4. THE BaF_2 SCINTILLATORS

The remaining solid angle available was covered with 20 small volume (2.5"x3") BaF_2 detectors from the HELENA array, grouped in 2 clusters of 8 detectors and 1 cluster of 4. The detectors covered ~30% of the solid angle.

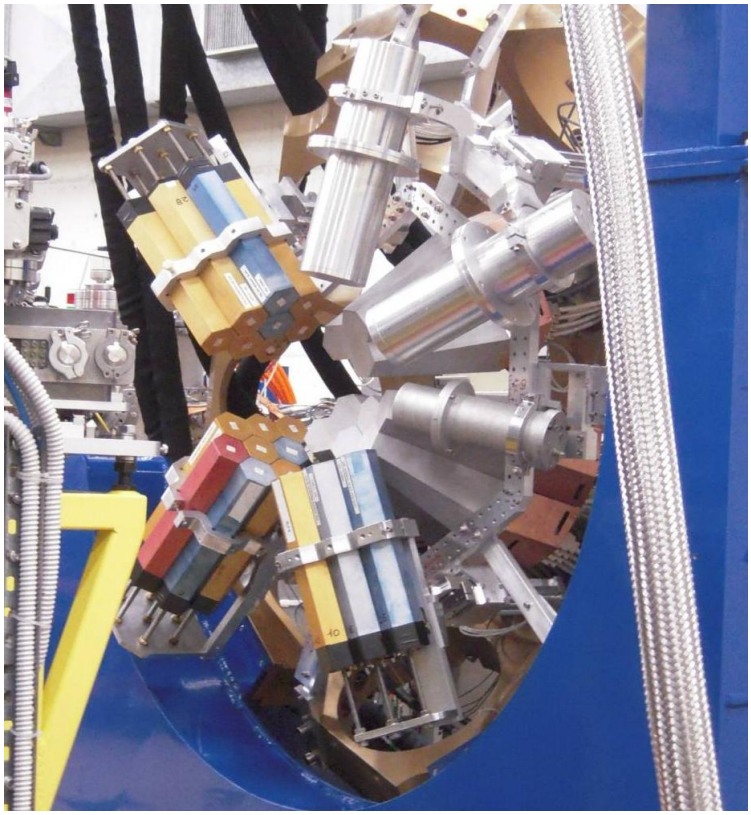

Fig. 3.10 - Photograph of the gamma detector setup used for our experiment: the 3 HECTORplus $LaBr_3$:Ce scintillators are the cylindrical detectors to the right, the HELENA BaF_2 scintillators are grouped in the 3 coloured clusters of detectors to the left and bottom, while the 3 HPGe triple-clusters of the AGATA Demonstrator are in the middle.

The typical use of the HELENA crystals is to act as multiplicity filter, but the large total volume of each cluster makes it possible to use them also for the detection of high-energy gamma-rays.

The signal of each HELENA crystal was sent to a channel of two BaFpro modules [96]. BaFpro is a custom spectroscopy amplifier developed in Milan for the shaping of BaF_2 signals; it has 16 channels and for each of them it gives a "fast" and a "slow" output, corresponding to the fast and slow components of the signal, as well as a "time" output obtained by a CFD.

A photo of all the gamma detectors used in the experiment is shown in Fig. 3.10. The large cylinders on the top-right side are the aluminium casings of the $LaBr_3$:Ce

detectors; the coloured hexagonal clusters in the left-bottom part are the BaF_2 detectors; the AGATA clusters can be seen behind the scintillators.

3.5. The Data Acquisition System

As mentioned in §3.1, the electrical contacts of each AGATA detector are segmented 36-fold, and the digitizers sample the pulses from each segment at 14 bits precision with a frequency 100 MHz; for every accepted event, a pulse trace of 60 samples is extracted and acquired. With a counting rate of 50 kHz/crystal the dataflow for each detector is therefore of the order of 100 MB/s (with zero suppression). Furthermore, in order to have an online analysis, the PSA has to be performed in real time for each of the acquired traces, and tracking algorithms must reconstruct the detected gamma-rays from the PSA information.

This means that the DAQ software for AGATA has to be able to handle large quantities of data, control a computing farm for the PSA and tracking algorithms, and coordinate the flow of information between the digitizers, the computing farm, and the disk server where all the data are written. All of this is performed by a NARVAL-based DAQ software [72].

The ancillary detectors (TRACE, HECTORplus, HELENA) were controlled by an independent DAQ run on a KMAX environment [73], which communicated with the VME crate via an optical fibre and with NARVAL via TCP/IP.

In NARVAL, each task is performed by an actor, associated to a process running on a Linux machine; actors communicate with each other with a UNIX fifo if running on the same machine or with a TCP/IP socket if running on different machines. There are 3 types of actors:

- producer: they interface with the hardware and read out the data
- intermediary: they perform operations on the data, receiving input and sending output from/to one or more other actors
- consumer: they can only receive input from the other actors, and store the data to disk or act as histogrammers

From the point of view of NARVAL, each AGATA crystal is considered as a separate entity and the whole detector may be considered as the aggregation of synchronized data supplied by the individual crystals. The synchronization is guaranteed by the AGATA Global Trigger and Synchronization (GTS) hardware with a common 100 MHz digital clock.

For each AGATA detector there is a producer actor reading the pulse traces from the front-end electronics; the traces are sent (together with the timestamp information) to an intermediary that performs the PSA and to a consumer that writes them to disk; the PSA data from all detectors are sent to an intermediary that acts as event builder, matching the data from different detectors through the timestamp information.

For the ancillary detectors, there is a producer actor that receives the data from the KMAX acquisition, kept synchronized to the GTS via the AGAVA (AGATA Ancillary VME Adapter) module. The producer sends the VME data to a consumer that writes them to disk and to an intermediary that decodes the VME words and sends only the actual data words to the event builder, discarding VME header and trailer words. The builder then matches the ancillary data to the AGATA data and sends the event to another intermediary that performs the online tracking.

3.6. TRIGGER CONDITIONS

When a gamma-ray is detected in an AGATA crystal, a trigger request is formed and sent via the GTS to the trigger processor, which can validate the request, meaning that all the traces for the event are acquired, written and processed, or reject it. This software trigger can be used to make multiplicity requirements on the AGATA crystals, or to make a coincidence between AGATA and the ancillary detectors via the AGAVA module.

This method, however, was not suitable for our experiment due to the complexity of our trigger condition. Therefore, we used standard NIM electronics to build the master gate, which was sent via AGAVA as a trigger request, and had the software trigger validate it. The master gate is schematically described in Fig. 3.11 and is the logical "OR" of four conditions:

- the coincidence between TRACE and AGATA
- the coincidence between TRACE and the scintillators
- the TRACE scaled-down singles
- the scintillators scaled-down singles

where the AGATA trigger was made using the analog output of each AGATA detector (present for debug purposes), sent to standard CFD modules and to a logical OR; the TRACE trigger was the OR of all the pads of the two E detectors, taken from the amplifiers; and the scintillator trigger was the OR of all the HELENA and HECTORplus detectors, taken from BaFpro.

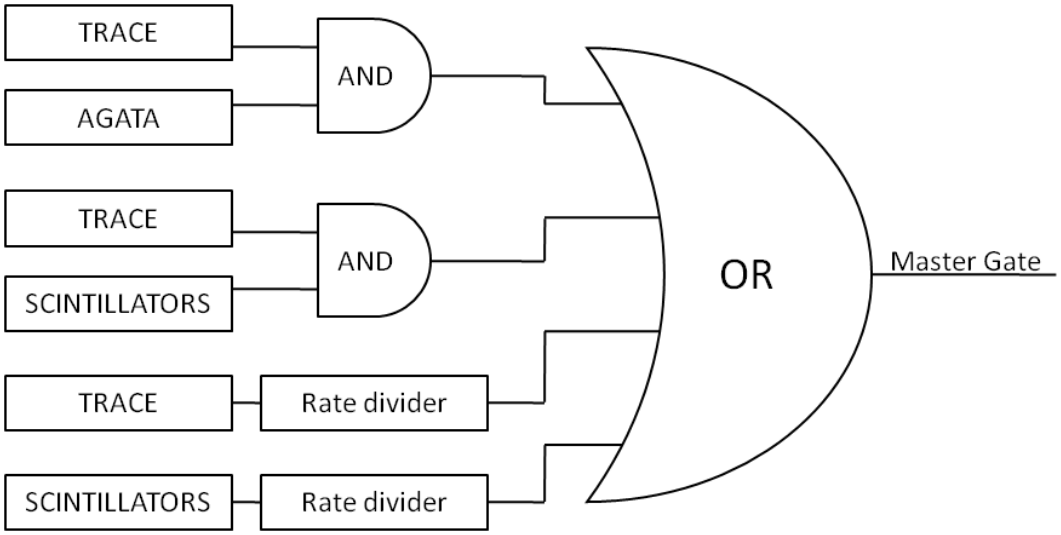

Fig. 3.11 - Logic view of the trigger conditions.

In order to separate the different classes of event, 4 channels of the TDCs were used as markers.

The coincidence between TRACE and the gamma detectors was set up in such a way that the gate opens when there is a signal in one pad of the E detectors, as illustrated in Fig. 3.12:

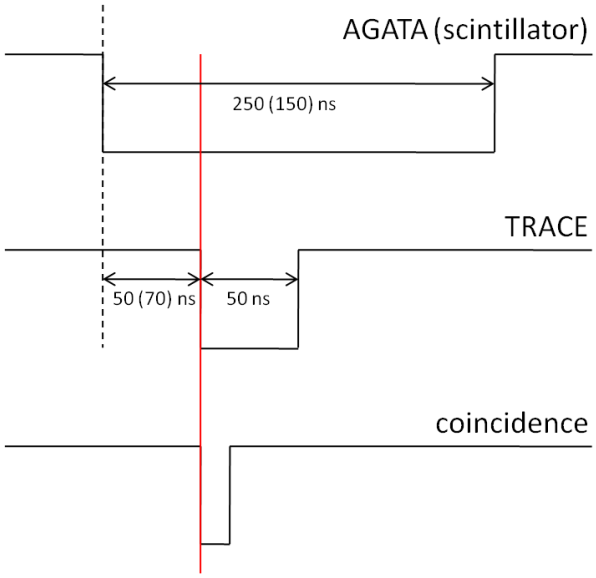

Fig. 3.12 - Schematic view of the time window for the AGATA-TRACE coincidence. The values between parentheses are for the scintillator-TRACE coincidence.

In this way both types of coincidence events (TRACE-AGATA and TRACE-scintillator) have a common time reference, since in both cases the Master Gate is opened by the TRACE E detectors.

Chapter 4. Analysis of the Si telescope data

The silicon telescopes were used for the identification of the reaction channel and for the measurement of the excitation energy transferred from the projectile to the target. It will be first shows in §4.1 how many of the pixels of the detectors were working correctly, in §4.2 how we interpreted the structures visible in the time spectra, and in §4.3 how we calibrated the detectors. In §4.4 the identification plot for the reaction channels will be shown, and in §4.5 the excitation spectra in the region of interest for the study of giant resonances.

4.1. WORKING CONDITIONS OF THE DETECTORS

During the experiment, a total of 62 signals from the Si telescopes were sent to the DAQ. Unfortunately, due to various problems, such as faulty amplifier channels or damaged cables, a number of these signals was lost. This is shown in Fig. 4.1 for both the measurement with the ^{208}Pb target (left panel) and the ^{90}Zr target (right panel). For each matrix, the yellow squares correspond to the pads that were working, the grey squares correspond to the pads that were broken and the white ones to the pads that were not connected to the DAQ (see Fig. 3.7).

There are some particular cases, for which a typical E-ΔE matrix is shown Fig. 4.2:

- the pads marked with a red "C" show a much larger counting rate than the others and a large contamination from the elastic scattering channel (which in principle should be eliminated by the coincidence requirement in the trigger, see §3.5).
- the pads marked with a grey "L" are working but have such a low counting rate that they were discarded because they gave no significant contribution to the statistics.
- the orange pads marked with an "S" show some spurious structure in the identification plot; in the red pads only that structure is visible, and were not considered for the analysis

^{208}Pb

	0	1	2	3	4	5	6	7	8	9
0				L						
1				L						
2						C				
3			L		C	C				
4					C	C	C			
5					C	C				
6						C				
7					C	C				
8			L			C				
9										
10				L						
11				L	L					

^{90}Zr

	0	1	2	3	4	5	6	7	8	9
0				L						
1				L	L					
2				L						
3			L							
4			L	S	S	C				
5			L	S	S	C				
6					S	C				
7				S		C				
8								L		
9				L	S					
10				L						
11				L	L	L				

Fig. 4.1 - Schematic view of the working conditions of the TRACE telescopes, for the ^{208}Pb target (left panel) and for the ^{90}Zr target (right panel).

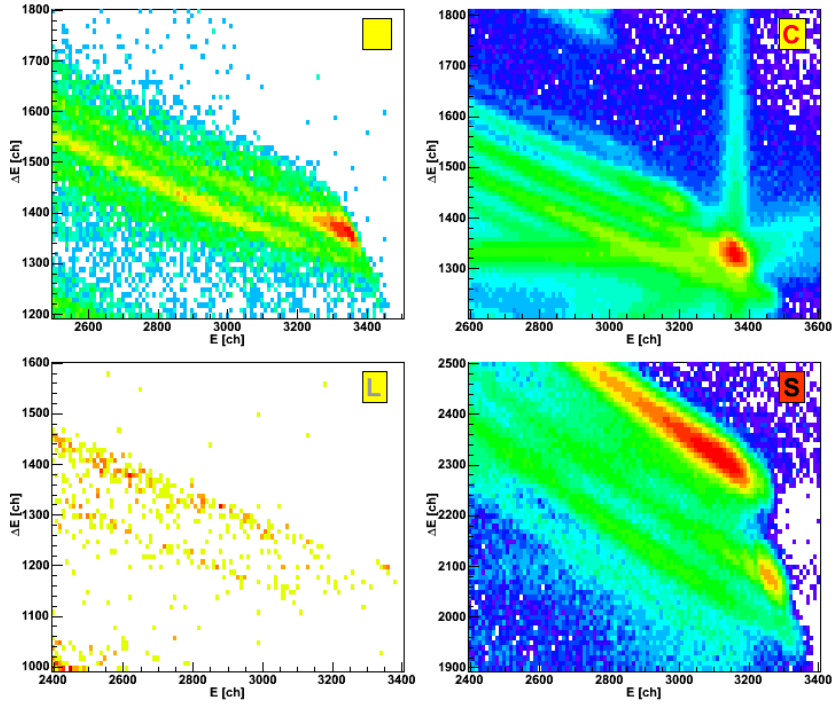

Fig. 4.2 - Scatter plot of the energy deposit measured in one pad of the ΔE detectors versus the energy deposit in the corresponding pad of the E detectors, for 4 pads of the TRACE telescopes. Note that raw data were used for these plots. The 4 plots correspond to the different types of pad in Fig. 4.1, see text for a complete description. All plots were obtained with the ^{90}Zr data, similar plots are obtained with the ^{208}Pb data.

4.2. TIME SPECTRA

During the experiment, a time signal was acquired for each pad of the Si detectors by 2 VME Time-to-Digital Converters (TDCs). The TDCs worked in "common start" mode: each TDC channel is started by the master trigger (cfr §3.6) and is stopped by the delayed time signal of a Si pad. Note that this means that the start of all the TDCs is given by the E detectors in case of a TRACE-gamma coincidence (see also Fig. 3.12).

Fig. 4.3 shows, in black, the time spectrum for one pad of the E detectors and the spectra obtained in coincidence with the different markers as described in the legend (cfr §3.6). The narrow self-coincidence peak present in the red and green spectra corresponds to the events in which the pad in question was the one to open the master trigger in the case of a particle-gamma coincidence. The peak in the blue spectrum instead corresponds to the same self-coincidence in the case of TRACE scaled-down singles. The purple spectrum, corresponding to the random coincidences of the E detector with a scaled-down "scintillator single" event, is mostly empty, probably because they fall outside of the time window of the TDC.

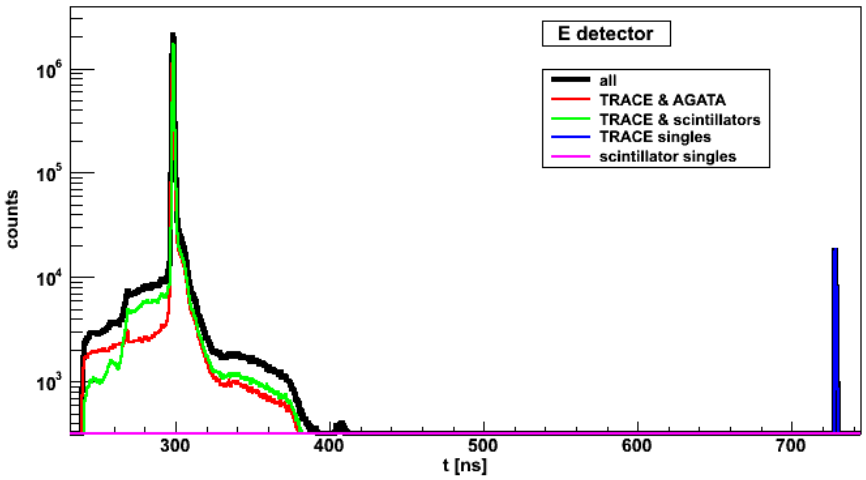

Fig. 4.3 - Typical time spectra for one pad of an E detector. The black line corresponds to the spectrum without any gating condition, while the coloured spectra are in coincidence with the various trigger markers, as indicated in the legend (see also §3.6).

Fig. 4.4 shows instead the time spectrum for one of the pads of the ΔE detectors in coincidence with the various trigger markers. The strongest peak in the red and

green spectra corresponds to the coincidence of the ΔE pad with the E pad behind it; the same holds for the peak in the blue spectrum for the case of Si singles.

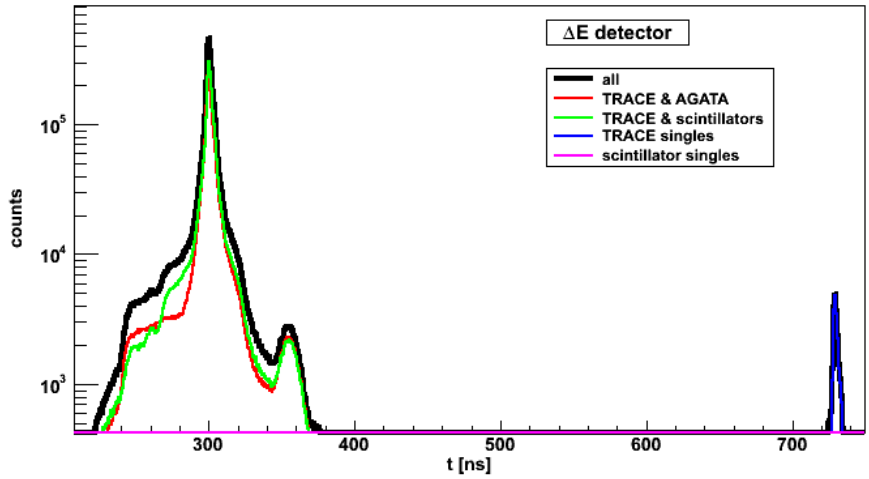

Fig. 4.4 - Typical time spectra for one pad of a ΔE detector. The black line corresponds to the spectrum without any gating condition, while the coloured spectra are in coincidence with the various trigger markers, as indicated in the legend (see also §3.6).

The timing of the Si detectors is affected by the large spread in energy (and time of flight) of the various reaction products. For this reason, we also show in Fig. 4.5 the time spectrum obtained by gating on the ^{17}O scattering reaction channel (see also §4.4), for both one pad of the E (left panel) and of the ΔE (right panel) detectors.

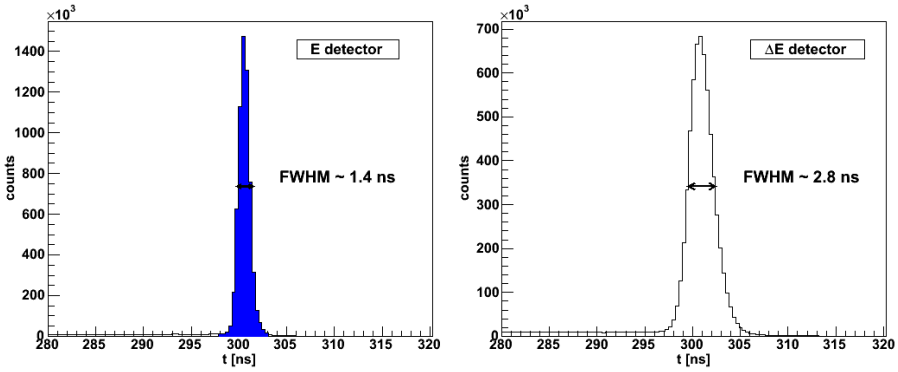

Fig. 4.5 - Time spectra for one pad of the E (left panel) and ΔE (right panel) Si detectors, under the gating condition that an ^{17}O ion is detected in the pad. The blue area marks the interval of time for the E detector that is assumed as "good" when performing a time gate for the detector.

The FWHM of the peak for the ΔE detector is ~3 ns and is due to the sum of the time resolutions of both the E and ΔE detectors. For the rest of the analysis, all TRACE spectra were gated on the time peak of the E detector, marked in blue.

4.3. DETECTOR CALIBRATION

The energy calibration of charged particle detectors with radioactive sources is only possible up to a few MeV of energy, since there are no long-lived emitters of alpha particles with higher energies. For this reason, the charge preamplifiers used in our experiment had a "test" input channel that was redirected to the 32 output channels. Knowing the sensitivity of the preamplifiers, 4.5 mV/MeV, we were able to calibrate each pad of the E and ΔE detectors up to 300 MeV.

Fig. 4.6 shows a calibration spectrum for one pad of one E detector. The FWHM of the peaks is of ~4 channels, equivalent to ~400 keV, which is a measure of the electronic noise of our system.

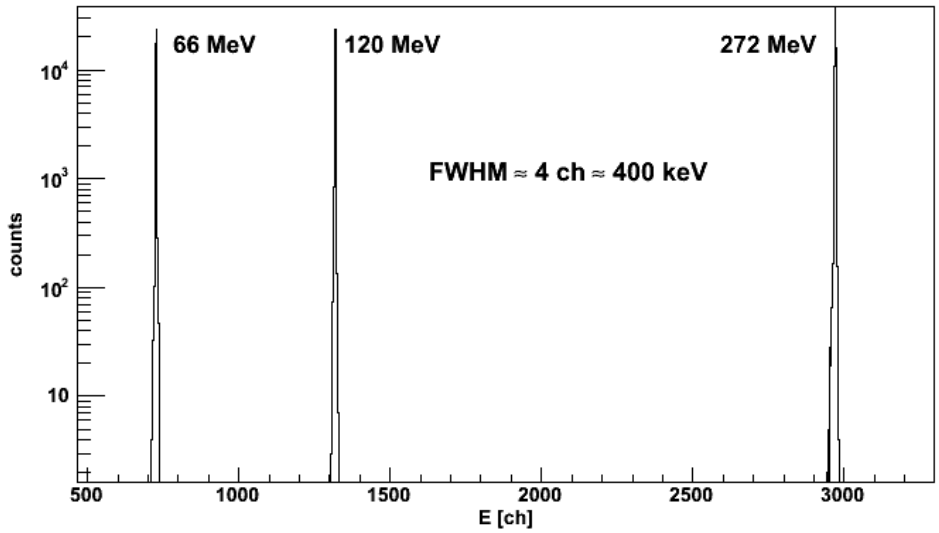

Fig. 4.6 - Typical calibration spectrum for one pad of the TRACE telescopes. The lines are made with a pulser sent as an input through the test channel of the preamplifiers. The equivalent energy of the lines is calculated with the design sensitivity of the preamplifiers.

Once the E and ΔE detectors are calibrated, it is possible to sum the energy deposit in each ΔE pad with the deposit in the E pad behind it, obtaining a measure of the Total Kinetic Energy (TKE) of the ions stopped in each pad of the telescope. Due to a

problem with the pulser used for the calibration, the slope of the calibration had to be corrected by a fixed scaling factor, applied to both E and ΔE detectors.

Fig. 4.7 shows the TKE spectrum measured in one pad, as well as the TKE spectrum obtained by gating on the ^{17}O scattering channel (see §4.4); the broad structure at 20-50 MeV is caused by alpha particles.

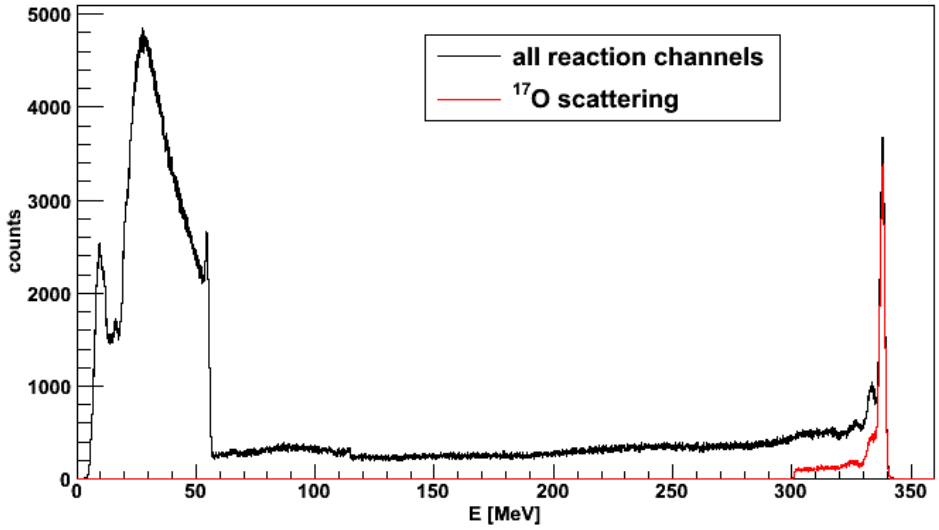

Fig. 4.7 - TKE spectrum measured with the ^{208}Pb target in one pad of the TRACE telescopes; the red spectrum corresponds only to the scattering of ^{17}O; the broad structure at 20-50 MeV is caused by alpha particles.

It should be noted that the nominal sensitivity of the preamplifier, used to calibrate the detectors, is just an average value, and that there are slight gain differences from channel to channel. For this reason, a fine calibration of the detectors was performed. Due to the energy straggling, the energy resolution in the E and ΔE detectors is worse than the resolution obtained for the TKE: for this reason, we decided to perform the fine tuning of the calibration by fitting the elastic peak in the TKE spectrum for each pad, without recalibrating the E and ΔE energies individually.

The average energy resolution was found to vary between 2 MeV and 3 MeV, which is worse than the design value but still good enough for our purposes.

4.3.1. DRIFT CORRECTION

During the course of the experiment, the leakage current passing through the detectors has steadily increased, due to the radiation damage caused by the scattered beam. This effect also causes a gradual loss of energy resolution and a variation over time of the energy gain for the pads that were more damaged by radiation, namely those suffering a higher counting rate, marked with a red "C" in Fig. 4.1.

These effects can be clearly seen in Fig. 4.8, where the TKE for two different pads is shown in relation to time (measured by the event counter): the pad to the left is stable, while the pad to the right has a clear drift of the elastic peak energy, as well as a degradation of the energy resolution.

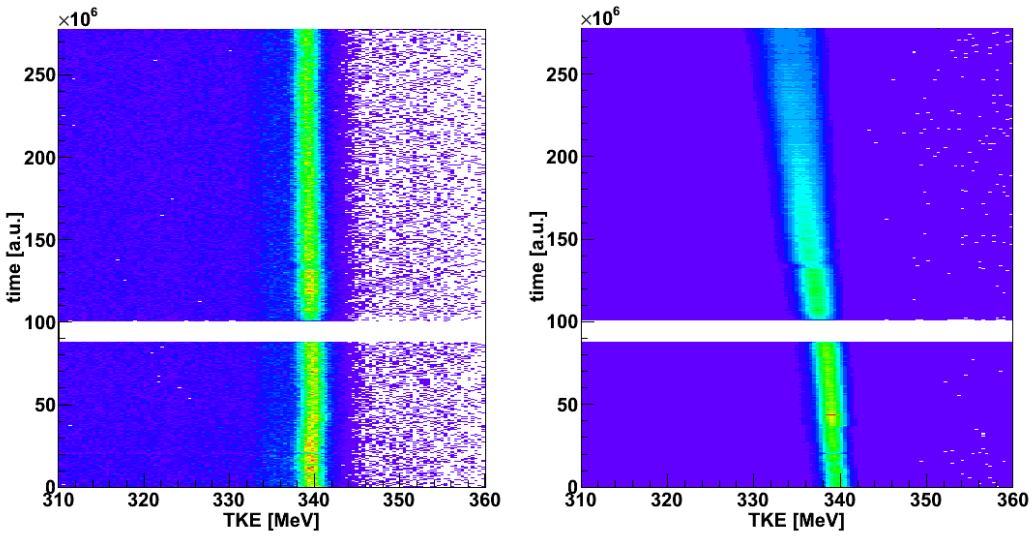

Fig. 4.8 - Scatter plot of the energy measured in two different pads of the TRACE telescopes versus the time of acquisition. The left panel shows one pad with small gain drift over time, while the right panel shows one pad with a large gain drift over time. The horizontal gap is caused by a problem of the ancillary DAQ.

The drift was corrected by performing a fit of the elastic peak every ~5 million events, thus obtaining a series of recalibration coefficients that were used for an event-by-event correction. The result is shown in Fig. 4.9, left panel, for the same pad that is shown in Fig. 4.8, right panel. Fig. 4.9, right panel, shows the improvement in energy resolution obtained thanks to this correction.

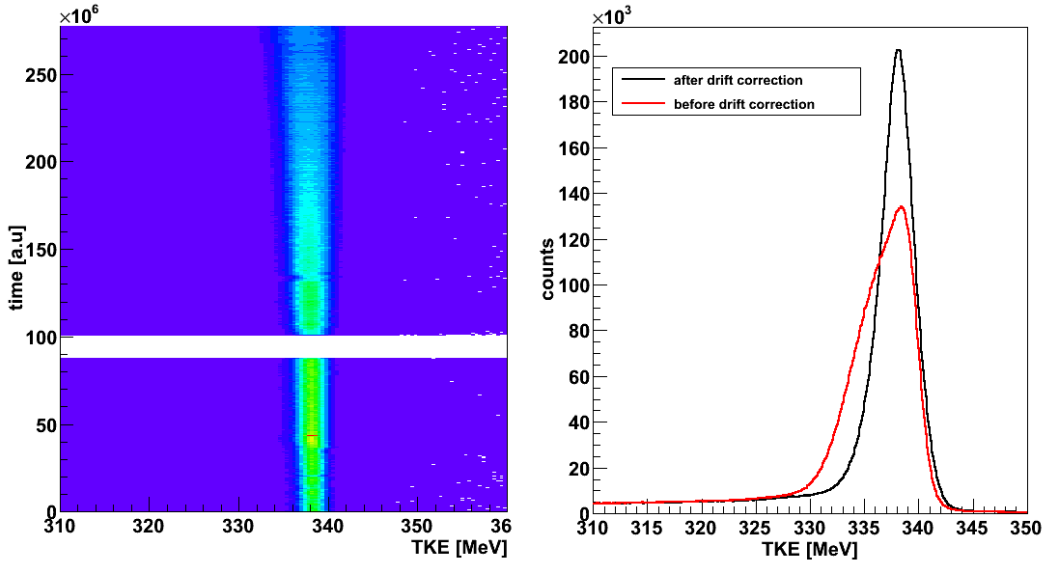

Fig. 4.9 - Left panel: scatter plot of the energy measured in one pad of the TRACE telescopes with a large gain drift after the correction. The horizontal gap is caused by a problem of the ancillary DAQ. Right panel: Total Kinetic Energy spectrum measured in the same pad before (in red) and after (in black) the correction for the gain drift.

4.4. EJECTILE IDENTIFICATION

The identification of the ions detected in the Si telescopes was performed with the standard ΔE-E technique.

Fig. 4.10, left panel, shows a typical ΔE-TKE matrix obtained for one pad. All the ions from He to F are clearly separated, and for each of them there's a clear mass separation. Note in particular the separation of the 3 main oxygen isotopes, as seen in the right panel of Fig. 4.10. The straight horizontal and diagonal structures seen in the matrix are due to a bug in the firmware of the CAEN ADC.

In the subsequent analysis, the events corresponding to ^{17}O scattering were selected by requesting that 1 pad had ΔE, TKE values inside the ^{17}O stripe (that is, inside the black line seen in Fig. 4.10, right panel), as well as the time signal of the E detector inside the self-coincidence spike (see Fig. 4.5), while all the other pads were requested to have no signal.

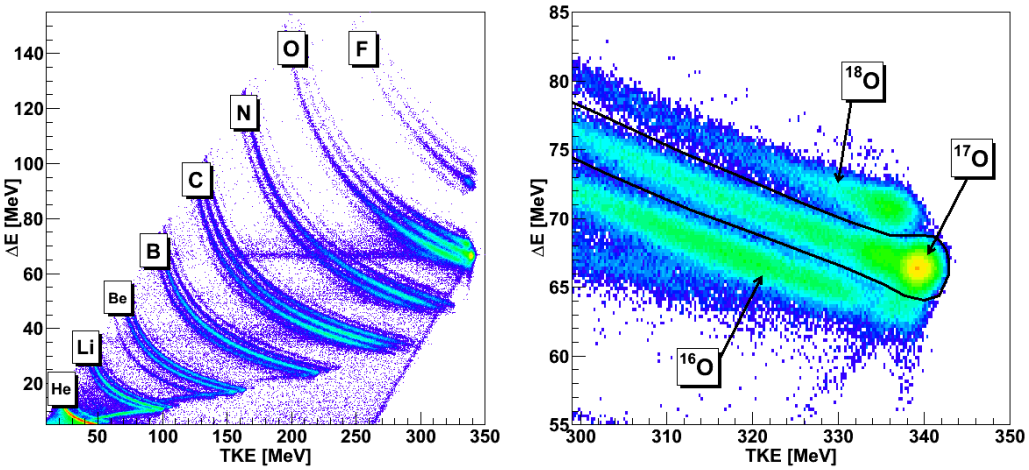

Fig. 4.10 - Scatter plot of the Total Kinetic Energy measured in one pad of the TRACE telescopes versus the energy deposit measured in the ΔE pad. The left panel shows the full range of ions that were measured, while the right panel shows the separation between the oxygen isotopes.

Fig. 4.11 shows the total number of ^{17}O scattering events detected in each pad for the ^{208}Pb (left panel) and ^{90}Zr (right panel) measurements. It can be seen that for both datasets, the pads in the right telescope have larger statistics than the pads in the left telescope, meaning that they also had a larger counting rate. This is most likely due to a wrong positioning of the detectors, possibly due to a design error in the mechanical support.

^{208}Pb

	2	3	4	5	6	7
0						
1			6.27E+3	2.54E+4	7.62E+3	
2		4.29E+3	2.14E+4	2.47E+5	2.80E+4	
3		1.34E+4	1.02E+5	1.28E+6	1.62E+5	1.96E+4
4	3.07E+3	2.04E+4	2.34E+5	4.73E+6	5.03E+5	3.08E+4
5	4.01E+3	2.76E+4	2.80E+5	6.14E+6	7.92E+5	6.95E+4
6			3.22E+5	5.89E+6		4.83E+4
7	2.26E+3	1.13E+4	1.70E+5	3.52E+6	3.95E+5	2.91E+4
8		7.80E+3	4.84E+4	1.01E+6		1.84E+4
9		2.47E+3	1.18E+4		3.36E+4	
10			3.28E+3			
11				3.37E+3		

^{90}Zr

	3	4	5	6	7
0					
1			1.08E+3	2.20E+2	
2		1.89E+3	1.43E+4	2.07E+3	
3	1.06E+3	1.17E+4	1.37E+5	1.47E+4	1.27E+3
4	2.93E+3	5.22E+4	1.06E+6	6.78E+4	4.06E+3
5	6.22E+3	8.61E+4	3.62E+6	1.60E+5	8.00E+3
6		7.34E+4	3.37E+6		7.59E+3
7	3.26E+3	3.11E+4	9.94E+5	6.86E+4	4.48E+3
8	8.23E+2	7.57E+3	1.48E+5		
9		1.69E+3		2.50E+3	
10					
11					

Fig. 4.11 - Typical counting rate for each working pad for the ^{208}Pb target (left panel) and for the ^{90}Zr (right panel) target.

This conclusion is also supported by the results of the optimization procedure we performed for the Doppler correction, described in §6.4. In fact, we obtained the best Doppler correction when moving the detectors some millimetre away from their supposed design position, resulting in the angular positions with respect to the beam axis shown in Tab. 4.1. This procedure did in fact show that the left telescope is some degree farther away from the beam direction compared to the right telescope.

	Design value	Left telescope	Right telescope
^{208}Pb	12°	16.2°	11.3°
^{90}Zr	8°	11.8°	9.0°

Tab. 4.1 - Angular position of the TRACE telescopes relative to the beam direction, as obtained with the optimization procedure for the Doppler correction (see §6.4). The angles are referred to the middle point of the first column of each ΔE detector.

4.5. GIANT QUADRUPOLE RESONANCE EXCITATION

The inelastic scattering of an ^{17}O beam at 20 MeV/u is expected to populate strongly the giant resonance region, in particular the ISGQR [60-62], of the target nuclei. This means that the energy spectra of the inelastically scattered ^{17}O ions are expected to show strong peaks above the separation energy. The excitation energy transferred to the target is measured by the Total Kinetic Energy Loss (TKEL) of the projectile, that is the difference between the Total Kinetic Energy (TKE) measured in an event and the energy corresponding to an elastic scattering event, since they are roughly equal in the our case.

Fig. 4.12 shows the excitation spectra in the Giant Resonance region for the ^{208}Pb data (left panel) and the ^{90}Zr data (right panel), with the full statistics, and selecting only the pads with the best energy resolution. The bump arising from the excitation of the giant resonance region is clearly visible and has been fitted with a simple Gaussian to show that the centroid energy is close to the known energy of the ISGQR. It has, however, a much larger width (see Tab. 4.2 for the known values): this is because the ISGQR is not the only giant resonance to be populated in the reaction,

and the peak in Fig. 4.12 is the result of the partial superposition of more than one resonance.

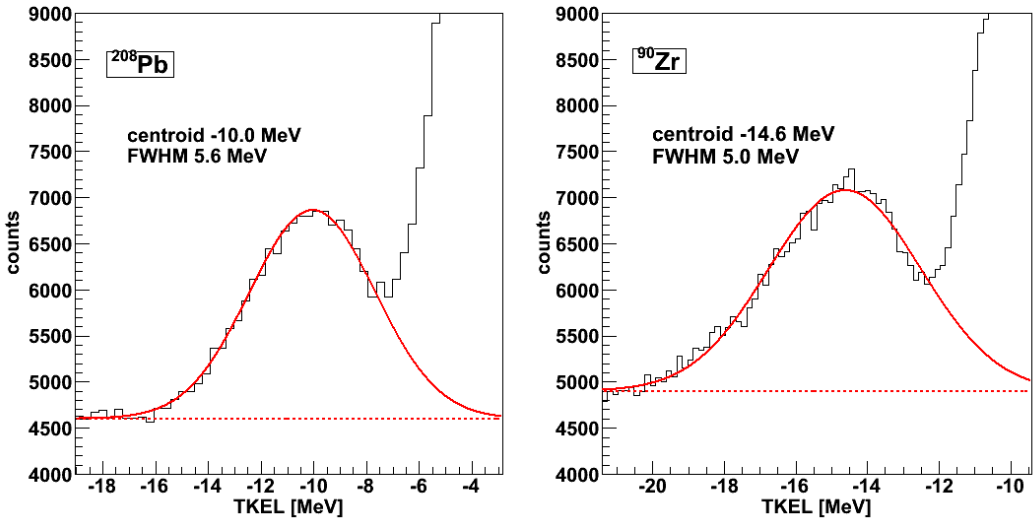

Fig. 4.12 - Energy spectra of the scattered ^{17}O ions measured with the ^{208}Pb target (left panel) and the ^{90}Zr target (right panel), for a selection of pads with the best energy resolution. The large peak is due to the population of various giant resonances, the dominant one being the ISGQR.

A tentative decomposition of the giant resonance peak is shown in Fig. 4.13; the centroid energy and FWHM of each resonance are fixed parameters (taken from [61], see also Tab. 4.2); the excitation of lower energy states has been reproduced with a large Gaussian peak. Note that this decomposition is only qualitative, and no cross-section information can be extracted from the fit because of the lack of a proper normalization. A subtraction of the continuum underlying the peaks has been performed following [62].

^{208}Pb	L	E [MeV]	FWHM [MeV]
ISGQR	2	10.9	2.6
ISGHR	4	12.0	2.4
ISGMR	0	13.7	3.6

^{90}Zr	L	E [MeV]	FWHM [MeV]
ISGQR	2	14.0	3.6
ISGMR	0	16.8	3.8

Tab. 4.2 - Multipolarity, centroid energy and FWHM of the IsoScalar Giant Monopole, Quadrupole and Hexapole Resonances, shown in Fig. 4.13; the values are taken from [61].

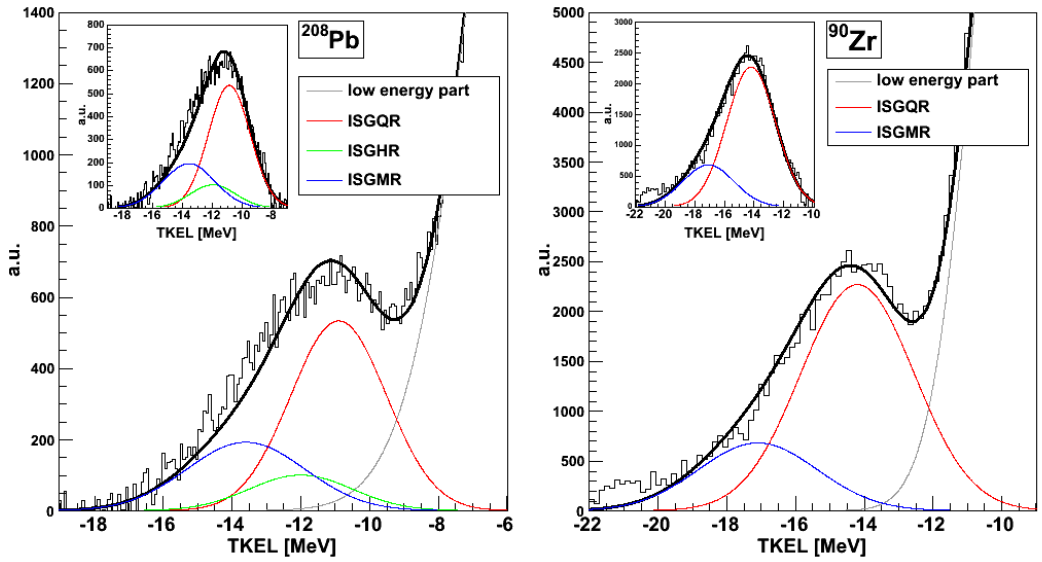

Fig. 4.13 - Energy spectra of the scattered ^{17}O ions measured with the ^{208}Pb target (left panel) and the ^{90}Zr target (right panel), for a selection of pads with the best energy resolution. A continuous background has been subtracted following ref. [62], and a fit showing the different components of the bump (taken from [61]) has been performed. The excitation of low-lying states has been taken into account with a gaussian tail (in grey); the insets show the fit results with the subtraction of the low energy component. All resonance widths were summed in squares with the experimental resolution.

Chapter 5. Analysis of the scintillator data

An array of 3 large volume $LaBr_3$:Ce detectors and 3 clusters of small BaF_2 detectors was used to measure the gamma-ray radiation emitted by the target in the inelastic scattering reaction channel. It will be shown in §5.1 how the gamma-rays emitted in coincidence with the scattered beam ions were selected with the timing information, and in §5.2 how the detectors were calibrated. It will be then shown in §5.3 how the gamma-ray energy was correlated to the energy loss measured in the Si telescopes and in §5.4 how this correlation was used to search for and identify a signature of the PDR decay.

5.1. TIME SPECTRA

During the experiment, a time signal was acquired for each $LaBr_3$:Ce and BaF_2 crystal using a CAEN V878 VME TDC. The timing information was obtained from the CFD output of the BaFpro module, sent through an active delay unit and then to the TDCs. As for the Si telescopes (see §4.2), the TDCs worked in "common start" mode and the Master Gate was opened, for gamma-ion coincidence events, by the pads of the E detectors (see also Fig. 3.12).

Fig. 5.1 shows the time spectrum for one $LaBr_3$:Ce detector in coincidence with the various trigger markers. The strongest peak in the red and green spectra corresponds to the coincidence of the $LaBr_3$:Ce detector with a Si detector; the width of the peak is 6 ns FWHM. The blue spectrum shows the peak corresponding to the random coincidences between the detector and a "TRACE singles" event, and has the same FHWM. The purple spectrum has two peaks: a narrow, self-coincidence spike corresponding to the events in which the detector opened the master gate in a "scintillator singles" event, and a larger peak corresponding to the coincidence of the detector with another scintillator; this peak has a FWHM of 3 ns because of the time walk of the detectors.

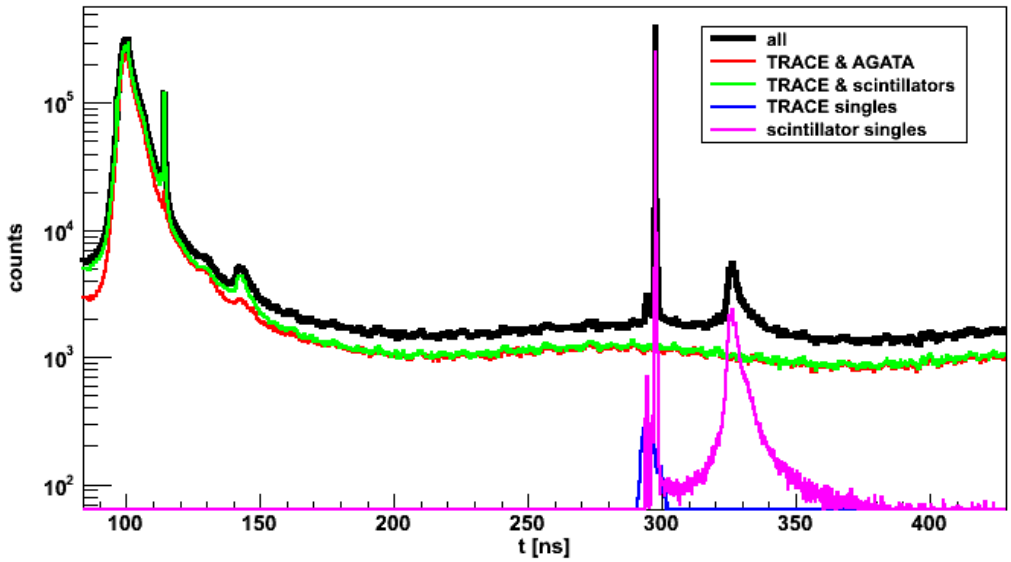

Fig. 5.1 - Typical time spectra for the 3"x3" $LaBr_3$:Ce detector. The black histogram corresponds to the spectrum without any gating condition, while the coloured spectra are in coincidence with the various trigger markers, as indicated in the legend (see also §3.6).

The width of the coincidence spectrum is affected by the large spread in energy of all the reaction products detected by the telescopes. Fig. 5.2 shows the time spectrum for the same $LaBr_3$:Ce detector with the gating condition that an ^{17}O ion is detected in the telescopes; the FWHM of the peak is now ~ 4 ns, and is due to both the timing

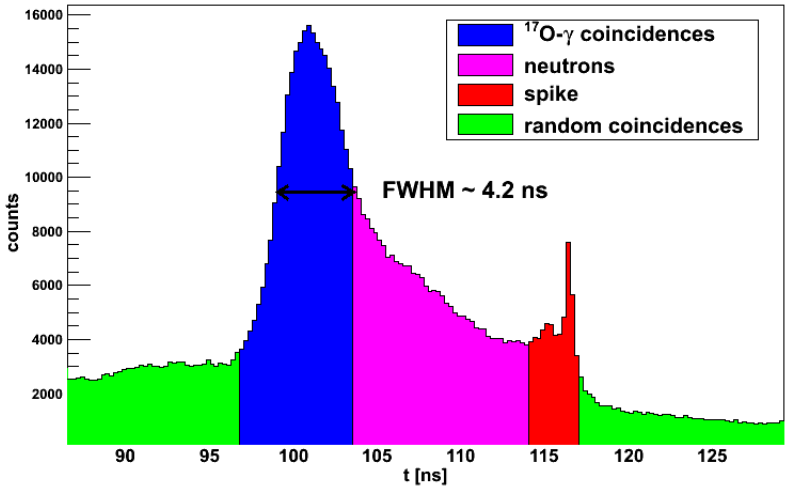

Fig. 5.2 - Time spectrum for the 3"x3" $LaBr_3$:Ce detector, gated on the ^{17}O scattering channel. The coincidence peak shows a tail due to neutrons, and a spike caused by spurious events.

resolution and to the time walk of the Si detectors (see also Fig. 5.9). For the following analysis, all $LaBr_3$:Ce spectra gated on the coincidence time are gated on the window in blue in Fig. 5.2, that is 7 ns large. The tail to the right of the coincidence is caused by neutrons.

In both Fig. 5.1 and Fig. 5.2 a narrow spike on top of the neutron tail is clearly visible; the spike is also present in the other 2 $LaBr_3$:Ce crystals (see Fig. 5.4). It has a FWHM of ~1 ns, meaning that the time reference for the start signal cannot be given by a TRACE telescope, since their time resolution is much worse. This peak is either due to a self-coincidence of the HECTORplus crystal with itself, or to a coincidence between the $LaBr_3$:Ce crystal and a BaF_2 crystal: that is, it corresponds to events in which the ion-gamma coincidence is not opened by the OR of the Si detectors, as shown in Fig. 3.12, but by the OR of the scintillators, as shown in Fig. 5.3.

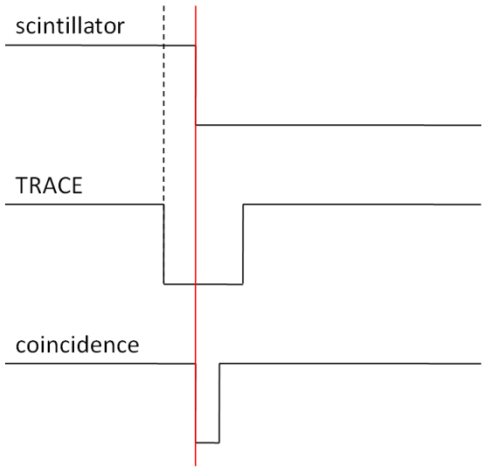

Fig. 5.3 - Schematic view of the possible class of events that causes the spike in the HECTORplus time spectra.

These events are a source of background and should be removed. Unfortunately, as can be seen in Fig. 5.4, left panel, for the 2 large volume HECTORplus detectors the spike lies exactly on top of the coincidence peak for the duration of the whole measurement with the ^{208}Pb target. This means that rejecting the gamma-rays that fall in the time window of the spike also means rejecting most of the coincidence gamma-rays. Before we started measuring with the ^{90}Zr target the scintillator timing

was adjusted in such a way that the spike is found on the tail of the peak, and as seen in Fig. 5.4, right panel.

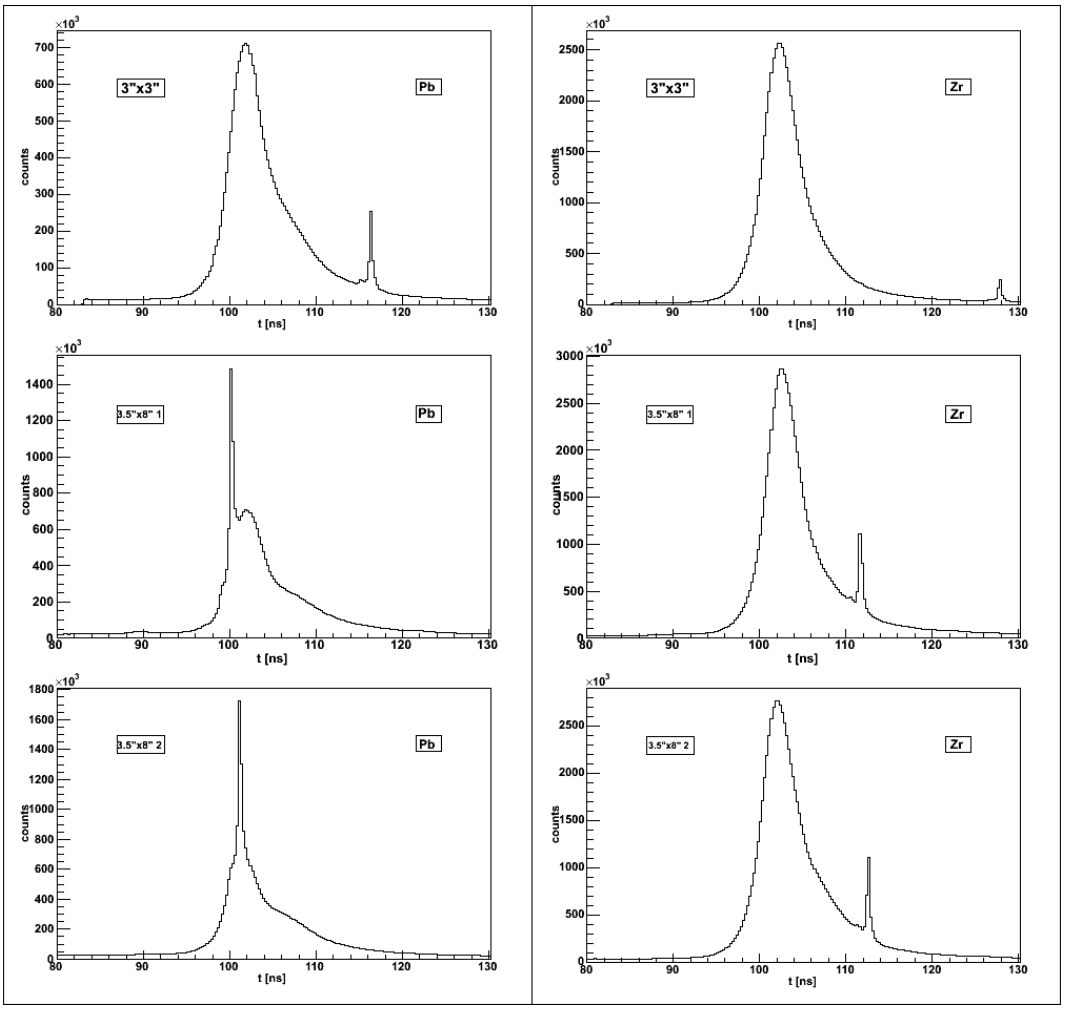

Fig. 5.4 - Time spectra for all 3 $LaBr_3$:Ce detectors during a typical run of the ^{208}Pb target (left column) and of the ^{90}Zr target (right column). Note how the position of the spike relative to the coincidence peak changes between the two datasets.

For the 3"x3" crystal it was possible to plot the two energy spectra obtained when the time information is in the coincidence time window or in the spike, shown in Fig. 5.5 in black and red respectively. It is clear that at high energy (above ~1 MeV) the gamma-rays in coincidence with the spike form a featureless continuum, while the first transitions of ^{208}Pb are visible in the gamma spectrum with the correct coincidence. We decided to ignore the presence of the spike in the subsequent

analysis, since it appears not to cause artefacts in the energy spectra, except for a higher background.

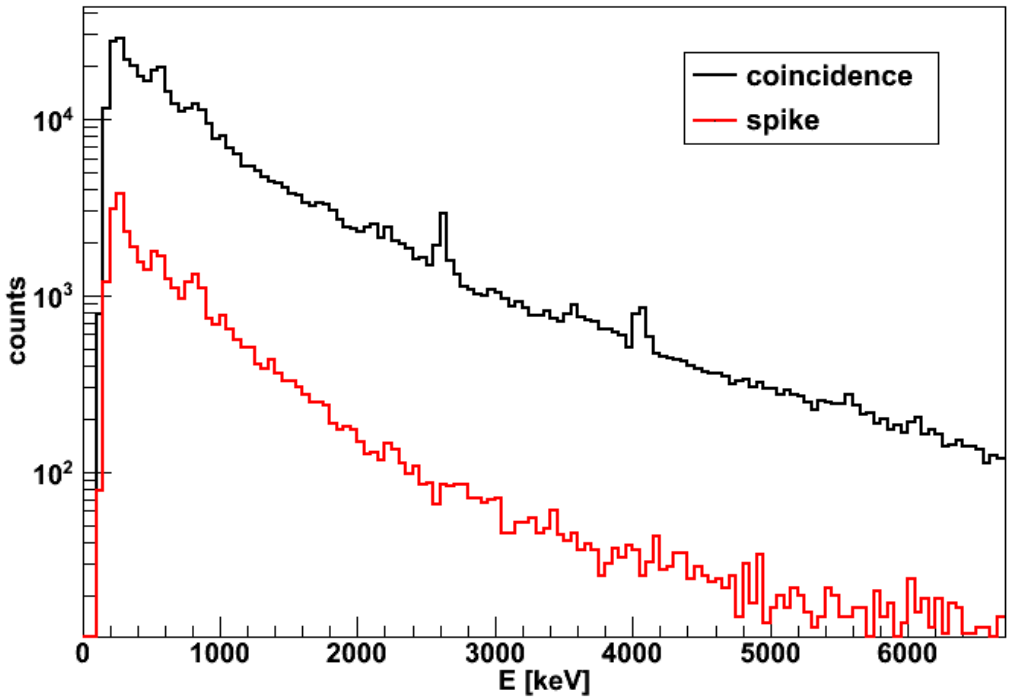

Fig. 5.5 - Energy spectra measured in the 3"x3" $LaBr_3$:Ce detector for the ^{208}Pb target under different timing conditions: the black spectrum is gated on the actual coincidence peak, marked in blue in Fig. 5.2, while the red spectrum is gated on the spike marked in red in Fig. 5.2. Both spectra are also gated on the ^{17}O scattering channel.

Fig. 5.6 shows the time spectrum obtained for one HELENA detector during the ^{208}Pb measurement, in coincidence with the various trigger markers. As for the $LaBr_3$:Ce detectors, the strongest peak in the red and green spectra corresponds to the coincidence of the BaF_2 detector with a TRACE telescope; the width of the peak is 6 ns FWHM. The blue spectrum shows the peak corresponding to the random coincidences between the detector and a "TRACE singles" event, and has the same width. The purple spectrum has only one peak, probably due to the coincidence between the BaF_2 crystal and one of the $LaBr_3$:Ce detectors; the peak has a FWHM of 300 ps.

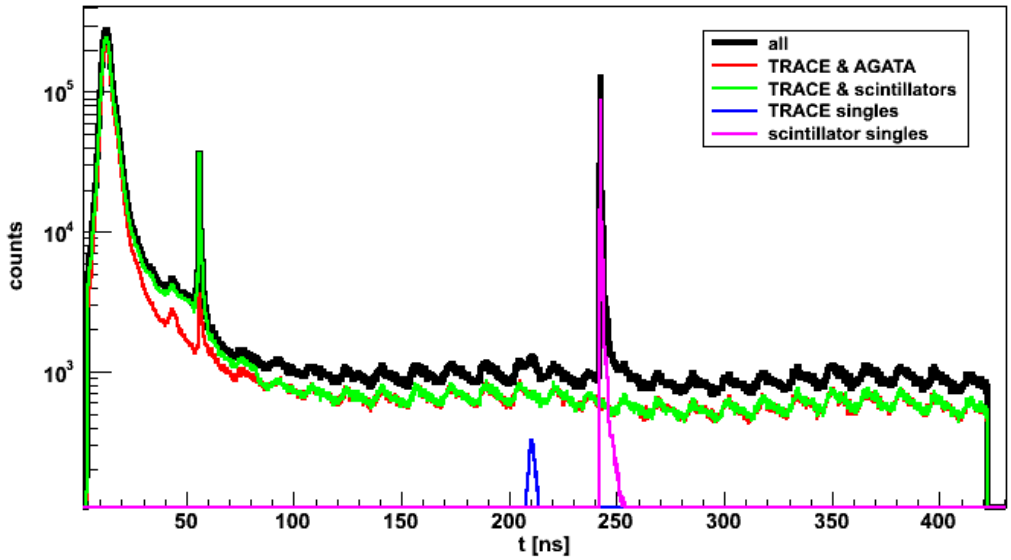

Fig. 5.6 - Time spectrum for one HELENA detector. The black line corresponds to the spectrum without any gating condition, while the coloured spectra are in coincidence with the various trigger markers, as indicated in the legend (see also §3.6).

During the ^{208}Pb measurement, however, the coincidence peak in the green and red spectra of Fig. 5.6 is visible only for two detectors. This can be seen in Fig. 5.7, which shows the time spectrum without gating conditions for all the HELENA crystals. The blue spectrum corresponds to the detector used for Fig. 5.6.

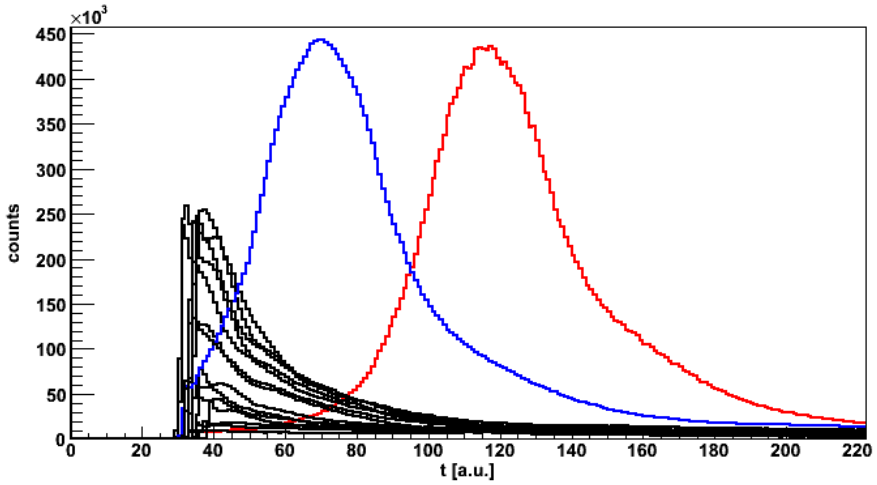

Fig. 5.7 - Raw time spectra for all Helena crystals during the measurement with the ^{208}Pb target. All coincidence peaks except for those of two crystals (in red and blue) are cut off from the spectrum because the stop signal of the TDC was not delayed enough.

This happened because the time signals for the HELENA detectors were not delayed enough, and in the case of a coincidence event the "stop" signal arrived at the TDC before the "start" signal. The problem was corrected for the ^{90}Zr measurement by adding one more delay module to the timing chain of the HELENA detectors, in order to bring the "stop" signals inside the window of the TDCs. This was possible only for the detectors that were grouped in the two 8-crystal clusters; the 4 crystals of the remaining cluster were therefore discarded.

We show in Fig. 5.8 the time spectrum for a HELENA crystal measured with the ^{90}Zr target, with the gating condition that an ^{17}O ion is detected in the telescopes, obtaining a coincidence peak of ~4 ns of FWHM, due to both the timing resolution and to the time walk of the Si detectors (see also Fig. 5.9). Note that since the $LaBr_3$:Ce detectors were placed at forward angles, had a larger contribution from neutron events compared to the BaF_2 detectors (see Fig. 5.2).

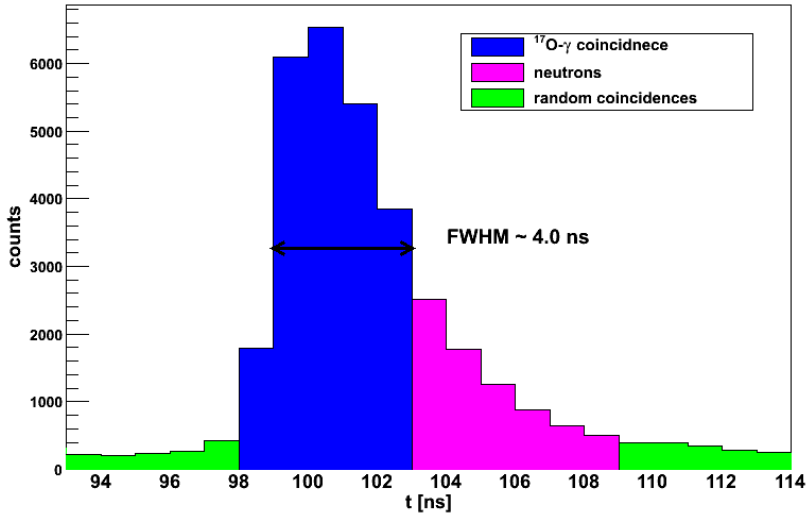

Fig. 5.8 - Time spectrum for one BaF_2 detector, gated on the ^{17}O scattering channel. The coincidence peak shows a tail due to neutrons.

The effect of the time walk of the Si telescopes can be seen in Fig. 5.9, showing the time spectrum measured in the 3"x3" $LaBr_3$:Ce detector (left panel) and in one BaF_2 detector (right panel) with the same gating conditions as in Fig. 5.2 and Fig. 5.8 and the additional requirement all the "start" signals come from the same pad, with a sizeable decrease of the FWHM.

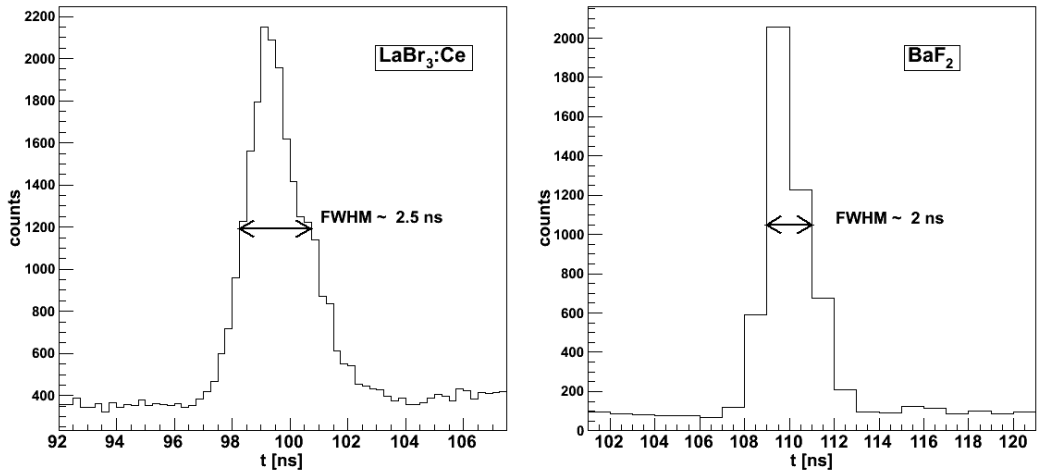

Fig. 5.9 - Time spectrum of the 3"x3" $LaBr_3$:Ce detector (left panel) and of one BaF_2 detector (right panel) gated on the ^{17}O scattering channel and with the requirement that all the "start" signals come from the same Si pad.

5.2. DETECTOR CALIBRATION

All the scintillators were calibrated in energy with standard radioactive sources such as ^{60}Co, ^{137}Cs, and ^{88}Y. Fig. 5.10 shows a calibration spectrum for a $LaBr_3$:Ce detector (left panel) and for a BaF_2 detector (right panel). The energy resolution at the 662 keV line of ^{137}Cs was 27 keV for the $LaBr_3$:Ce and 79 keV for the BaF_2.

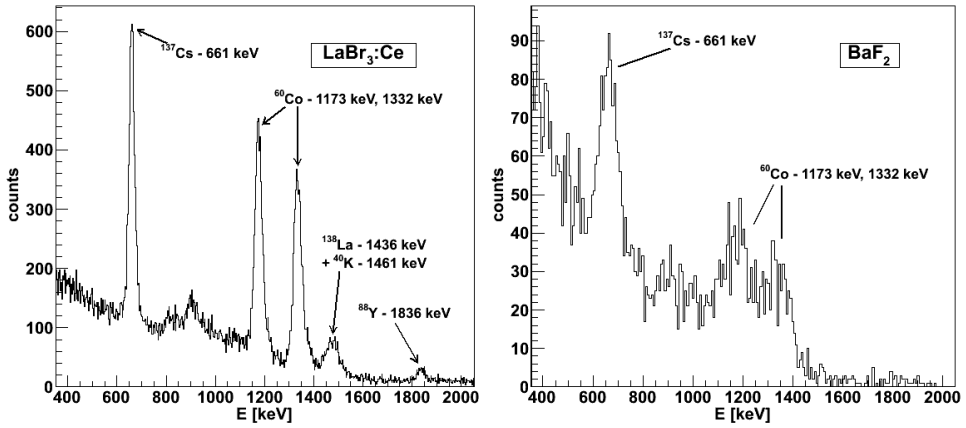

Fig. 5.10 - Calibration spectra for a $LaBr_3$:Ce detector (left panel) and a BaF_2 detector (right panel). The ^{88}Y source was significantly less active than the others, meaning that the 898 keV line of ^{88}Y was not used for the calibration of $LaBr_3$:Ce detectors, and neither lines of ^{88}Y were used for the BaF_2 detectors.

A recalibration for each $LaBr_3$:Ce crystal was necessary for the spectra taken during the measurement, probably due to the higher counting rate. This was performed by taking the energy spectra gated on the ^{17}O scattering channel and performing a fit on the decay from the first 3^- state of ^{208}Pb at 2615 keV for one dataset and from the first 2^+ state of ^{90}Zr at 2168 keV for the other.

Fig. 5.11 shows the energy spectra obtained for all 3 detectors with the ^{208}Pb (left panel) and ^{90}Zr (right panel) taregets. It can be seen, however, that the energy resolution of the 2 large volume $LaBr_3$:Ce detectors was far worse than that of the 3"x3" one, even though they have comparable energy resolutions in the calibration spectra (see Tab. 5.1).

	^{137}Cs	^{208}Pb	^{90}Zr
3"x3"	3.6%	3.7%	4.1%
3.5"x8" 1	4.1%	6.8%	7.9%
3.5"x8" 2	3.6%	6.8%	7.7%

Tab. 5.1 - Energy resolution of the 3 $LaBr_3$:Ce detectors at the energy of 662 keV, measured with a ^{137}Cs source and during the experiment. The resolution for the data with the ^{208}Pb target was measured at the 2615 keV line of the ground state decay from the first 3^- state, and the value at 662 keV was obtained with the relation $FWHM \propto \sqrt{E}$; the same was done for the ^{90}Zr data and the resolution measured at the 2186 keV line of the ground state decay from the first 2^+ state.

A possible explanation for the degradation in energy resolution is that it is caused by the very high counting rate the detectors suffered during the measurement (up to 70 kHz), which was higher in the 3.5"x8" crystals both because of the larger volume and because they were closer to the beam dump.

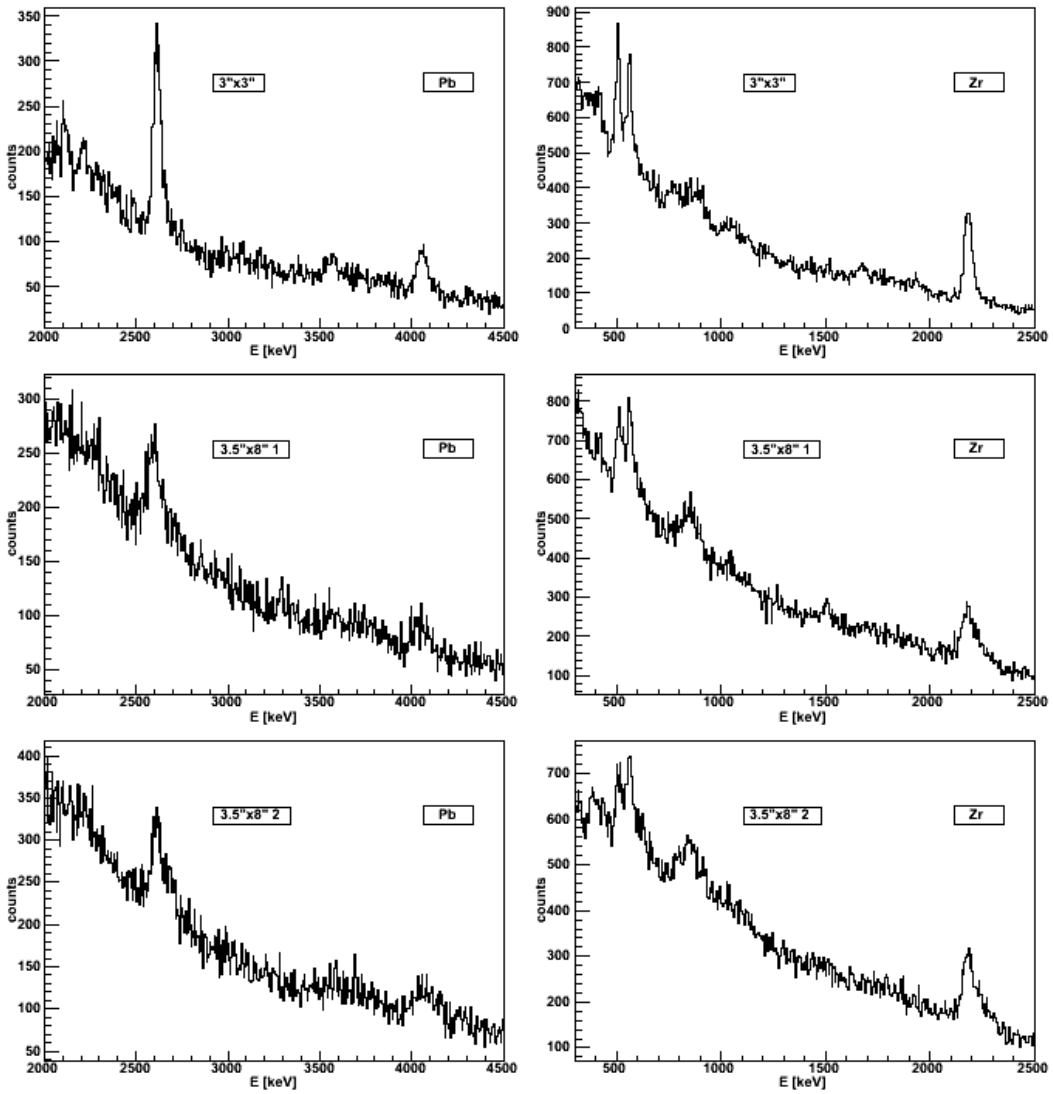

Fig. 5.11 - Energy spectra measured in the 3 HECTORplus detectors with the ^{208}Pb target (left column) and the ^{90}Zr target (right column); the spectra are gated on the ^{17}O scattering channel and on time.

A preliminary operation to be performed before studying the energy spectra of the HELENA detectors is the selection of the gamma-rays in the matrix that shows the fast component of the signal against the slow component. This matrix is shown in Fig. 5.12, left panel, for one BaF_2 crystal during the ^{208}Pb measurement, with gating conditions on the ^{17}O scattering and on the timing. All the events that fall outside of the area enclosed in the black line are either alpha particles caused by the internal

activity of the BaF_2 (in the low part of the matrix) or pileup events (in the top part of the matrix). There is a class of events that do not have a fast component, probably because the threshold was set too high. As shown in the right panel of Fig. 5.12, these events constitute mostly the low-energy part of the energy spectrum, while the events inside the gate are dominant for energies above ~1.5 MeV. Since we are interested in the gamma decay from high-energy states, we will always apply the gate on the "fast vs slow" matrix keeping the events with E_{fast}=0.

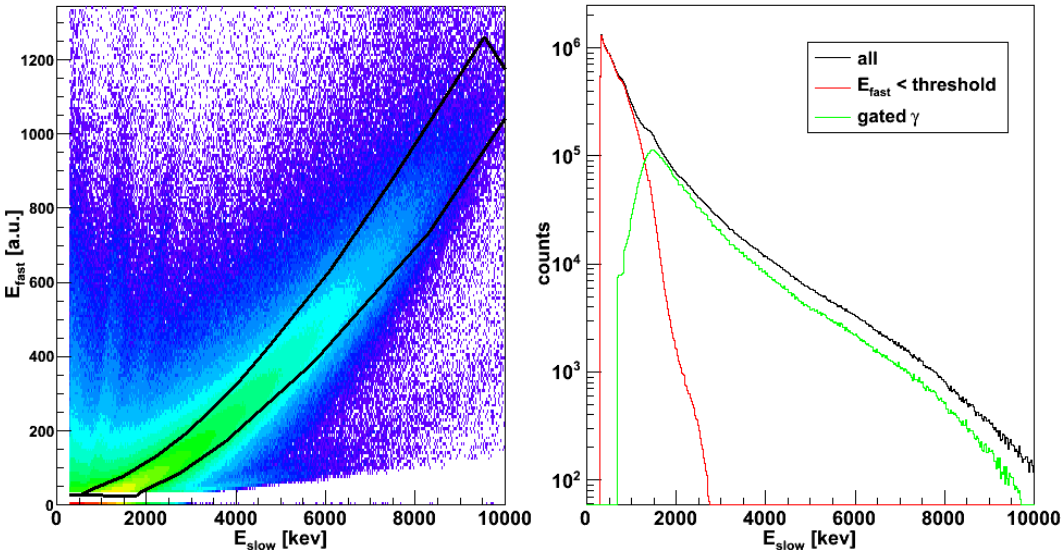

Fig. 5.12 - Left panel: scatter plot showing the fast component of the signal of a BaF_2 detector against the slow component; the black line marks the gamma-ray part of the matrix. Right panel: in black, the energy spectrum for the same BaF_2 detector; the red spectrum corresponds to the events in which the fast component was 0 (below the threshold); the green spectrum corresponds to the part of the matrix inside of the gate.

Fig. 5.13, left panel, shows the energy spectrum measured with the ^{208}Pb target by one of the BaF_2 crystals with a good timing (see Fig. 5.7), gated on the coincidence time peak and on the fast vs slow matrix, as well as on ^{17}O scattering channel. The right panel shows the spectrum measured by the same crystal under the same conditions with the ^{90}Zr target. Both spectra show how the HELENA detectors can barely resolve the first excited state of the target nucleus from the background.

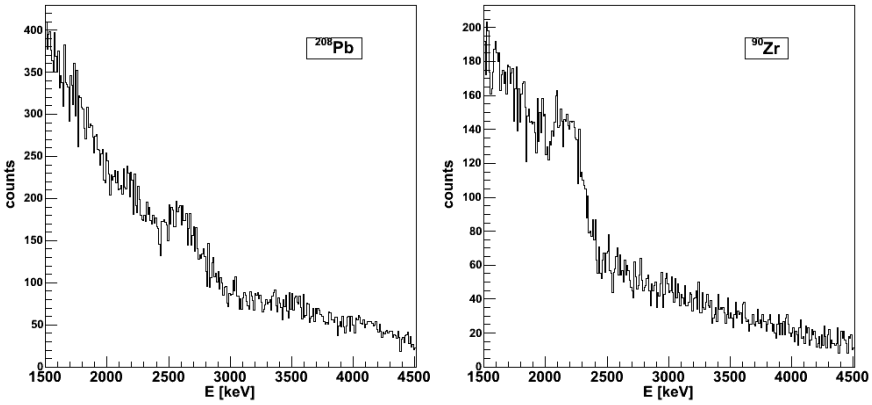

Fig. 5.13 - Energy spectra measured in one BaF_2 detector with the ^{208}Pb target (left panel) and the ^{90}Zr target (right panel). Both spectra are gated on the ^{17}O scattering channel.

For the ^{90}Zr measurement, we could also build the energy spectra for the two clusters with a good timing (see §5.1), by summing the energy of each crystal for each cluster. The cluster energy spectrum (in red) is compared to the one obtained by taking all the individual crystals (in black) in Fig. 5.14, and shows as expected an increase of counts in the high energy region. Note that the statistics collected in the energy region of the ISGQR (12 MeV) is rather small, even without further gating conditions.

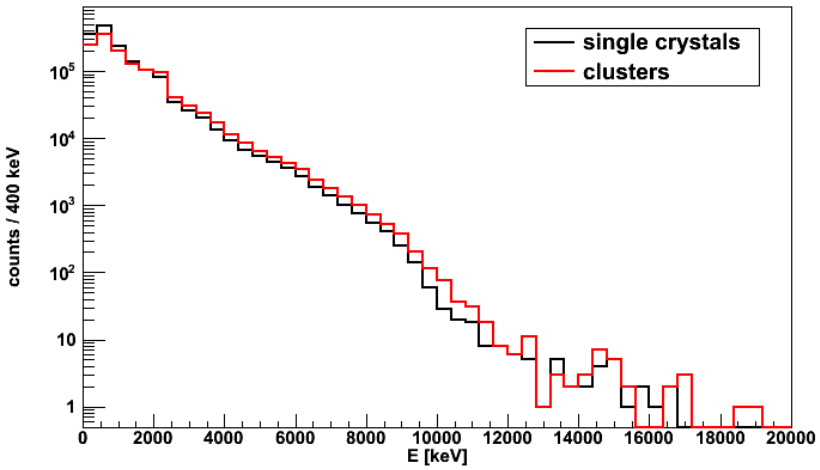

Fig. 5.14 - Energy spectrum of the gamma-rays measured with the BaF_2 detectors in coincidence with the ^{17}O scattering with the ^{90}Zr target. The red spectrum is obtained by considering the two 8-crystal clusters as two individual detectors and summing the energies of all crystals belonging to each; the black spectrum is obtained by considering the array as made of 16 independent BaF_2 detectors.

5.3. CORRELATION WITH THE SI TELESCOPES

There are two reasons for using the Si telescopes in the analysis of the experiment: for the selection of the reaction channel, as described in §4.4, and for the correlation of the gamma-ray energy with the excitation energy transferred to the target nuclei. In the case of the experiment described in this thesis, the latter quantity can be measured with the Total Kinetic Energy Loss (TKEL) of the projectile, that is the difference between the Total Kinetic Energy (TKE) measured in an event and the energy corresponding to an elastic scattering event.

In particular, we decided to request that the gamma-ray energy be equal, within the energy resolution of the TRACE detectors, to the TKEL: this condition allows to select the direct decay to the ground-state. This is done by plotting the gamma-ray energy against the TKEL for the event and by applying a diagonal cut on the matrix, as seen in Fig. 5.15 for the 3"x3" detector. Note how this excludes both the gamma decay from higher lying states (seen in the bottom right part of the matrix) and the gamma-rays corresponding to a random coincidence with an elastic scattering event (the vertical structure in the top part of the matrix).

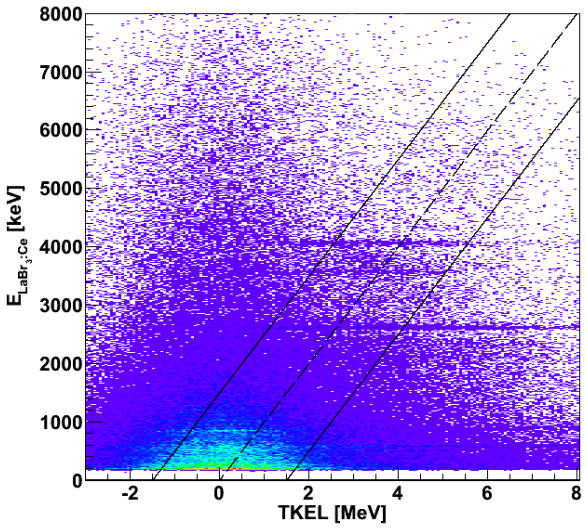

Fig. 5.15 - Scatter plot showing the TKEL versus the gamma-ray energy measured by the 3"x3" $LaBr_3$:Ce detector with the ^{208}Pb target. The diagonal lines mark the region that was selected for the study of the ground-state decay, that is ±1.5 MeV large.

Fig. 5.16 shows in green the energy spectrum of the gamma-rays detected in coincidence with a scattered ^{17}O ion, while the red spectrum is obtained without any gating condition. Since both spectra are normalized to the total number of counts, it is clear how the selection of the ^{17}O scattering channel enhances greatly the intensity of ^{208}Pb transitions, in particular for the decay of the first 3^- state at 2614.5 keV and for the first 2^+ state at 4185.5 keV. Fig. 5.16 also shows, in blue, the energy spectrum of the gamma-rays whose energy is equal to the TKEL, again normalized to the total number of counts. It is evident how the transitions corresponding to the ground-state decay of the first 3^- and 2^+ states are further enhanced compared to the green spectrum. See also §6.5 for more comments on this kind of correlation.

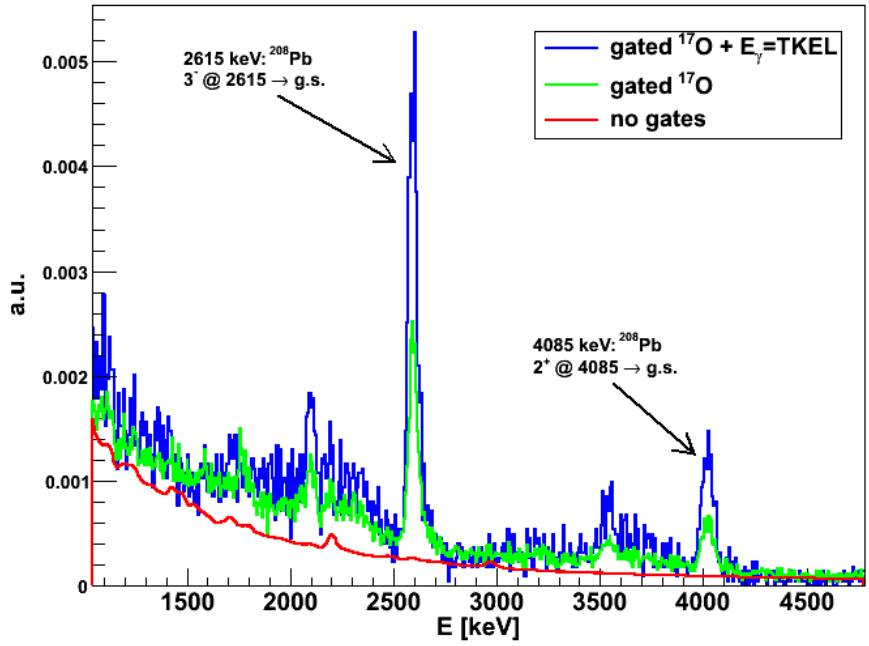

Fig. 5.16 - Energy spectra measured for the ^{208}Pb target with the 3"x3" $LaBr_3$:Ce detector, under different gating conditions: the red spectrum is without any gate, the green spectrum is gated on the ^{17}O scattering channel and on the coincidence peak of the time spectrum, and the blue spectrum has the additional requirement that the energy be equal to the TKEL within a ±1.5 MeV large gate. All spectra are normalized to the total number of counts.

In order to see if it possible to measure the direct decay from the ISGQR to the ground state, we also show in Fig. 5.17 the energy spectra measured over the range 0-15 MeV, with a binning of 400 keV/ch, both with the ^{208}Pb target (left panel) and the ^{90}Zr target (right panel). We performed both the diagonal cut described above,

and a simple "vertical" cut by requesting that the measured TKEL is in the range between 5 and 25 MeV. However, the statistics drops above 7-8 MeV, and is very small at the energy of the ground-state decay of the ISGQR, both for ^{208}Pb and ^{90}Zr.

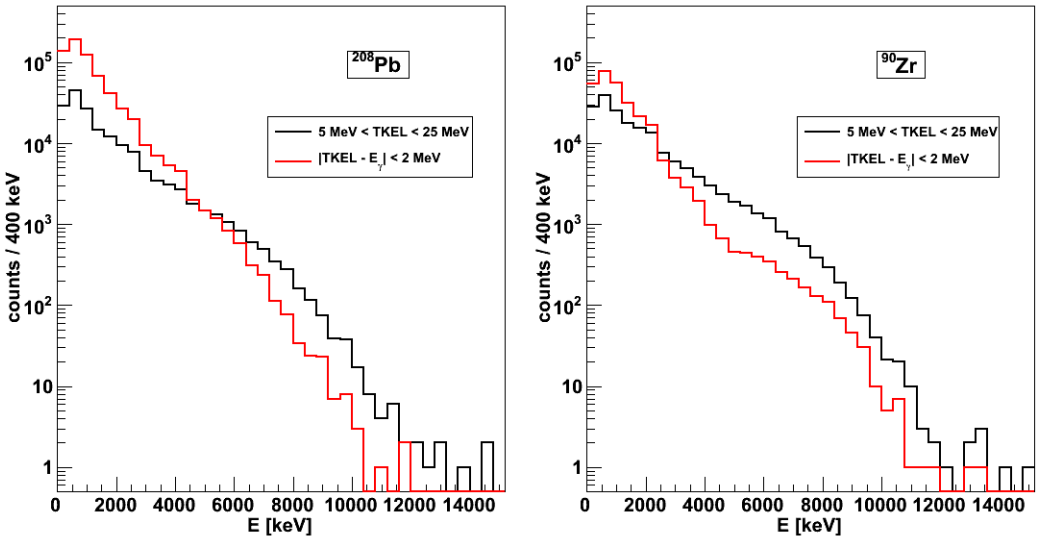

Fig. 5.17 - Energy spectra measured with the 3 LaBr$_3$:Ce detectors in the 0-15 MeV energy range, binned to 400 keV/ch, for the ^{208}Pb target (left panel) and for the ^{90}Zr target (right panel). The black spectra are gated on the requirement that the TKEL be in the 5-25 MeV interval, the red spectra are gated on the requirement that the TKEL be equal to the gamma-ray energy within ±2 MeV. In either case, the statistics at the energy of the ground state decay of the ISGQR is negligible.

The same procedure was applied to the BaF_2 clusters for the data measured with the ^{90}Zr target, obtaining the matrix shown in Fig. 5.18, analogous to that obtained for $LaBr_3$:Ce detectors (Fig. 5.15).

Fig. 5.19 shows in red the energy spectrum measured with the BaF_2 clusters for the ^{90}Zr target without any gating condition, compared to the one obtained by gating on the ^{17}O scattering channel (in green) and on the diagonal of the matrix in Fig. 5.18 (in blue); as for Fig. 5.16, all spectra are normalized to the total number of counts and show a marked increase of the intensity of ground state transitions over the background as we put more stringent gating conditions.

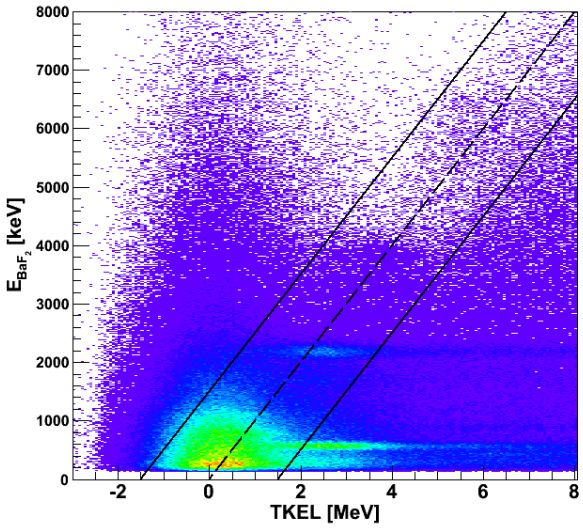

Fig. 5.18 - Scatter plot showing TKEL versus the gamma-ray energy measured by the BaF_2 clusters with the ^{90}Zr target. The diagonal lines mark the region that was selected for the study of the ground-state decay, that is ±1.5 MeV large.

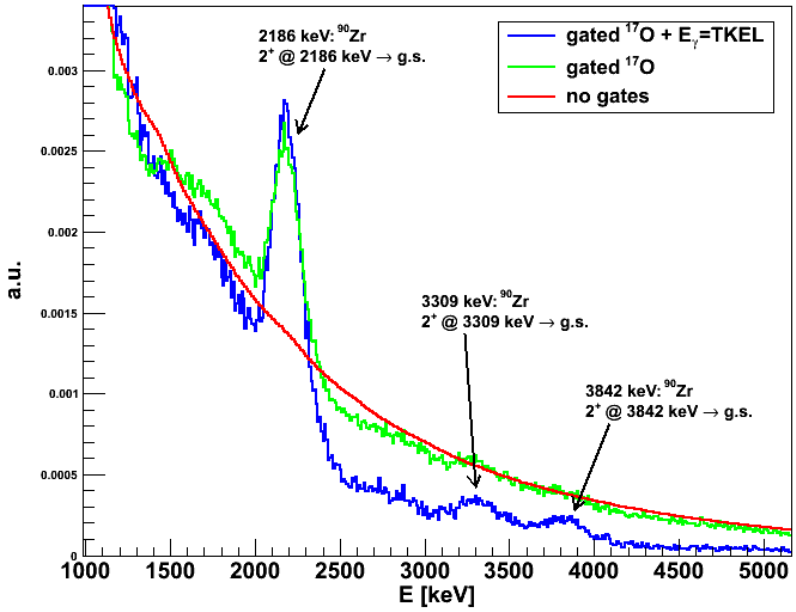

Fig. 5.19 - Energy spectra measured for the ^{90}Zr target with the BaF_2 clusters, under different gating conditions: the red spectrum is without any gate, the green spectrum is gated on the ^{17}O scattering channel and on the coincidence peak of the time spectrum, and the blue spectrum has the additional requirement that the energy be equal to the TKEL within ±1.5 MeV. All spectra are normalized to the total number of counts.

5.4. GAMMA DECAY FROM THE PDR

As mentioned in §1.6, the PDR is a collective vibration of electric dipolar (1^-) nature, meaning that its dominant decay channel is to the 0^+ ground state. While the $LaBr_3$:Ce detectors do not have the energy resolution necessary to separate the various states in which the resonance is fragmented, it is possible to use them to get an integrated measurement of the PDR strength.

In order to measure the gamma decay from the PDR we therefore had to select the ^{17}O inelastic scattering channel and the coincidence peak in the time spectrum, as well as to request that the gamma-ray energy be equal to the TKEL within detector resolution, as explained in §5.3.

Fig. 5.20 shows the energy spectrum obtained with the ^{208}Pb target in the energy region of the PDR (up to ~8 MeV for ^{208}Pb). The top panel shows only the spectrum for gamma-rays measured in the 3"x3" detector. Some structures are visible, qualitatively similar to the ones seen with the AGATA Demonstrator (see Fig. 6.23), but at energies that do not match the known values for the strongest transitions; this is probably due to the nonlinearity of the detector. The bottom panel shows the spectrum with the sum of all the HECTORplus detectors, where due to the worse resolution of the large crystals the structures are less visible over the background.

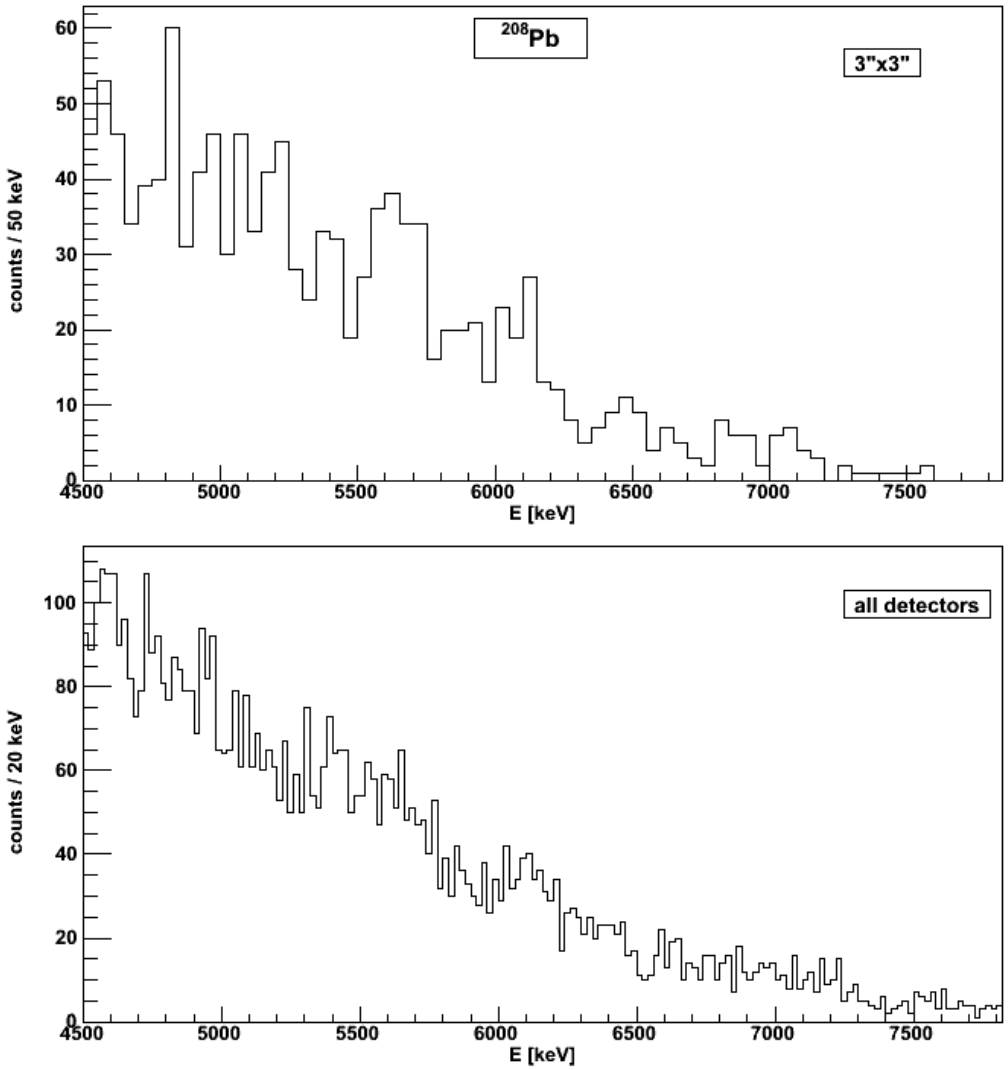

Fig. 5.20 - Gamma decay from the PDR of ^{208}Pb measured with the 3"x3" LaBr$_3$:Ce detector (top panel) and all HECTORplus detectors (bottom panel); all spectra are gated with the conditions described in text.

The same can be said for the spectra measured with the ^{90}Zr target, as seen in Fig. 5.21.

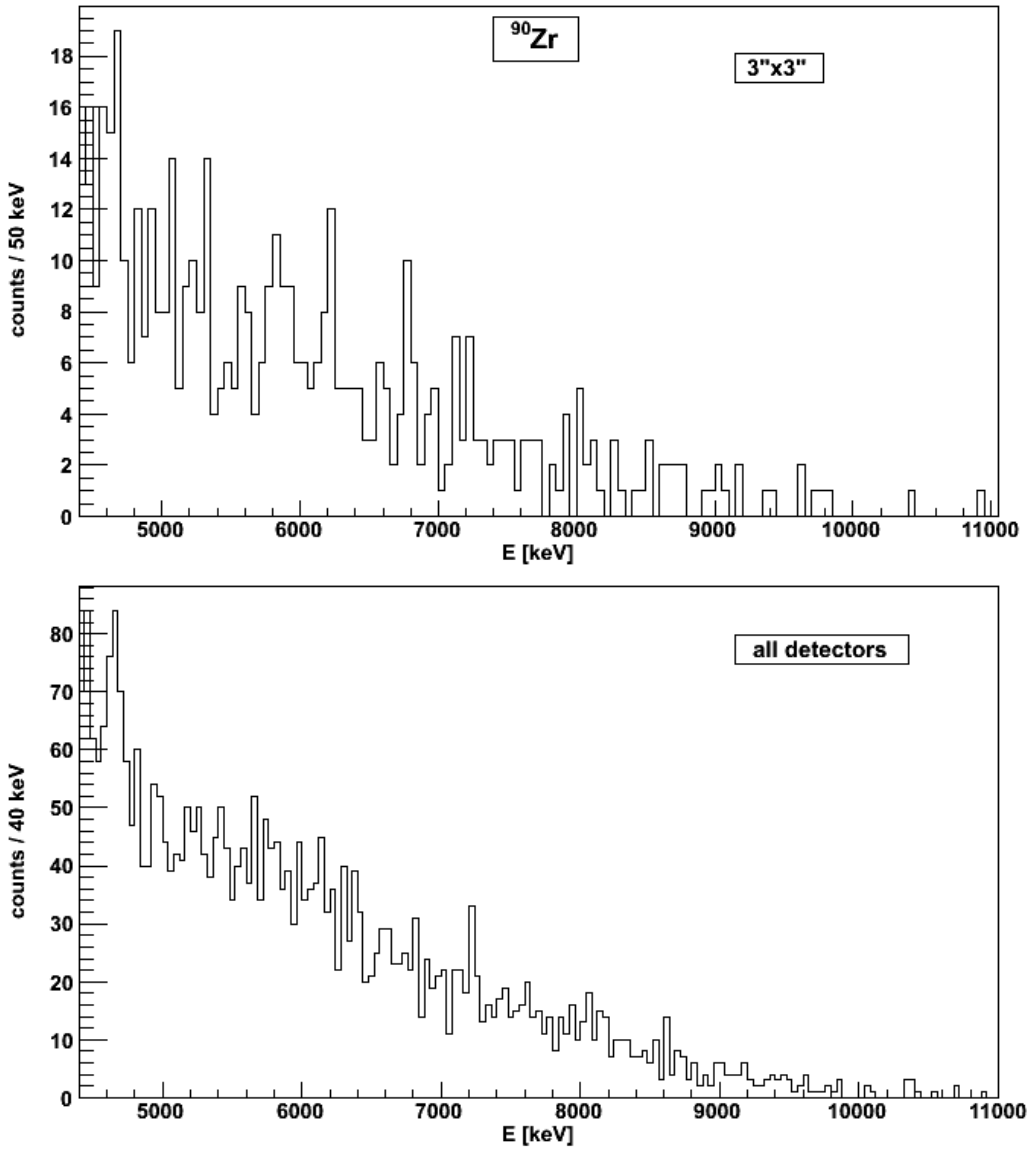

Fig. 5.21 - Gamma decay from the PDR of ^{90}Zr measured with the 3"x3" $LaBr_3$:Ce detector (top panel) and all HECTORplus detectors (bottom panel); all spectra are gated with the conditions described in text.

To improve the quality of these spectra, we are presently investigating better corrections for the nonlinearity and the possibility of performing an unfolding procedure (see §6.6).

Better results with the ^{90}Zr target were obtained with the BaF_2 clusters: Fig. 5.22 shows the energy spectrum measured in coincidence with the ^{17}O scattering and gated on the diagonal of Fig. 5.18; some structures around ~6.5 MeV are visible, in good agreement with what is observed with AGATA (see Fig. 6.23 and Fig. 6.33).

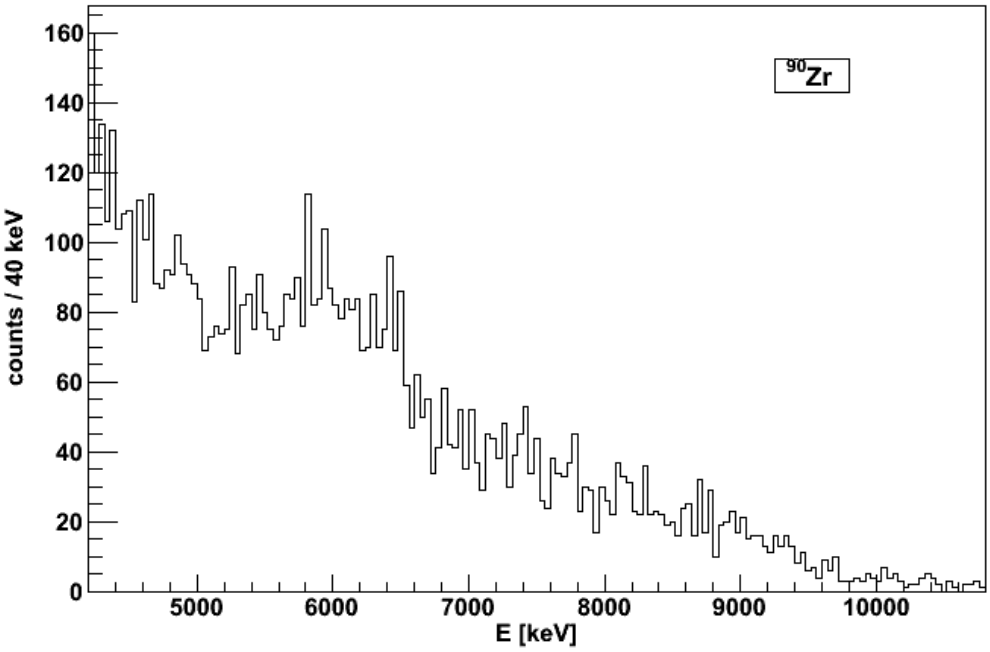

Fig. 5.22 - Gamma decay from the PDR of ^{90}Zr measured with the BaF_2 clusters; the spectrum is gated with the conditions described in text.

Chapter 6. Analysis of the AGATA Data

The AGATA Demonstrator was used to measure the gamma-ray radiation emitted in coincidence with the inelastic scattering of the ^{17}O beam. A preliminary step of the analysis was the so-called replay of the experiment, in which the PSA and tracking algorithms were performed starting from the pulse samples written to disk; this procedure is described in §6.1. It will be then shown in §6.2 how the timing information is obtained for the AGATA detectors. In §6.3 we will describe the calibration of the detectors, and in §6.4 the correction of the measured energies for the Doppler effect. It will be then shown in §6.5 how the gamma-ray energy was correlated to the energy loss measured in the Si telescopes, and in §6.6 how the gamma spectra were further cleaned from background by performing a removal of the Compton-scattered gamma-rays. Then it will be shown in §6.7 how all this was used to obtain a measure of the PDR decay, and in §6.8 how we looked into the possibility of measuring the angular distributions of the pygmy transitions. Finally, in §6.9, it will be presented how we obtained from the experimental data a measure of the B(E1) strength for the PDR states we observed.

6.1. Replay of the AGATA Data

As described in §3.1, the spectroscopic performance of the AGATA array is based on the principles of pulse-shape analysis (PSA) and gamma-ray tracking. During the experiment, these operations are performed in real time by the NARVAL Data AcQuisition (DAQ) system (see also §3.5), but they also can be performed again after the experiment with a C++ emulator of NARVAL.

This is possible because the DAQ writes to disk a list-mode file for each detector, containing the digitized pulse signals from the segments and the timestamp information for each event; the emulator can process all the files, performing again the PSA and matching the data from different crystals, as well as matching the AGATA and ancillary data. This procedure is called a "replay" , because from the point of view of the data processing it is essentially a repetition of the experiment.

In the case of our experiment, a replay was necessary in order to apply a better calibration to the segments, since the calibration used online was very rough due to time constraints. We could also make use of improvements in the PSA that were not available at the time of the experiment, such as the correction for neutron damage (see [66] and references therein).

The replay was performed in two steps: in the first one, the PSA was performed for all AGATA detectors, and "reduced" data with energy, position, and time information for all the segments were saved to disk. In the second step, the data from all the segments were merged and the tracking was performed.

The advantage of this separation in two steps is that the PSA is a very slow process, taking up a large amount of computing power and memory: it took about 1 week to perform the first step with 6 computers working in parallel. The tracking, instead, is a much faster task and could be repeated several times as we changed parameters, without having to perform the PSA again.

After the PSA and tracking processes are completed, the user is given a list-mode file in ROOT tree format (see [97], [98] for more information on ROOT). For each event, the file contains the list of reconstructed gammas, together with their energy, timestamp information and the position of the first interaction, as well as the data of the ancillary detectors received from the VME crate. A sorting code was developed for the analysis of the list-mode data; it is the code used to make all the experimental spectra shown in this thesis. See Appendix C for more details.

6.2. TIME SPECTRA

Each gamma-ray reconstructed by the tracking algorithm is associated to a timestamp, which measures the absolute time from the start of the GTS clock in steps of 10 ns. A more precise information is given by the PSA, that uses a linear interpolation algorithm to determine the start time of the signal. The sum of these two values gives the detection time of the gamma relative to the start time of the GTS.

The spectra in Fig. 6.1, left panel, were obtained by choosing one AGATA detector as a reference and measuring the time difference between that detector and all the

others. A time walk of the order of 10 ns between the crystals is observed; this was corrected by adding an offset to the timing information of each crystal, obtaining the spectra shown in the right panel of Fig. 6.1.

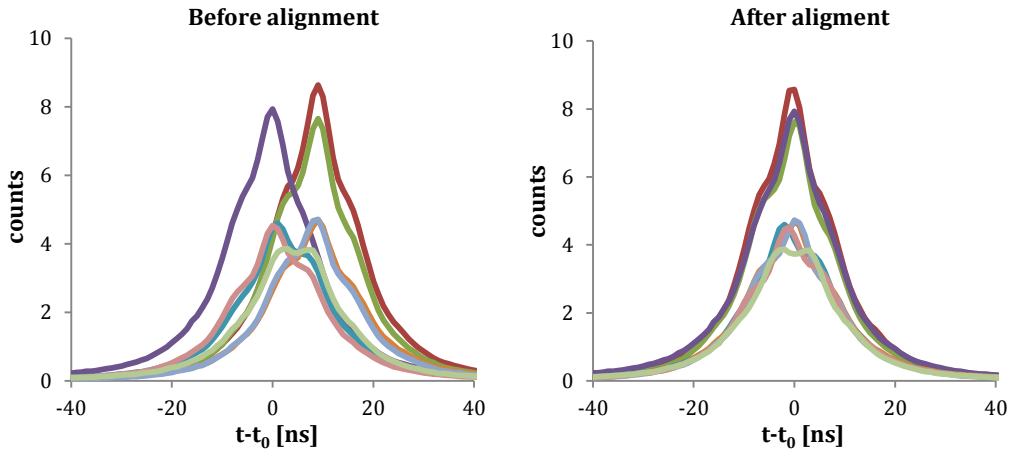

Fig. 6.1 - Time spectra of all AGATA crystals against a reference one, before (left panel) and after (right panel) the correction for the time walk of the crystals. The spectra are without gating conditions.

To obtain useful physical information, however, the detection time of the gamma-ray must be correlated to the detection time of the ^{17}O ions. The latter timing information is given by the GTS timestamp of the ancillary branch of the acquisition, again with a step of 10 ns; a better precision is obtained by adding to the timestamp the so-called "phase shift", which is acquired by one channel of the TDCs and measures when the VME master gate was opened relative to the GTS clock.

The AGATA time relative to the trigger time was therefore built as:

$$t_{gamma} = T_{AGATA} + t_{linear\ interpolation} - T_{AGAVA} - t_{phase\ shift} \quad (6.1)$$

where T_{AGATA} and T_{AGAVA} are the timestamps for the gamma and for the ancillary branch of the DAQ.

Fig. 6.2 shows in black the time spectrum thus obtained, as well as the time spectra obtained in coincidence with the different trigger markers as described in the legend (see §3.6). The strongest peak in the red and green spectra corresponds to the coincidence of the AGATA detector with a TRACE telescope, and the peak in the blue spectrum corresponds to the random coincidence of AGATA with a scaled-down "TRACE singles" trigger. The width of both peaks is ~24 ns and is dominated by the

time resolution of the AGATA detectors. The purple spectrum shows the peak corresponding to the random coincidence of AGATA and the scaled-down "scintillator singles" trigger; it is interesting to note that a peak in the same position is present also in the black spectrum, meaning that there are coincidences between scintillators and AGATA not accounted for by the scaled-down trigger. This class of events probably corresponds to the "spike" seen in the HECTORplus time spectra (see §5.1) and would be a source of background, but it is easily removed by placing a gate on the coincidence peak.

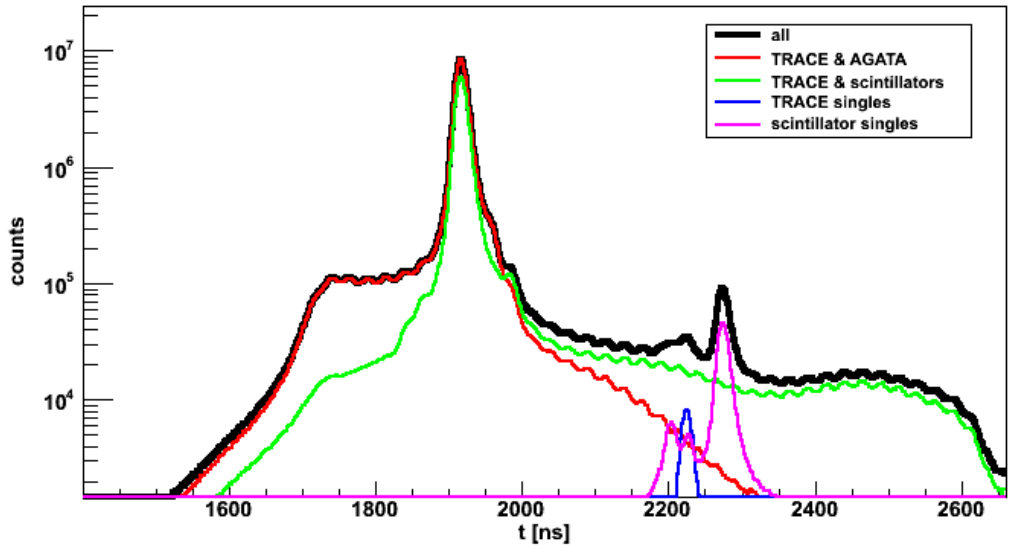

Fig. 6.2 - Time spectrum for the AGATA detectors. The black line corresponds to the spectrum without any gating condition, while the coloured spectra are in coincidence with the various trigger markers, as indicated in the legend (see also §3.6).

As seen in §4.4, many different reaction products are detected in the Si telescopes, with a large spread in energy and time-of-flight; this spread also affects the width of the coincidence peak. For this reason, the gate on the coincidence time must be set after performing a selection of the ^{17}O scattering events. We show in Fig. 6.3 the time spectrum for the AGATA detectors under the gating condition that an ^{17}O ion is detected in the TRACE telescopes. The peak has a FWHM of ~ 20 ns, and the area marked in blue corresponds to the gate on time that will be applied to the AGATA spectra in the following analysis.

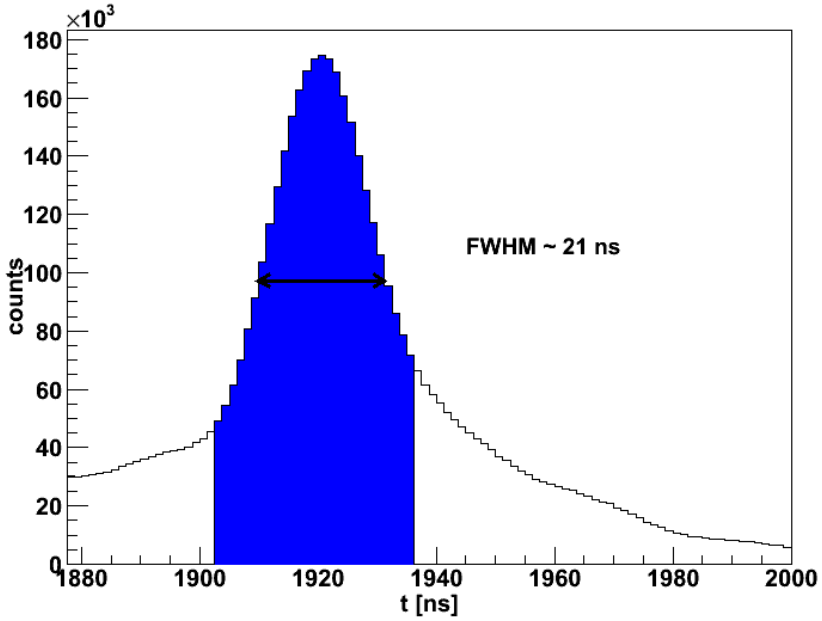

Fig. 6.3 - Time spectrum for the AGATA detectors when an ^{17}O ion has been detected in the TRACE telescopes. The area in blue marks the coincidence between AGATA and the Si telescopes, and corresponds to the time window used as gating condition in all the subsequent spectra taken in coincidence with the ^{17}O scattering.

6.3. ENERGY CALIBRATION

The energy calibration of the AGATA detectors is performed together with the PSA. The calibration coefficients for each segment of the 9 detectors, as well as for the core signals, were calculated using data from two ^{60}Co calibration runs, one performed at the beginning and one performed at the end of the experiment, since during the measurement the flat-top constant of the digital shaping algorithm was changed to allow for higher counting rates.

Since the performance of the detector at high energies is important for our measurement, we also used a composite source of AmBe-Ni for calibration. In such a source, a core of ^{9}Be and alpha-unstable ^{241}Am is surrounded by a thick layer of paraffin; some metal discs of nickel are also placed inside the paraffin layer. When an alpha particle is emitted by the ^{241}Am, there's a high probability that it is captured by a ^{9}Be, making a $^{9}Be(\alpha,n)^{12}C$ reaction. The neutrons are emitted with energies going from ~400 keV to ~5 MeV, and are termalized by the multiple scattering in the

paraffin layer, which serves both as moderator and as shielding. The slow neutrons are then captured by the nickel isotopes, as well as by the chlorine isotopes present in the PVC that was used as an additional shielding; the neutron capture by the ^{1}H nuclei of the shielding produces additional gamma-rays in the spectrum. Note that the $^{9}Be(\alpha,n)^{12}C$ reaction can also populate the ^{12}C in its first excited state, at 4.4 MeV; the gamma decay from the level is Doppler broadened because the ^{12}C has a v/c of ~10%.

The AmBe-Ni source is very useful because the $^{58}Ni(n, \gamma)$ neutron capture reaction produces gamma-rays up to ~9 MeV of energy, and this is one of the few ways to have such high energy gammas without using an accelerator. The energy spectrum acquired with the AGATA Demonstrator for the AmBe-Ni source is shown in Fig. 6.4, while Tab. 6.1 shows the principal energy lines in the spectrum and the associated reactions.

Energy [keV]	Reaction
1460.822	^{40}K β decay
1712.245	$^{1}H(n,\gamma)^{2}H$
1951.142	$^{35}Cl(n,\gamma)^{36}Cl$
1959.348	$^{35}Cl(n,\gamma)^{36}Cl$
2223.245	$^{1}H(n,\gamma)^{2}H$
2614.522	$^{207}Pb(n,\gamma)^{208}Pb$
2863.823	$^{35}Cl(n,\gamma)^{36}Cl$
3061.869	$^{35}Cl(n,\gamma)^{36}Cl$
4438.91	$^{9}Be(\alpha,n)^{12}C$
4944.316	$^{35}Cl(n,\gamma)^{36}Cl$
5517.223	$^{35}Cl(n,\gamma)^{36}Cl$
5715.253	$^{35}Cl(n,\gamma)^{36}Cl$
6110.853	$^{35}Cl(n,\gamma)^{36}Cl$
6768.343	$^{35}Cl(n,\gamma)^{36}Cl$
6977.847	$^{35}Cl(n,\gamma)^{36}Cl$
7413.979	$^{35}Cl(n,\gamma)^{36}Cl$
7790.343	$^{35}Cl(n,\gamma)^{36}Cl$
8533.36	$^{58}Ni(n,\gamma)^{59}Ni$
8575.588	$^{35}Cl(n,\gamma)^{36}Cl$
8998.41	$^{58}Ni(n,\gamma)^{59}Ni$

Tab. 6.1 - Energies of the most intense gamma-rays produced by the AmBe-Ni source.

The front-end electronics for the AGATA detectors has 2 settings, one for low dynamic range (up to 4 MeV) and one for high dynamic range (up to 20 MeV); we used the latter during the experiment. It is known, however, that the segments show a non-linearity at high energies with this setting. While this effect is not large enough to compromise the performance of tracking algorithms, it can deteriorate the energy resolution of the reconstructed gamma-rays.

This effect can be seen clearly with the AmBe-Ni source: the inset of Fig. 6.4 shows, in red, the 8998 keV line reconstructed by the tracking: its shape is not gaussian and

it has a FWHM of ~20 keV, compared to the ~6 keV we would expect for HPGe detectors at that energy.

Since this nonlinearity affects only the segments, and not the core signals of the detectors, it's possible to correct the effect by adding the constraint in the tracking algorithm that for every event, the sum of the segment energies in a crystal is recalibrated to be equal to the energy measured in the core. This procedure was used to make the black spectrum in Fig. 6.4, which shows a FWHM of 7 keV at 9889 keV.

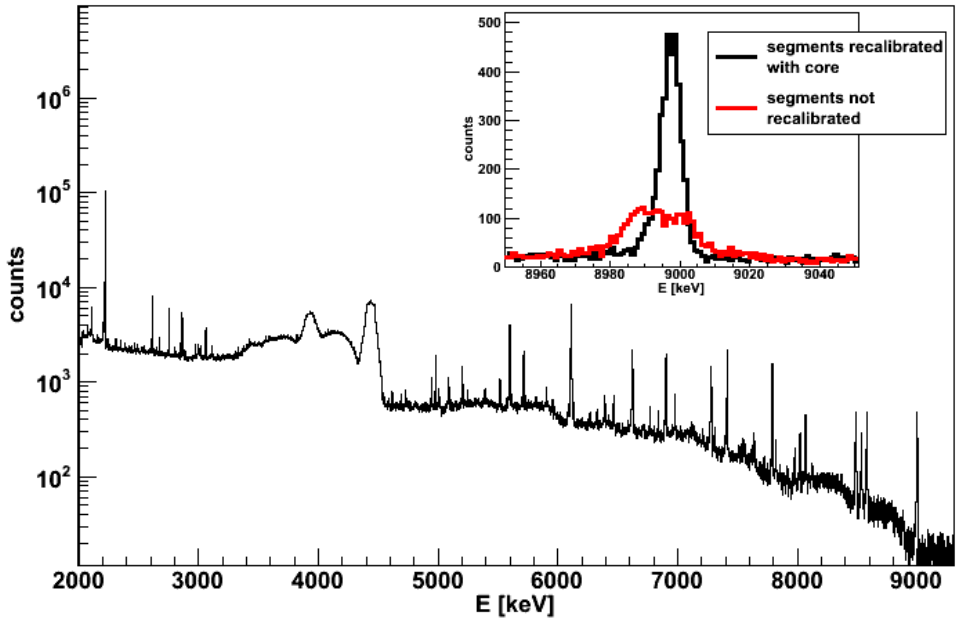

Fig. 6.4 - Energy spectrum of a composite AmBe-Ni source measured with the AGATA Demonstrator. The broad structure around 4 MeV is the Doppler-broadened decay of the first excited state of ^{12}C. The spectrum has been obtained with the recalibration of segment energies with the energy measured by the core, for each crystal. The inset shows an enlargement of the spectrum around the energy of the highest gamma-ray line at 9889 keV; the red spectrum is without recalibration.

The AmBe-Ni source was also used to verify the linearity of the response of the detector over the 5 - 9 MeV energy range: Fig. 6.5 shows the difference between measured and known value for various transitions above 5 MeV of energy (see Tab. 6.1); such difference is always within 1 keV (much smaller than the FWHM at 9 MeV), showing a very good linearity.

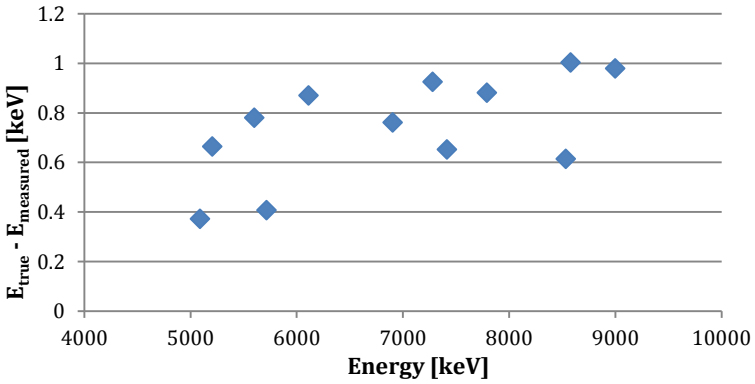

Fig. 6.5 - Linearity of the response of the AGATA Demostrator for gamma-rays in the energy range of 5 - 9 MeV.

The segment recalibration procedure was applied to the whole dataset. We then checked if the gain of the HPGe detectors was stable over time, by choosing a reference line and comparing its measured energy with the known value, for each crystal and on a run by run basis. We then calculated the ratio of the known energy of the peak over the measured value, as shown in Fig. 6.6. The coefficients show a gain variation over time within 3 ‰, and were used to recalibrate all the detectors on a run by run basis to correct for these fluctuations.

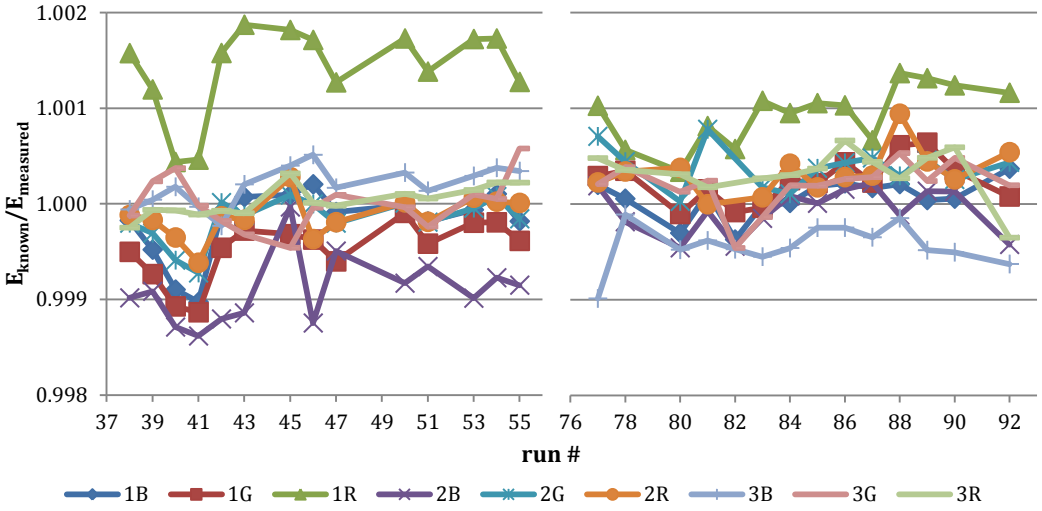

Fig. 6.6 - Ratio of the known energy for a reference line over the value measured for each crystal and for each run of the ^{208}Pb (left) and ^{90}Zr (right) measurements, showing gain fluctuations within 3 ‰. For the ^{208}Pb runs the reference line was the 2615 keV line of ^{208}Pb, for the ^{90}Zr runs the reference line was the 2212 keV line of ^{27}Al.

6.4. DOPPLER CORRECTION

One of the main challenges for the next generation of gamma spectrometers will be the detection of gamma-rays emitted in-flight by radioactive beams, in conditions of high background and relativistic projectile velocity (up to ~80% of the speed of light). For this reason, it is interesting to study the gamma decay from the projectile-like ejectiles produced in our experiment, as they have a $\beta = v/c$ of the order of 20%, that is the highest value of β for which the AGATA Demonstrator has been used up to now.

As seen in §4.4, we have many reaction channels available beside the ^{17}O inelastic scattering. Among those, we chose to focus first on ^{16}O, because it has a very strong gamma-ray line at 6129 keV, at an energy much higher than the 871 keV of the first excited state of ^{17}O: the ^{16}O line has therefore a larger Doppler shift and gives a better sensitivity to the Doppler correction; furthermore, the background from the target is much smaller.

The Doppler correction was applied using the well known formula:

$$E_{corr} = E_{lab}\frac{1-\beta\cos\theta}{\sqrt{1-\beta^2}} \qquad (6.2)$$

where E_{lab} is the energy measured in the laboratory frame of reference, E_{corr} is the energy in the projectile frame of reference, and θ is the angle between the projectile velocity vector and the gamma-ray velocity vector.

Assuming that the decay occurs at the target position, the direction of the gamma-ray velocity vector is determined by the position of the first point of interaction with the Demonstrator. Tracking algorithms are able to determine, for each reconstructed gamma-ray, the first interaction point and its coordinates, which are given as part of the output in the ROOT tree. The coordinates for the interaction points are given in the AGATA frame of reference (see Fig. 6.7).

The direction of the projectile velocity vector is similarly determined by the position of the pad in which the ion was detected. In order to account for uncertainties in the positioning of the detectors, we performed an optimization procedure for the position of the telescopes. Starting from the design position, we moved them

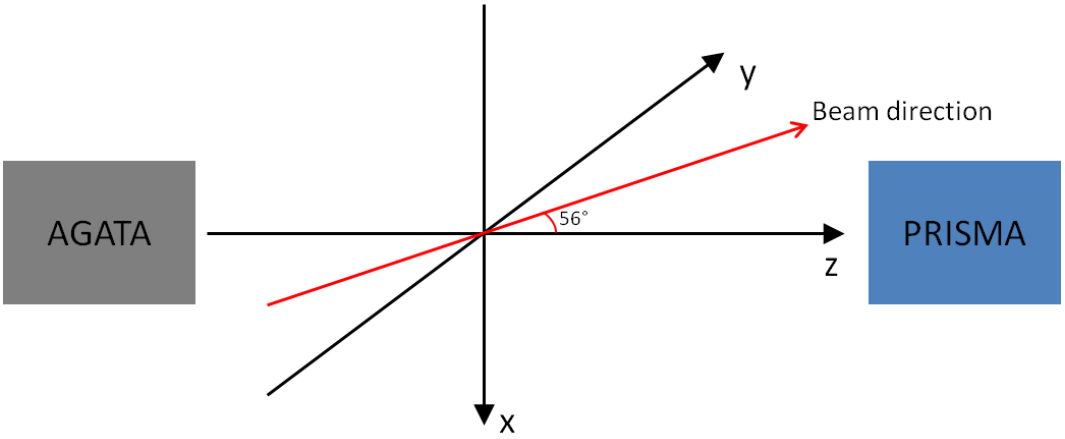

Fig. 6.7 - Frame of reference of the AGATA detectors.

horizontally in a 1 cm x 1 cm large grid with a step of 1 mm, evaluating for each point a figure of merit taking into account the FWHM and the correct energy of the ^{16}O line. The procedure was applied both for the data measured with the ^{208}Pb target and with the ^{90}Zr target, since they had different geometries. For the rest of the analysis, we used the optimal positions found in this way as the reference positions for the TRACE telescopes.

Fig. 6.8 shows, in red, the spectrum obtained for ^{16}O gamma decay. The Doppler correction was performed with the optimal position of the TRACE telescopes and the full information of PSA and tracking; we used a fixed value of $\beta = 0.203$ calculated from the reaction kinematics. For comparison, we also performed the Doppler correction using only the positions of the centres of the segments (in blue), losing the PSA information, and only the centres of the crystals (in black), as we would have with a conventional HPGe array. The grey spectrum instead is without Doppler correction, and one can see how the 6.1 MeV peak is Doppler-shifted into a broad structure.

The figure shows clearly that there is a marked improvement in the energy resolution of the Doppler-corrected spectrum thanks to the high position resolution of the AGATA detectors. The Doppler broadening was further reduced by calculating the speed of the projectile from the measured kinetic energy on an event-by-event basis: Fig. 6.9 shows in green the spectrum obtained in this way, compared to the one obtained with a fixed average value of β in red.

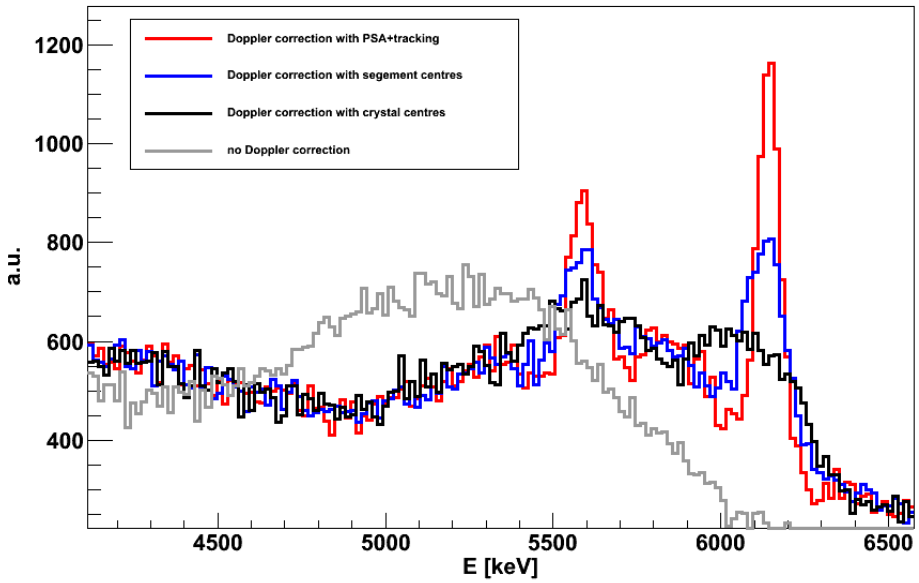

Fig. 6.8 - Energy spectrum of the gamma-rays measured in coincidence with the ^{16}O reaction channel. The grey spectrum is without Doppler correction, while the others were corrected using different position information as described in the legend.

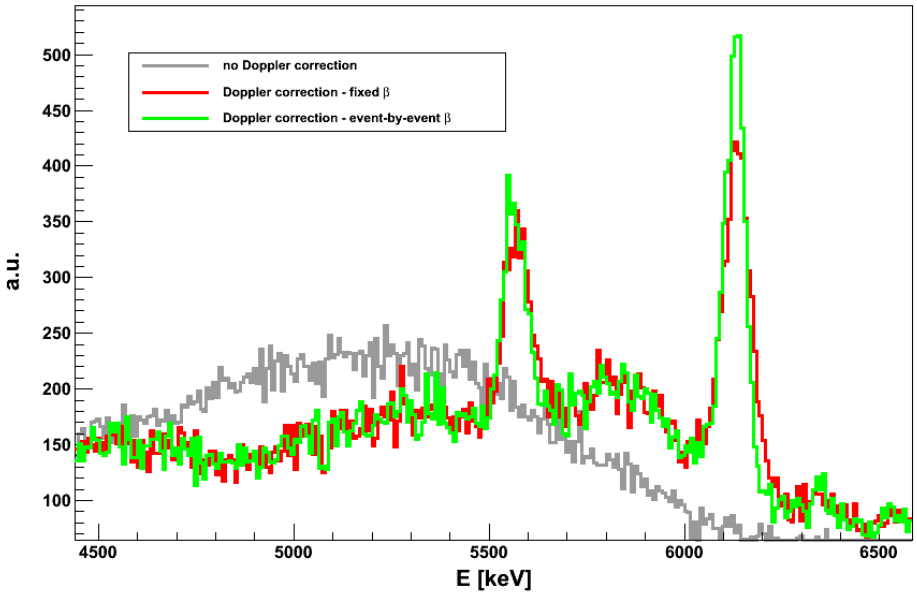

Fig. 6.9 - Energy spectrum of the gamma-rays measured in coincidence with the ^{16}O reaction channel. The grey spectrum is without Doppler correction, while the others were Doppler corrected, the red one with a fixed value of v/c, the other with a value that was calculated on an event-by-event basis from the TKE of the ion.

The energy resolution obtained in this way is 58 keV FWHM. This is the best result we could achieve, and is limited by the relatively bad angular resolution of the TRACE detectors: each pad is 4 mm large and the ΔE detectors are at a distance of ~7 cm from target, so that each pad covers an angle of about 3°.

Having fixed the position of the TRACE telescopes, we were also able to perform the Doppler correction for a number of other reaction channels, as shown in Fig. 6.10 for the 4.4 MeV transition of ^{12}C and the first excited levels of ^{17}N. It should be remarked that the experimental conditions would make it impossible to measure these transitions with traditional HPGe detectors.

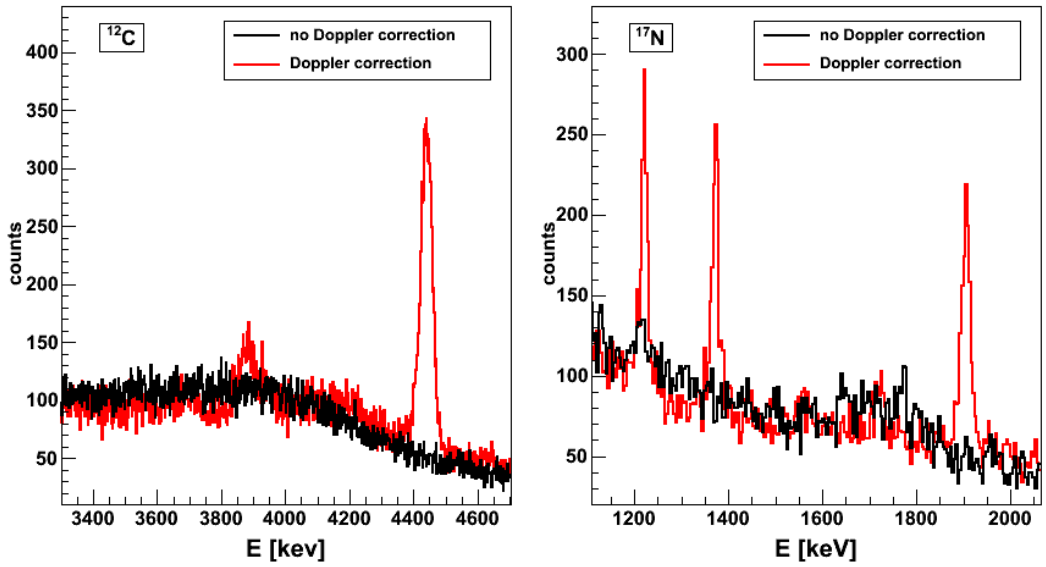

Fig. 6.10 - Energy spectra of the gamma-rays measured in coincidence with the ^{12}C (left panel) and ^{17}N (right panel) reaction channels. The red spectra are Doppler corrected, the black spectra are without correction.

Special care had to be taken for the case of ^{17}O: the first excited state of that nucleus is at 871 keV, quite close to the background line of ^{27}Al at 844 keV. The left panel of Fig. 6.11 shows the spectra with and without Doppler correction at energies close to those of said transitions, measured in coincidence with the left TRACE telescope. Both the ^{27}Al and the ^{17}O lines are clearly visible, the latter with a larger FWHM because of the Doppler broadening. We are sure that the line in the Doppler corrected spectrum is not just the Doppler-shifted ^{27}Al line because, given the position of the detectors and the beam velocity, it would be at an energy of 893 keV.

This is more visible in Fig. 6.11, right panel, where the spectra are taken in coincidence with the right TRACE telescope: due to a higher background, the ^{27}Al line is much stronger, and a bump centred at the energy of ~930 keV is visible.

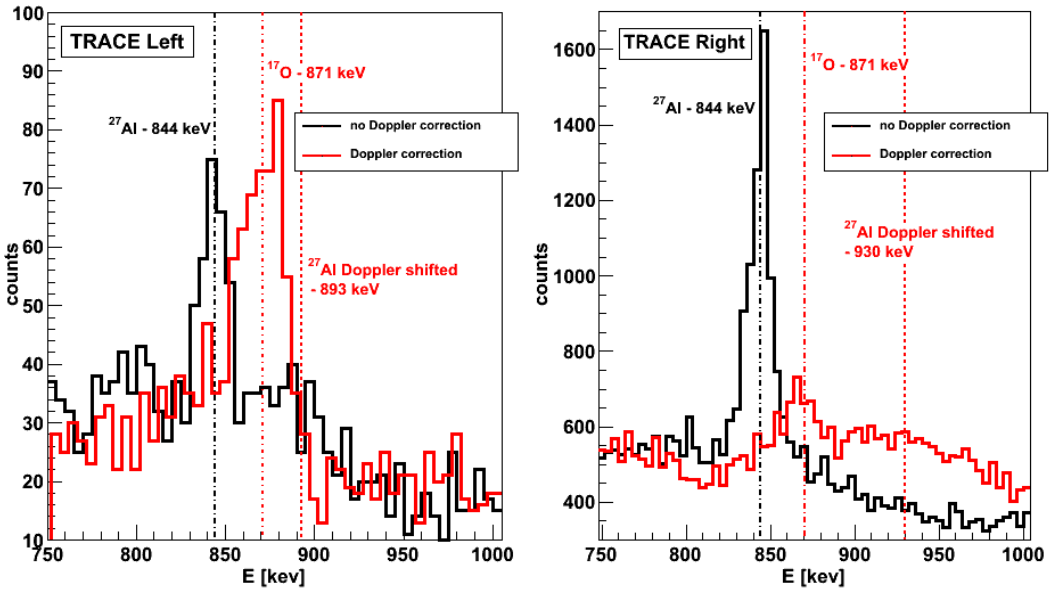

Fig. 6.11 - Energy spectra of the gamma-rays in coincidence with an ^{17}O ion measured in the left (left panel) or right (right panel) TRACE telescope. The red spectra are Doppler corrected, the black spectra are without correction. The dash-dotted lines mark the positions of the background line of ^{27}Al (in black) and of the ^{17}O line (in red); the dotted lines mark the position where the ^{27}Al line is shifted by the correction.

6.4.1. DOPPLER CORRECTION FOR THE TARGET-LIKE PARTNER

The scattering of the ^{17}O beam transfers some recoil kinetic energy to the target nuclei. The amount of this recoil energy can be calculated with simple kinematics considerations, as shown in Appendix A.

The speed obtained for the recoil is of the order of 0.5% of the speed of light. While this value of β is quite small, it is enough to cause a shift of more than 10 keV for high-energy gamma-rays. This can be seen clearly if we compare the gamma-ray energy spectrum obtained in coincidence with an ^{17}O ion detected in the left telescope with the one in coincidence with the right telescope: due to the reaction kinematics (see also Appendix A), in one case the recoil goes away from the Demonstrator, while in the other it goes towards it, as shown in Fig. 6.12.

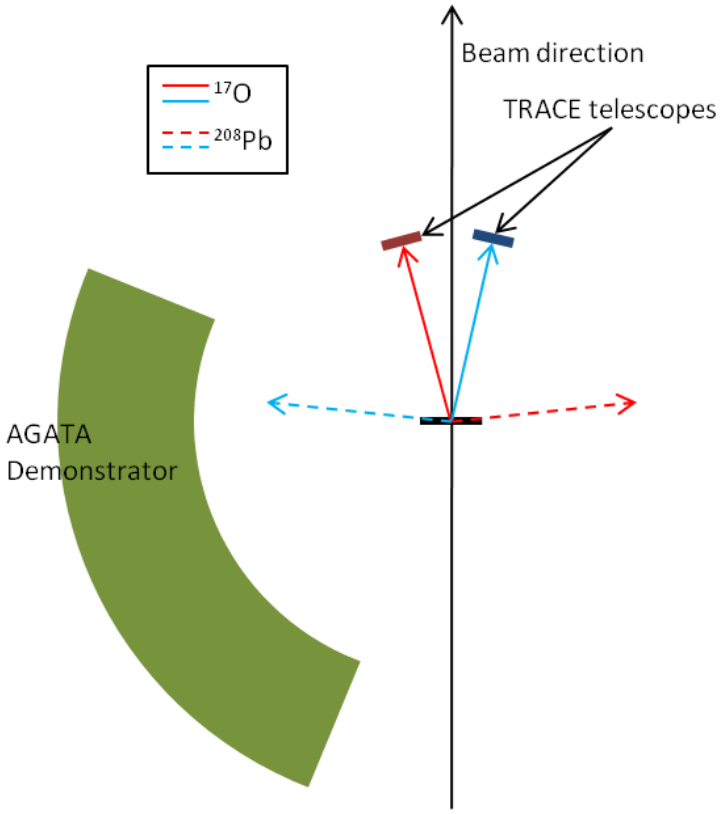

Fig. 6.12 - Schematic view of the direction of the ^{17}O ions (continuous line) and of the recoiling ^{208}Pb ions (dashed line) when an ^{17}O has been detected in the left (red) or right (blue) telescope.

Fig. 6.13 shows part of the "^{17}O left" and "^{17}O right" spectra measured with a ^{208}Pb target. The left panel shows the gamma decay from the first 3^- state, at an energy of 2614.5 keV; the two spectra show a peak at the same energy because the lifetime of the state is 17 ps, long enough for the ^{208}Pb nucleus to stop in the target before decaying, and have therefore a negligible Doppler shift. The right panel shows the decay from the first 2^+ state, at 4085.5 keV, and the two spectra are clearly shifted: one has a peak at 4069.1 keV and the other at 4098.2 keV; this is because the lifetime of the state is 0.8 fs (a factor of 20000 less than the 3^-) and the gamma-ray is emitted when the ^{208}Pb is still recoiling.

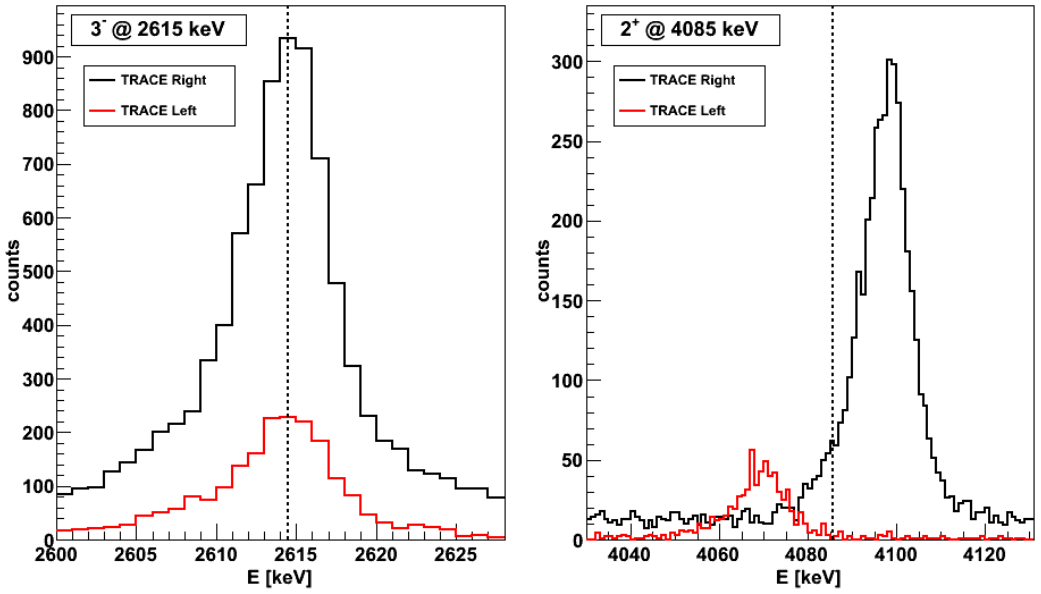

Fig. 6.13 - Energy spectra of the gamma-rays in coincidence with an ^{17}O ion measured in the left (red) or right (black) TRACE telescope. The left panel shows the energy range around to the first 3^- state of ^{208}Pb, which is not Doppler-shifted, the right panel shows the decay of the first 2^+ state, which is emitted in-flight.

In order to perform a Doppler correction for the recoil, we used equation A.5 to associate to each pad of the TRACE telescopes the velocity vector of the corresponding recoil, and kept a fixed value of v/c. It should be noted that, since the projectile has speed $\beta \sim 20\%$, the use of non-relativistic kinematics is not a very good approximation. However, we verified with the LISE++ [99], [100] kinematical calculator that the error related to this approximation is much smaller that the angular resolution of the TRACE telescopes.

The result of the Doppler correction is shown in Fig. 6.14 for the 4085 keV line of ^{208}Pb. The peaks in the black and red spectra correspond to the coincidence with the right and left telescopes: they have a smaller FWHM than in Fig. 6.13, but the energy is off by a few keV. It was not possible to determine why the Doppler correction did not obtain the correct value of energy, however, and it was decided to add a "recalibration coefficient" to the correction, obtaining the blue and purple spectra of Fig. 6.14.

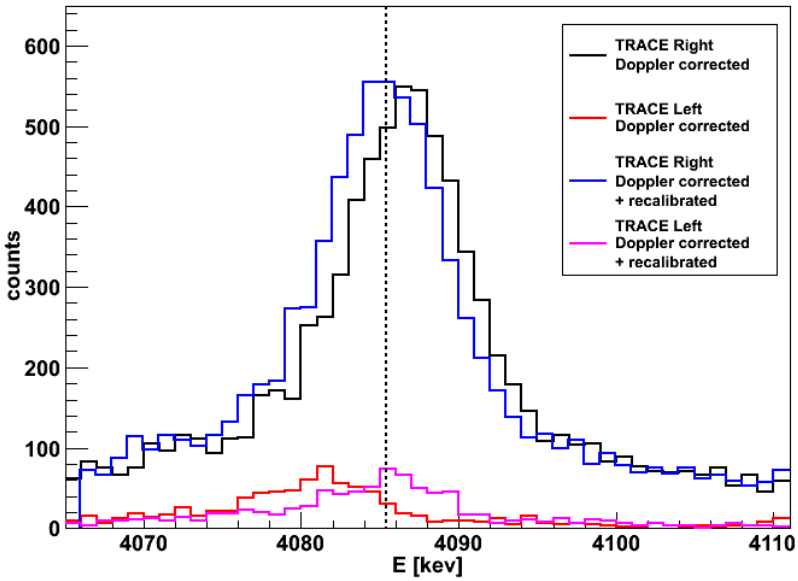

Fig. 6.14 - Energy spectra of the gamma-rays in coincidence with an ^{17}O ion measured in the left (red and purple) or right (black and blue) TRACE telescope. All spectra have been Doppler-corrected for the recoil motion of ^{208}Pb. The blue and purple spectra are just a recalibration of the black and red spectra in order to obtain the correct energy for the transition, marked by the dashed line.

6.5. Correlation with the Si telescopes

As mentioned in §5.3 for the analysis of the scintillator data, the TRACE telescopes were used for analysis of the experiment for two reasons: the first is the selection of the reaction channel (see §4.4); the second is the reduction of the background in gamma-ray spectra through the correlation of the measured gamma-ray energy to the excitation energy transferred to the target, measured by the Total Kinetic Energy Loss (TKEL) of the projectile, that is the difference between the Total Kinetic Energy (TKE) and the energy corresponding to an elastic scattering event.

Fig. 6.16 shows, in green, the energy spectrum of the gamma-rays detected, with the ^{208}Pb target, in coincidence with a scattered ^{17}O ion, while the red spectrum is obtained without any gating condition. Since both spectra are normalized to the total number of counts, it is clear how the selection of the ^{17}O scattering channel enhances greatly the intensity of ^{208}Pb transitions, in particular for the decay of the first 3^- state at 2614.5 keV and for the first 2^+ state at 4185.5 keV.

In order to correlate the gamma-ray energy to the TKEL, we performed a diagonal cut on the matrix in Fig. 6.15, which shows the TKEL measured event by event against the gamma-ray energy. The diagonal cut removes both the gamma decay from higher lying states (seen in the bottom right part of the matrix) and the gamma-rays corresponding to a random coincidence with an elastic scattering event (the vertical structure in the left part of the matrix).

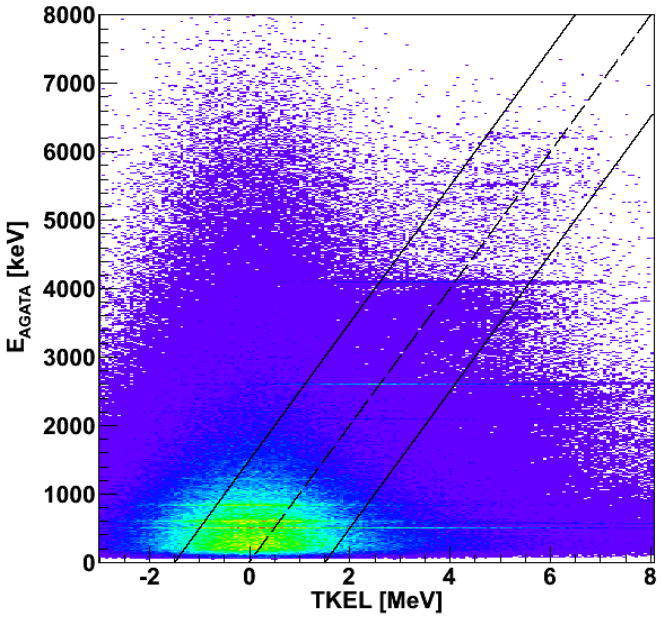

Fig. 6.15 - Scatter plot showing the TKEL versus the gamma-ray energy measured by the AGATA Demonstrator. The diagonal lines mark the region that was selected for the study of the ground-state decay, that is ±1.5 MeV large.

Fig. 6.16 shows, in blue, the energy spectrum of the gamma-rays whose energy is equal to the TKEL, again normalized to the total number of counts. It is evident how the transitions corresponding to the ground-state decay of the first 3^- and 2^+ states, in the inset, are greatly enhanced compared to the green spectrum, and transitions between excited states (such as the line at 583 keV, corresponding to the decay from the 5^- state at 3197 keV to the first 3^- state) and from the ^{207,206}Pb isotopes (produced by neutron emission from the ^{208}Pb target at high excitation energies, see also Fig. 6.19) are suppressed. The ^{27}Al transition is enhanced by the gate on TKEL because it is present as a random coincidence with an elastic scattering event (see

also Fig. 6.18), and the energy resolution of the Si telescopes does not allow to completely clean those events for energies smaller than ~2 MeV.

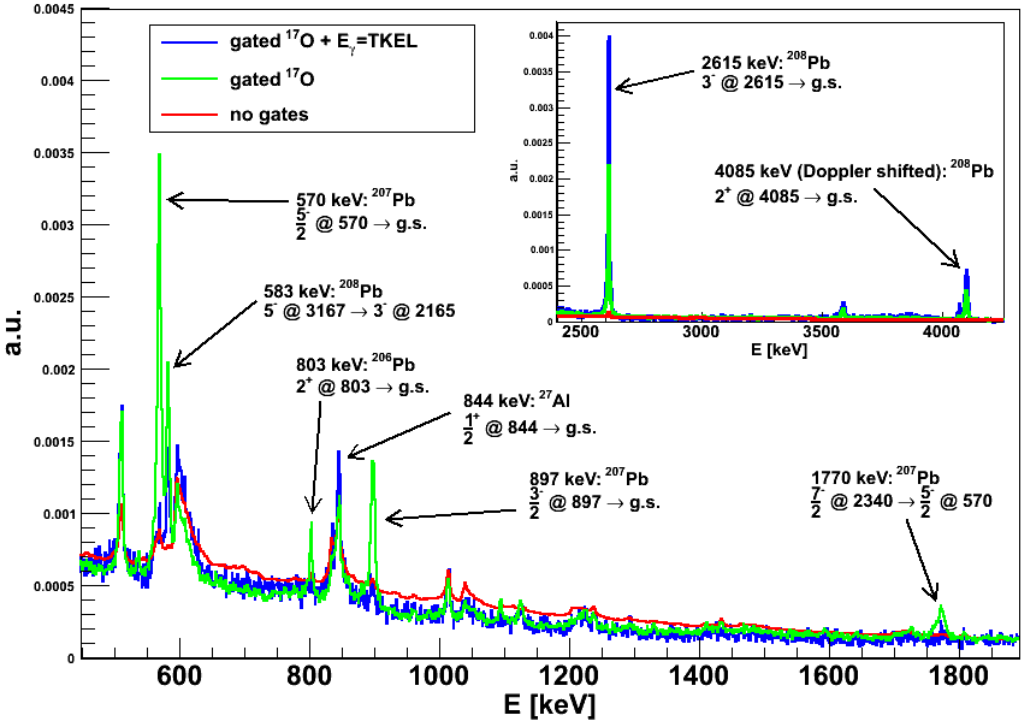

Fig. 6.16 - Energy spectra measured with the AGATA Demonstrator under different gating conditions: the red spectrum is without any gate, the green spectrum is gated on the ^{17}O scattering channel and on the coincidence peak of the time spectrum, and the blue spectrum has the additional requirement that the energy be equal to the TKEL within a ±1.5 MeV large window. All spectra are normalized to the total number of counts.

The correlation between Si and HPGe detectors was also verified by performing several diagonal cuts on the matrix in Fig. 6.15, requesting that $E_\gamma = TKEL + E_0$, with E_0 being an offset ranging from -2 MeV to +2 MeV. Fig. 6.17 shows the energy spectra resulting from such projections for the ^{208}Pb measurement. The intensity of ground-state transitions is reduced as E_0 gets different than 0, while transitions between excited states becomes stronger for $E_0 < 0$, that is for a gamma energy smaller than the TKEL (region right of the diagonal), while background lines become stronger for $E_0 > 0$, that is for a gamma energy larger than the TKEL (region above the diagonal).

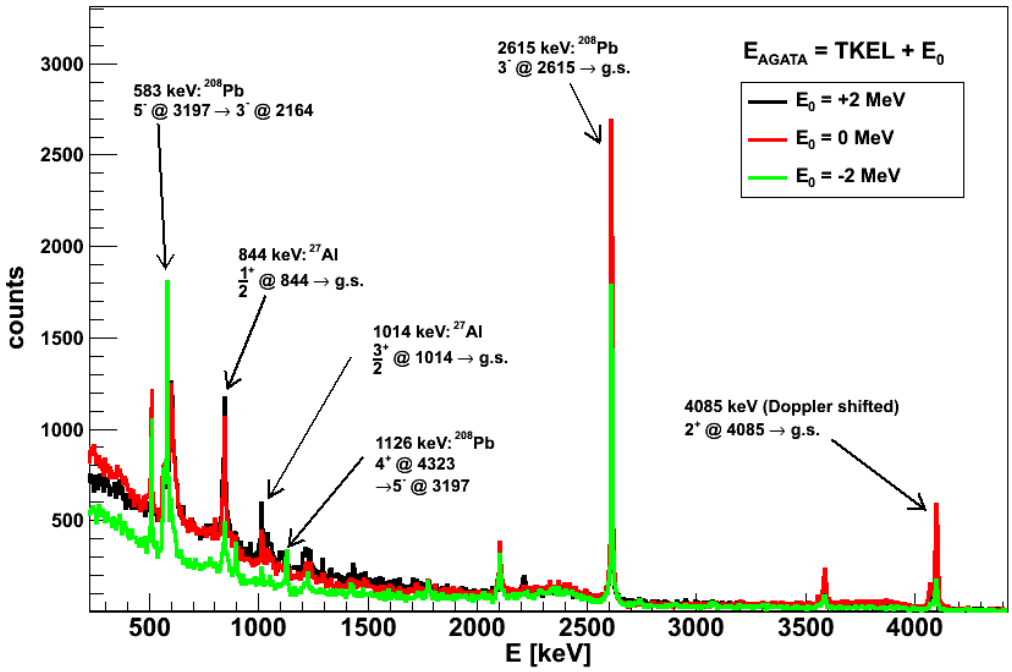

Fig. 6.17 - Energy spectra measured with the AGATA Demonstrator in coincidence with ^{17}O scattering with different gating conditions on the TKEL: the red spectrum shows gamma-rays with energy equal to the TKEL (corresponding to the diagonal region marked in Fig. 6.15); the black spectrum with energy larger than the TKEL by 2 MeV (corresponding to the region above the diagonal in Fig. 6.15); the green spectrum with energy smaller that the TKEL by 2 MeV (corresponding to the region left of the diagonal in Fig. 6.15); all 3 gates are within ±1.5 MeV large.

We should mention that in principle the top part of the matrix in Fig. 6.15 should be empty, since it corresponds to gamma-rays with an energy significantly larger than the TKEL, violating the energy conservation principle. These gamma-rays must come from random coincidences of an elastic scattering event with an uncorrelated gamma-ray. This is clear by comparing the energy spectrum of all gamma-rays measured in coincidence with an ^{17}O scattering event with the spectrum of the gamma-rays measured in coincidence with an elastic scattering event, shown in black and red respectively in Fig. 6.18; both are normalized to have the same area. All lines from the target are suppressed by the gate on the TKEL=0 region, while the transitions from ^{27}Al are enhanced; see also Fig. 6.16 and Fig. 6.17 for the identification of the transitions. The inset shows the same spectra, rebinned at 10 keV/ch, in the 4.5-8 MeV energy range; the strongest transitions from the ^{208}Pb PDR

decay are visible in the black spectrum (see also §6.7) and are completely absent from the red spectrum.

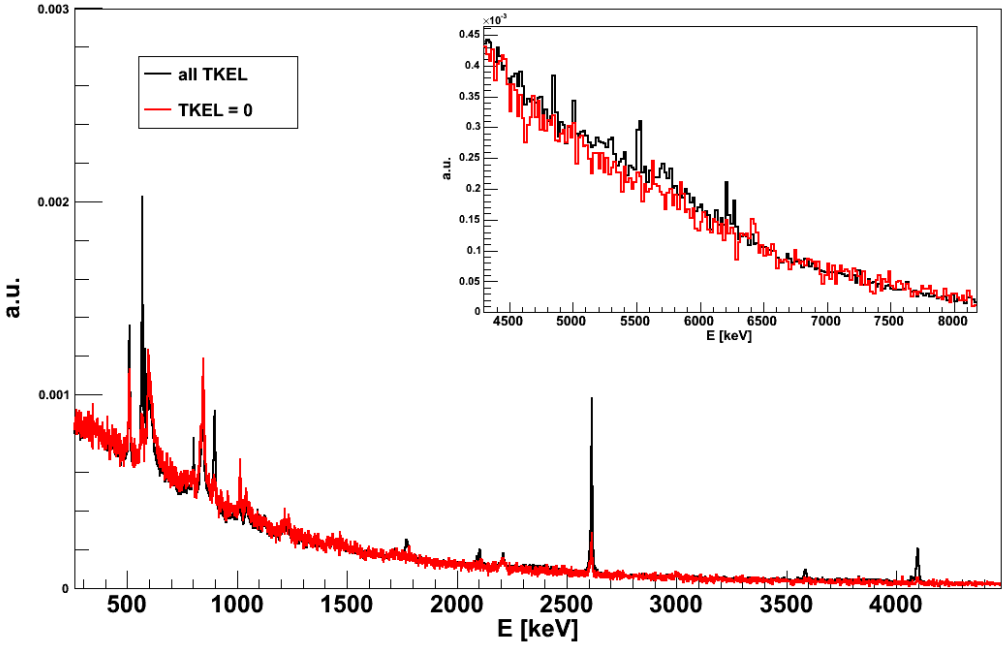

Fig. 6.18 - Energy spectrum of the gamma-rays measured in coincidence with the ^{17}O scattering channel; the black spectrum has no gating condition on the TKEL, while the red spectrum is gated on the elastic scattering with the requirement that $|TKEL| < 1\ MeV$. Both spectra are normalized to the total number of counts.

Another way to correlate the measured gamma-ray energy to the TKEL is to slice the matrix of Fig. 6.15 vertically, selecting the gamma-rays emitted for different intervals of TKEL. In Fig. 6.19 we show the gamma spectra corresponding to a TKEL smaller than the neutron separation energy S_n (in black, top panel); between S_n and the 2-neutron separation energy S_{2n} (in red, bottom panel); and above S_{2n} (in blue, bottom panel), for the ^{208}Pb (S_n= 7.4 MeV and S_{2n}= 14.1 MeV) target. It can be seen how the gamma lines from ^{208}Pb are greatly suppressed once the neutron emission channel opens, and a number of transitions from ^{207}Pb become visible; once the excitation energy is sufficiently high, ^{206}Pb transitions are also visible.

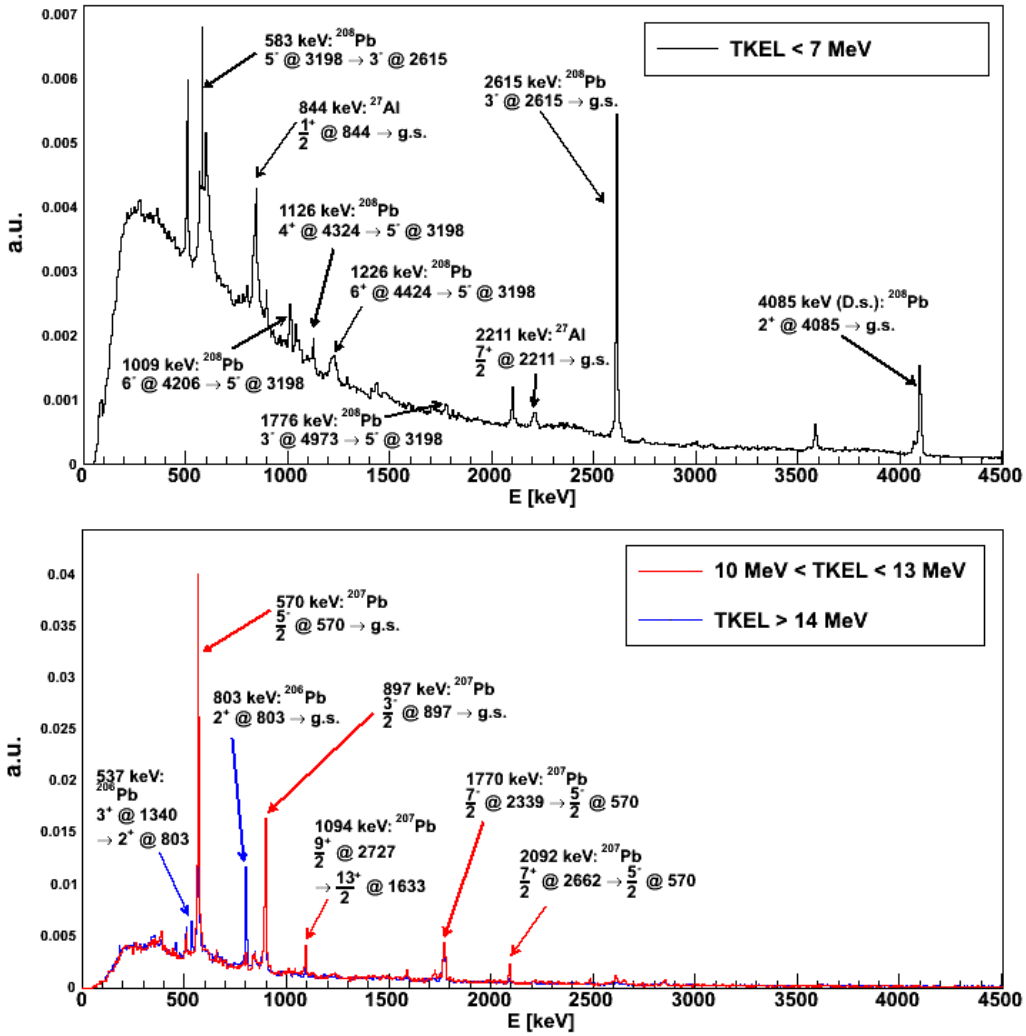

Fig. 6.19 - Energy spectra measured in the AGATA Demonstrator in coincidence with ^{17}O scattering, for the ^{208}Pb target, with different gating conditions on the TKEL: in the top panel, the black spectrum is gated on a TKEL smaller than S_n; in the bottom panel, the red spectrum is gated on a TKEL between S_n and S_{2n}, while the blue spectrum is gated with a TKEL larger than S_{2n}. Due to the resolution of the TRACE telescopes, a margin of 1-2 MeV had to be taken when performing the gates, as indicated in the legend.

The same has been done for the ^{90}Zr (S_n = 12 MeV, S_{2n} = 21 MeV) target, as shown in Fig. 6.20.

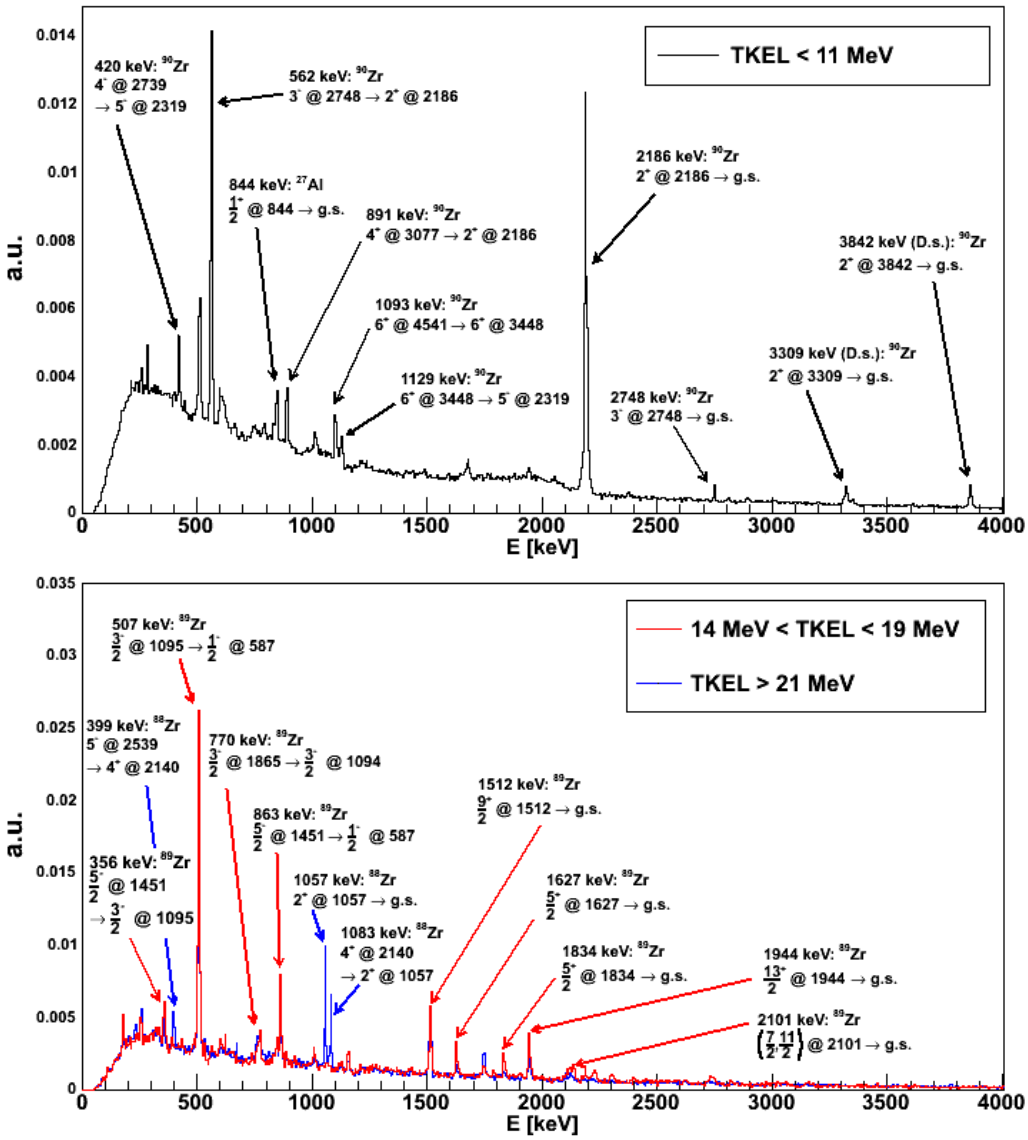

Fig. 6.20 - Energy spectra measured in the AGATA Demonstrator in coincidence with ^{17}O scattering, for the ^{90}Zr target, with different gating conditions on the TKEL: in the top panel, the black spectrum is gated on a TKEL smaller than S_n; in the bottom panel, the red spectrum is gated on a TKEL between S_n and S_{2n}, while the blue spectrum is gated with a TKEL larger than S_{2n}. Due to the resolution of the TRACE telescopes, a margin of 1-2 MeV had to be taken when performing the gates, as indicated in the legend.

Finally, we show in Fig. 6.21 the energy spectra measured with the Demonstrator over the range 0 - 15 MeV, with a binning of 400 keV/ch, to give a measure of the statistics at high energy for the ^{208}Pb target (left panel) and the ^{90}Zr target (right panel). We performed both the diagonal cuts described above, and a simple vertical cut between 5 and 25 MeV. Unfortunately, it can be seen how, both for ^{208}Pb and ^{90}Zr, the statistics becomes small after 7-8 MeV, especially at the energy of the ground-state decay of the ISGQR.

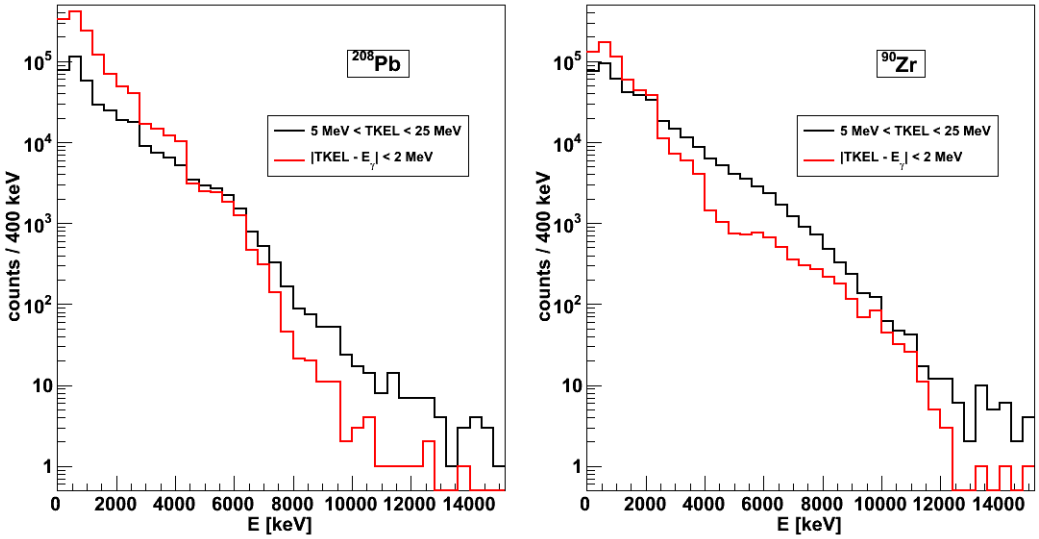

Fig. 6.21 - Energy spectra measured with the AGATA Demonstrator in coincidence with the ^{17}O scattering, in the 0-15 MeV energy range, binned to 400 keV/ch, with the ^{208}Pb target (left panel) and with the ^{90}Zr target (right panel). The black spectra are gated on the requirement that the TKEL be in the 5-25 MeV interval, the red spectra are gated on the requirement that the TKEL be equal to the gamma-ray energy within ±2 MeV. In either case, the statistics at the energy of the ground state decay of the ISGQR is quite low.

6.6. Removal of Compton-scattered gamma-rays

As mentioned in §3.1, the use of tracking algorithms can greatly improve the P/T ratio of the AGATA Demonstrator compared to traditional HPGe arrays. Unfortunately, a sizable fraction of the measured spectrum still corresponds to Compton-scattered gamma-rays; this is true in particular in our experiment, since only 3 triple-clusters out of the 5 that should compose the Demonstrator were available.

For this reason, we applied the Compton unfolding techniques implemented in the RADWARE software package and described in [101], which we will now briefly recall. The main idea of the unfolding procedure is to subtract the Compton continuum associated to each photopeak through a deconvolution of the detector response function. The spectrum is scanned starting from the highest energy, and for each channel the background is calculated with the assumption that only photopeak counts are left in the bin and subtracted.

This requires an accurate knowledge of the detector response as a function of the primary photon energy. The response function can be measured with monochromatic gamma-ray sources only at selected energies, so that a dedicated technique is necessary to interpolate and extrapolate the response function at all the other energies.

In particular, the technique described in [101] divides the Compton background in 3 components, corresponding to the backscatter peak, the continuum, and the Compton edge. When interpolating the experimental data, each component is transformed smoothly as a function of energy. The response function also takes into account the intensity of the first and second escape peak, which are taken as 1 channel large so that as the photopeak is scanned, two escape peaks with the same shape and width are subtracted.

In our case, the response function of the AGATA Demonstrator was computed with the GEANT4 simulation code developed by E. Farnea [102] for various photon energies, going from 1 MeV to 15 MeV. The GEANT4 code gives as an output a file containing all the interaction points for each primary event; this file was used to perform the tracking on the simulated data with the MGT code [70], which is the same we used for the experimental data.

We tuned the parameters of the unfolding algorithm on the energy spectrum measured with the AmBe-Ni source, since it is important for us to perform the procedure correctly at high energies. The results of the unfolding procedure is shown in Fig. 6.22 for the AmBe-Ni spectrum: the black spectrum is the original, the red spectrum is after the unfolding. The Compton shoulder and first escape peak of the large peak at 4.4 MeV is not completely removed, probably because of the large

width of the line (which is Doppler broadened, see §6.3). The inset shows the 3 most energetic lines in the spectrum, and how the unfolding procedure cleanly removes both the Compton continuum and the escape peaks.

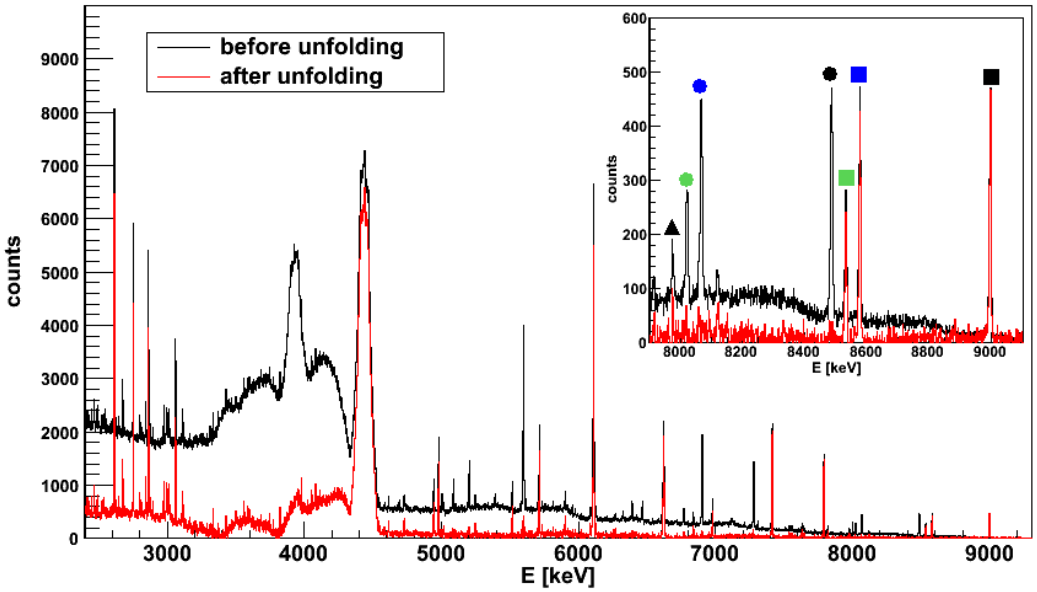

Fig. 6.22 - Energy spectra measured with the AGATA Demonstrator for the AmBe-Ni composite source, before (in black) and after (in red) the unfolding procedure. The inset shows the 3 highest energy lines, and how the unfolding keeps the Full Energy Peak (FEP, squares) while removing the first (circles) and second (triangles) escape peaks. The colours of the markers refer to the 3 different energies of the primary gamma-rays (see also Tab. 6.1).

6.7. Gamma decay from the Pygmy Dipole Resonance

As mentioned in §1.6, the PDR is composed by a number of discrete states of 1^- nature, whose dominant decay channel is towards the 0^+ ground state. In order to measure the gamma decay from the PDR we therefore had to select the ^{17}O inelastic scattering channel and the coincidence peak in the time spectrum, as well as request that the gamma-ray energy be equal to the TKEL within detector resolution, as explained in §6.5. Furthermore, since the typical lifetime of these states is of the order of the femtosecond, a Doppler correction for the recoil was also performed (see §6.4.1).

Fig. 6.23 shows the gamma-ray energy spectrum obtained with these conditions, over all the statistics collected with the ^{208}Pb target (top panel) and ^{90}Zr target (bottom panel), before unfolding (in black) and after unfolding (in red). The spectra have been unfolded with a 2 keV/ch binning and rebinned afterwards for clarity.

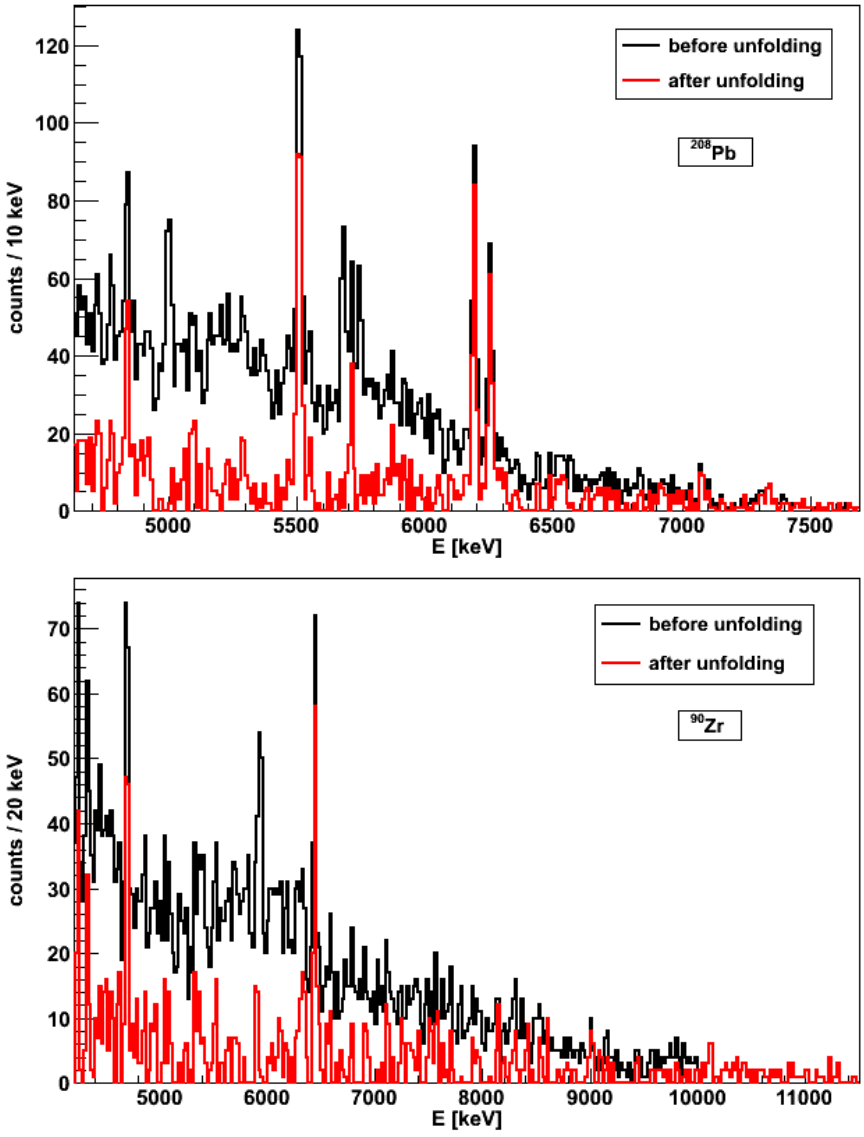

Fig. 6.23 - Gamma decay in the PDR region measured with the ^{208}Pb target (top panel) and with the ^{90}Zr target (bottom panel); the black spectra are made with the gating conditions described in text, the red spectra are obtained with the unfolding procedure.

Fig. 6.24 shows the unfolded gamma-ray energy spectra for ^{208}Pb, where the arrows mark the energies at which PDR transitions have been measured with the NRF technique [34], [35]; the green arrows correspond to transitions we observe (with dashed lines when the identification is not clear), the grey lines correspond to transitions we do not observe, and the red arrows correspond to known E2 transitions. The width of each line is proportional to the B(E1) value reported in [34].

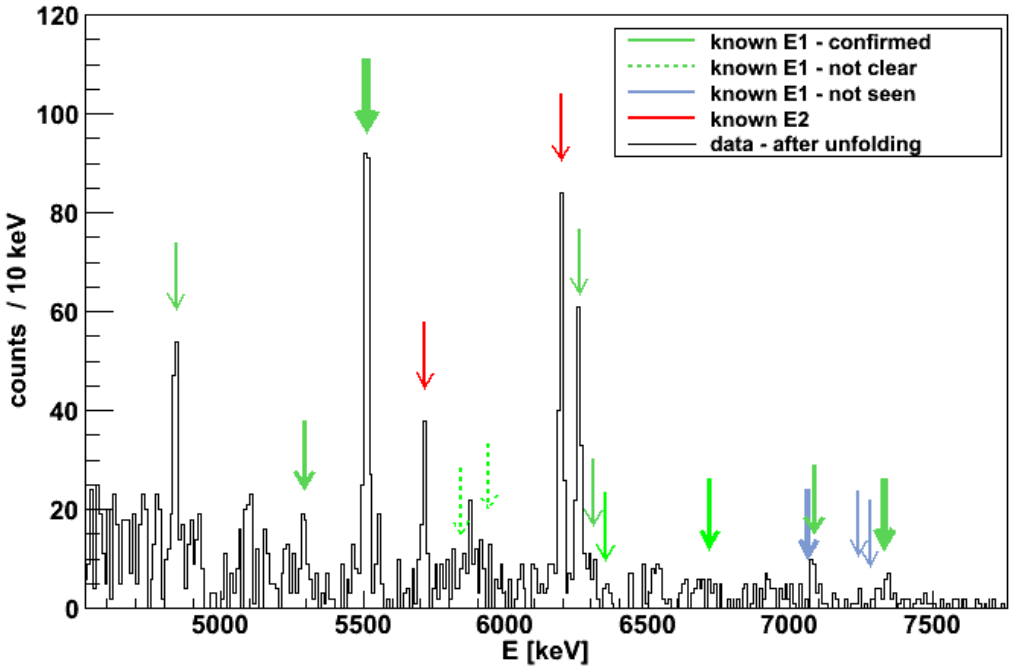

Fig. 6.24 - Energy spectrum measured with the AGATA Demonstrator for the gamma decay from the PDR of ^{208}Pb, with the gating conditions described in text and the unfolding. The arrows mark the known transitions reported in [34].

In the case of ^{90}Zr the larger fragmentation of the dipole strength makes it possible to clearly identify only the strongest transitions; all the lines visible in Fig. 6.23, bottom panel, were also observed in [103].

6.8. Angular distributions

We know from previous NRF experiments that the energy spectrum we measured in the PDR region is dominated by E1 transitions, but some E2 transitions are also

present. It is interesting to see if it is possible to separate the two contributions through the different angular distribution of the emitted gamma-rays.

The angular distribution associated with an electromagnetic transition from a state $|J_i\rangle$ to a state $|J_f\rangle$ is given by:

$$W(\theta) = \sum_{m_i,\mu} \left|\langle J_i m_i \lambda\mu | J_f m_f\rangle\right|^2 P(m_i) Z_{\lambda\mu}(\theta) \qquad (6.3)$$

where $P(m_i)$ is the population probability of each magnetic component m_i of the initial state, and $Z_{\lambda\mu}(\theta)$ is the angular distribution for photons of multipolarity λ with component μ, which can be calculated exactly (see for example [104]).

If $P(m_i)$ has the same values for all the components, the symmetry properties of $Z_{\lambda\mu}(\theta)$ make the resulting angular distribution isotropic: it is therefore possible to observe an angular distribution for a gamma transition only when the initial state is oriented with respect to a symmetry axis, breaking the rotational symmetry.

Typically, the excited states formed in nuclear reactions are oriented with respect to the beam direction. The degree of orientation depends on the formation process and therefore on the reaction mechanism. While we expect a certain degree of alignment in the case of our experiment, we are still working on calculating the $P(m_i)$ coefficients for our reaction. For this reason we are able to make only qualitative observations on the angular distributions.

When evaluating the angular distribution of gamma-rays measured with a traditional detector array one has to count the gammas detected in each individual detector, and plot this number against the detector angle. In the case of the AGATA Demonstrator, however, it is possible to know where each gamma-ray is detected with a much better precision, thanks to the PSA and tracking algorithms.

For this reason, we treated the AGATA Demonstrator as a continuous HPGe detector, and considered for each gamma-ray the angular position of the first interaction point with respect to the beam direction. Fig. 6.25 shows the angular distribution obtained in this way for the 1408 keV line of a ^{152}Eu source, placed at target position, which serves as an efficiency calibration for our detector.

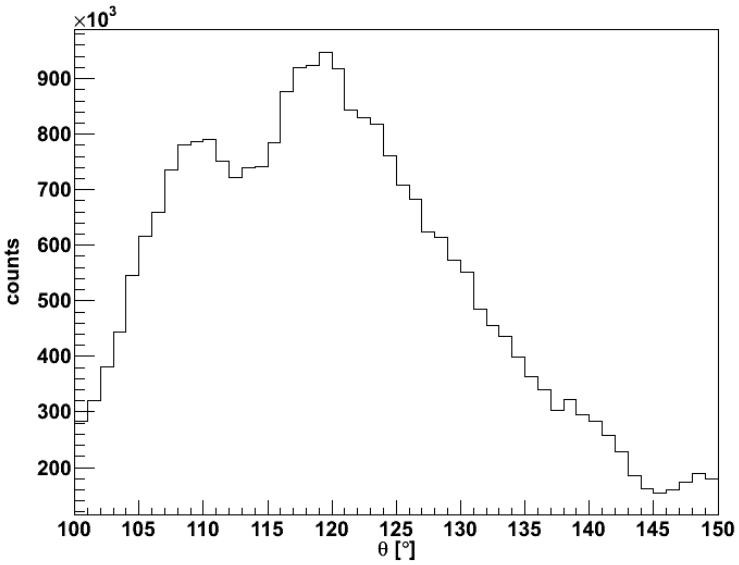

Fig. 6.25 - Number of counts measured at different angles by the AGATA Demonstrator for the 1408 keV line of a ^{152}Eu source placed at the target position

It is clear that the efficiency varies greatly with the angle, due to the irregular geometry caused by the presence of only 3 out of 5 triple-clusters, and due to the fact that the Demonstrator was moved 10 cm closer to the target compared to the design position (see §3.1.6).

We divided the angular range between 100° and 150° in 5 bins, and measured the efficiency at 1408 keV for each angle with the ^{152}Eu source. We then measured for each angle the intensity of the strongest E1 and E2 transitions in the ^{208}Pb spectrum, that are found at 5512 keV and 4085 keV respectively, and divided it by the efficiency. This gives us a qualitative estimate of the angular distribution: we would need to evaluate the efficiency at each angle at the correct energy instead of taking the one measured at 1408 keV, but it is still useful to see if there is a signature of different distributions for the two transitions. As a matter of fact, it can be seen in Fig. 6.26, left panel, how the two distributions have very different slope (note that both distributions are normalized to the value of the first bin). Similar distributions are obtained with the ^{90}Zr target.

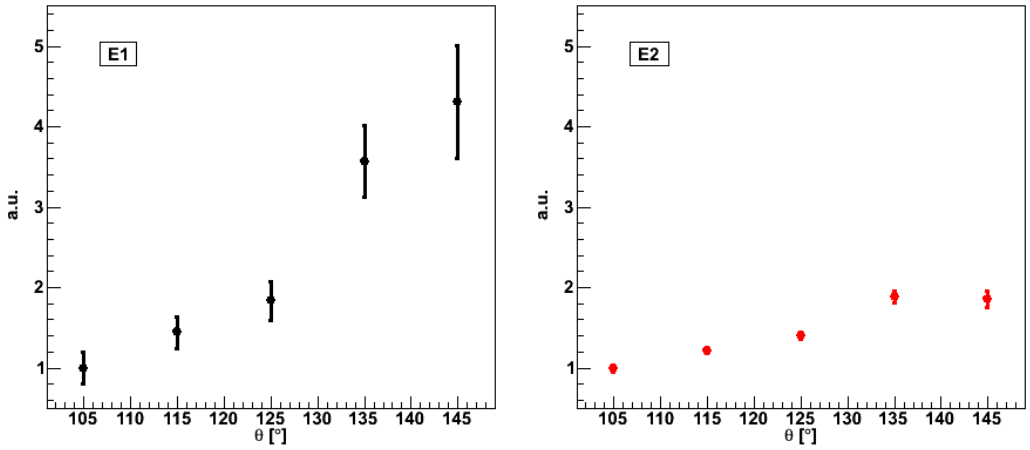

Fig. 6.26 - Absolute angular distribution of the strongest E1 (at 5512 keV, left panel) and E2 (at 4085 keV, right panel) transitions of ^{208}Pb, normalized to the value of the first bin.

Due to the relatively small statistics in the PDR transitions and to the rather small angular range covered by the 3 AGATA triple-clusters, it is difficult to compare the angular distribution of the PDR lines to the reference ones. We therefore used a more simple approach of comparing the integral of each line in the angular range between 100° and 125° ("left" spectrum) against the integral in the range between 125° and 150° ("right" spectrum).

We show in Fig. 6.27 the ratio of the integral in the "right" spectrum over the integral in the "left" spectrum for several E1 (in black) and E2 (in red) transitions, both for the ^{208}Pb (left panel) and ^{90}Zr (right panel) measurements. The horizontal dashed lines mark the values of said ratio for the strongest E1 and E2 transitions, taken as reference values. The blue square represents the integral over the whole pygmy region, showing as expected an E1 behaviour; note that for data with the ^{208}Pb target the part below 6.4 MeV was cut because of the presence of strong E2 contaminants.

There is therefore a signature for a different angular distribution of E1 and E2 transitions: this is important, because it shows the capability of this technique to separate the two contributions to the energy spectra.

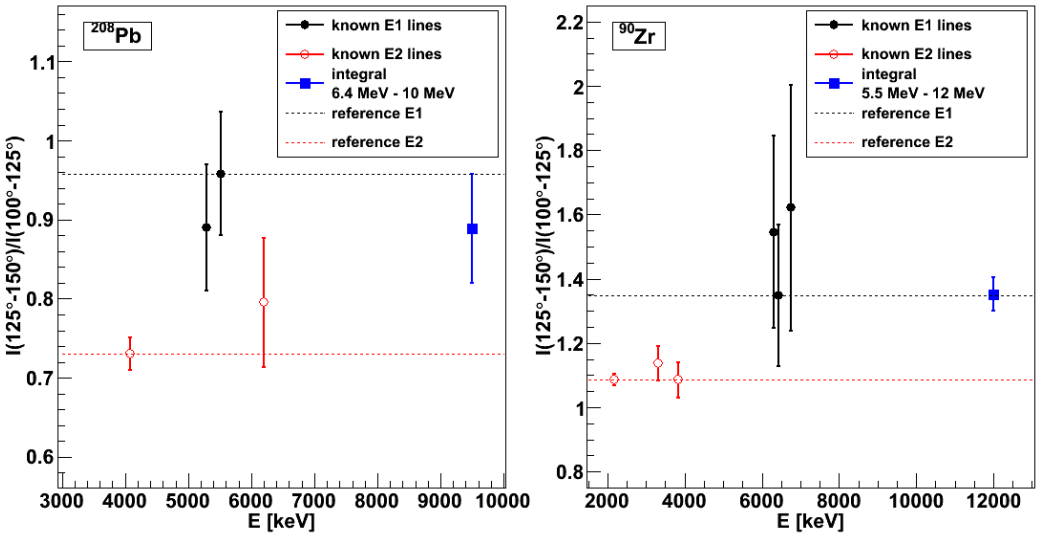

Fig. 6.27 - Ratio between the number of counts in the 100°-125° angular range over the number of counts in the 125°-150° angular range, measured with the AGATA Demonstrator for various transitions in the PDR region of ^{208}Pb (left panel) and ^{90}Zr (right panel). The black circles correspond to E1 transitions, the red circles to E2 transitions, and the blue squares to the integral of the whole PDR region. Note that the values of the ratio for E1 and E2 transitions are different in the two cases, possibly because of a different alignment of the two reactions or because of the different reaction kinematics.

6.9. Evaluation of the B(E1) for the PDR states

Due to the dipole electric nature of the PDR, a comparison of the experimental results with theoretical calculations requires the extraction of the B(E1) for each state of the resonance from the experimental cross-sections. Following from [62], we therefore use the relation:

$$\frac{d^2\sigma}{d\Omega dE} = B_{E1}(E)\left[\frac{d\sigma}{d\Omega}\right]_{B_{E1}=1} \qquad (6.4)$$

where $\frac{d^2\sigma}{d\Omega dE}$ is the excitation cross-section, $B_{E1}(E)$ is the distribution of E1 reduced transition probability as a function of energy, and $\left[\frac{d\sigma}{d\Omega}\right]_{B_{E1}=1}$ is the DWBA cross-section for a unit E1 strength.

The latter term was calculated by performing the DWBA calculations for E1 states of fixed strength at the energies of the known PDR lines, as shown in Fig. 6.28, left

panel. The cross-sections were integrated over the angular range covered by the TRACE telescopes (marked by the two vertical lines).

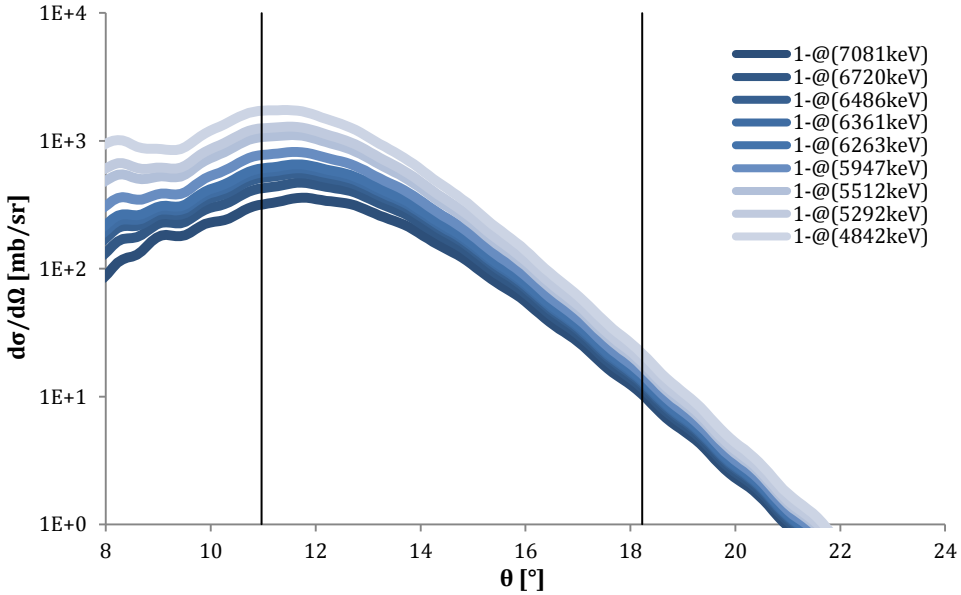

Fig. 6.28 - DWBA cross-sections calculated with the PTOLEMY code for the population of an E1 state of unit strength at different energies; the vertical lines mark the integration interval of the cross-section.

In principle, the absolute cross-section obtained from the DWBA calculation should be compared to the experimental cross-section, obtained from the spectra as

$$\frac{d\sigma}{dE} = \frac{N_\gamma(E)}{\varepsilon(E) N_{beam} N_{target}} \qquad (6.5)$$

where $N_\gamma(E)$ is the number of gamma-rays measured at an energy E, $\varepsilon(E)$ is the absolute efficiency of the gamma-ray detection array at the energy E (which should take into account also the angular distribution of the gamma-rays), N_{target} is the number of target nuclei per unit surface, and N_{beam} are the number beam nuclei that passed through the target during the whole measurement. Unfortunately, the latter term could not be evaluated, because no calibrated faraday cup was available for use as a beam dump.

We can, however, evaluate the relative strength of each state compared to a reference one, and scale all B(E1) values with the value for the reference state found in literature: from Eq. 6.4 and Eq. 6.5 one obtains that the number of counts in a line

at energy E_x is proportional to the strength of the line, the DWBA estimate for a transition of unit strength and energy E_x, and to the absolute efficiency of the detector array:

$$N(E_x) \propto B(E1)_x \sigma_{B_{E1}=1}(E_x)\varepsilon(E_x) \qquad (6.6)$$

From this, it follows that the relative strength for a state at energy E_x can be evaluated with:

$$B(E1)_x = B(E1)_{ref} \frac{N_x/\varepsilon_x}{N_{ref}/\varepsilon_{ref}} \frac{\sigma_{B_{E1}=1}(E_{ref})}{\sigma_{B_{E1}=1}(E_x)} \qquad (6.7)$$

Note that we do not need to take into account the angular distributions of the gamma-rays because we are comparing E1 transitions to a reference E1 transition.

For the measurement with the ^{208}Pb target, we used as a reference line the strongest E1 transition, at 5512 keV, using the value of B(E1) measured in [34] as a reference. Fig. 6.29 shows the B(E1) values thus extracted for the ^{208}Pb E1 transitions in the region of the PDR (red circles), compared to the values in [34] (black diamonds). The dashed blue line represents our detection limit, estimated following [38].

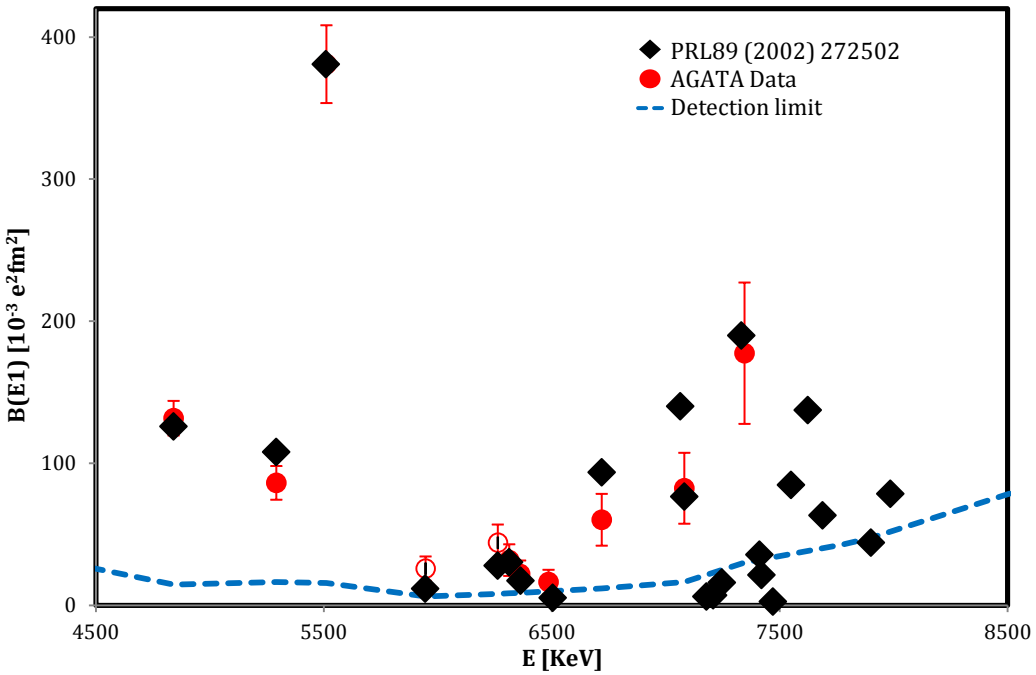

Fig. 6.29 - B(E1) strength of the ^{208}Pb PDR transitions measured with our setup (red circles) compared to the values in [34] (black diamonds); the blue dashed line represents the sensitivity limit of our measurement.

It can be seen how there are various transitions above 7.5 MeV of energy that should be visible given the sensitivity of our setup. We remark that, even though this energy is close to the neutron separation energy in ^{208}Pb (7.36 MeV), statistical model calculations performed with the NRV tool [105] show that the neutron branching becomes dominant only around 8.3 MeV of energy. Similar results were obtained with the LISE++ toolkit [99], [100].

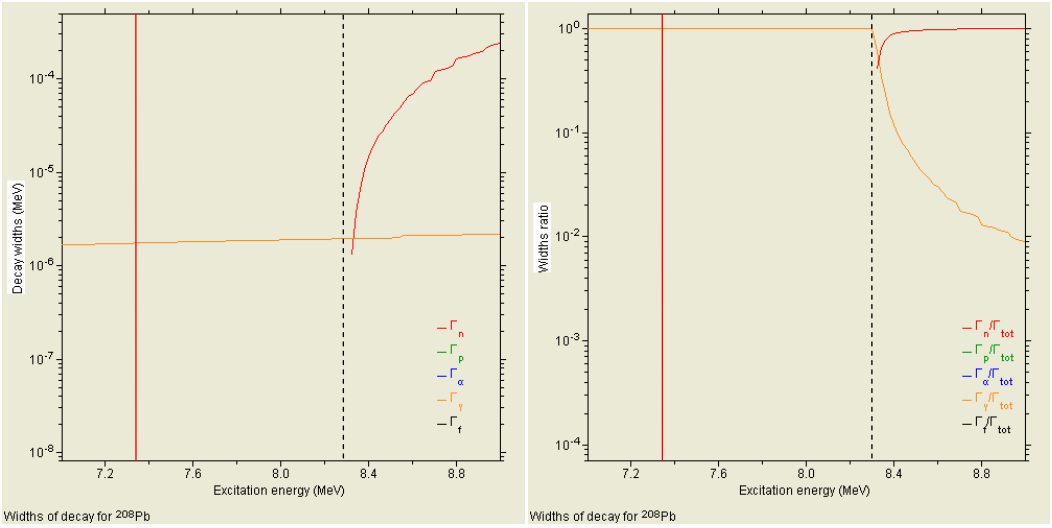

Fig. 6.30 - Absolute (left panel) and relative (right panel) decay widths for gamma (orange) and neutron (red) emission. The vertical red line marks the neutron separation energy at 7.36 MeV, the dashed black line marks the energy at which the neutron emission channel is no longer negligible.

We can therefore say that we are not observing the transitions between 7.5 MeV and 8.3 MeV because we lack the sensitivity or because of the neutron emission, but because such states are not excited by our probe. This points to a splitting of the PDR in ^{208}Pb analogous to what has been observed for lighter nuclei with the *(α,α'γ)* technique [36-39]: the low-energy part of the resonance is excited equally well by heavy ions and photons, while the high-energy part is weakly excited by ions. This splitting can be seen more clearly in Fig. 6.31, showing the convolution of the measured strength values with a Lorentz bell curve with a width of 500 keV; the red curve corresponds to the values in [34], the blue curve to our measurement. There is a remarkable overlap between the two curves below ~6.5 MeV, while for higher energies there is an abrupt change in the response for the two different probes.

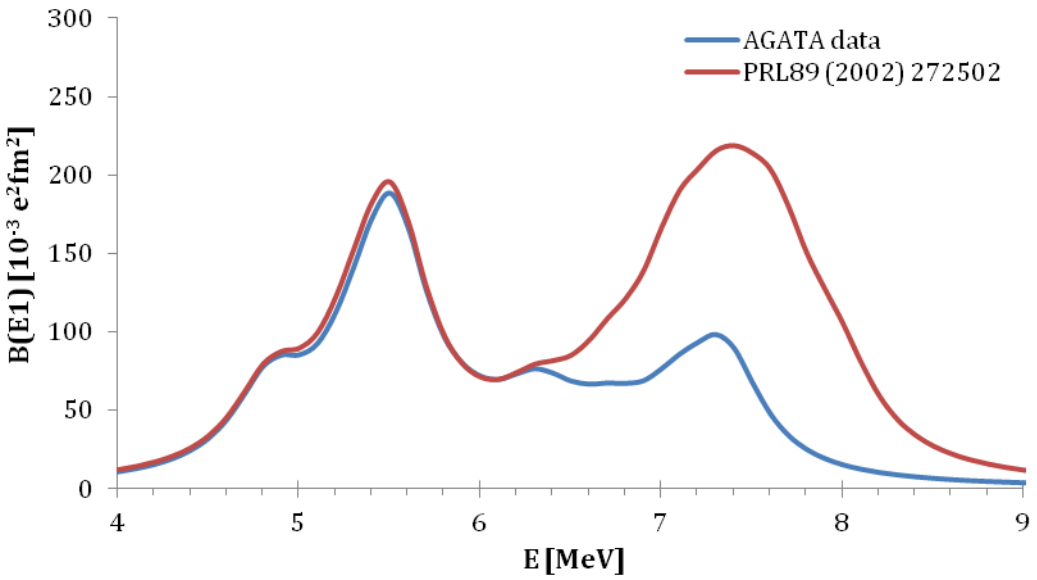

Fig. 6.31 - Experimental values of the B(E1) of the PDR in ^{208}Pb measured with our setup (in blue) and with the NRF technique (in red), convoluted with a Lorentzian curve with a width of 500 keV.

The B(E1) values for the ^{90}Zr transitions were evaluated with the same procedure as the ^{208}Pb transitions; we took the 6296 keV line as reference and used the values reported in [103]. Fig. 6.32 shows the B(E1) values extracted for the strongest transitions measured by our setup, compared to those of [103].

Again, the results point to a splitting of the PDR in ^{90}Zr in a low-energy, isoscalar component, and a high-energy, isovector component; this can be seen in Fig. 6.33, where the strength values measured in [103] (red curve) and in our experiment (blue curve) have been convoluted with a Lorentz bell curve with a width of 500 keV.

We can therefore say that the inelastic scattering of ^{17}O at 20 MeV/u was successfully used to measure the gamma decay from the PDR states of ^{208}Pb and ^{90}Zr, and that the results point to the presence of a splitting of the PDR similar to what has been observed with the *(α,α'γ)* techinque [36-39].

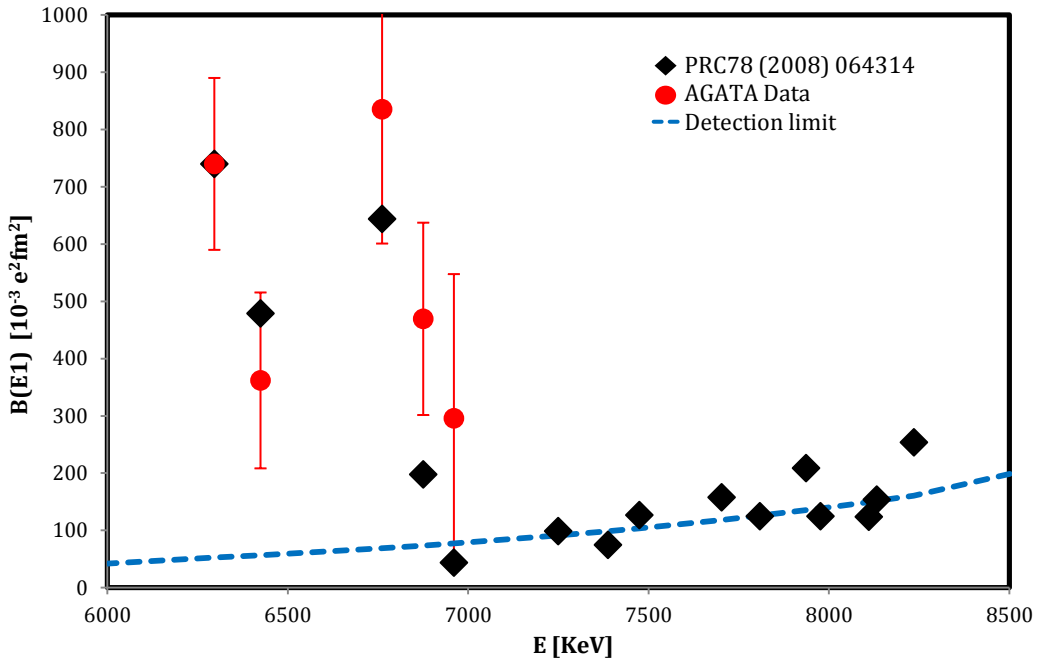

Fig. 6.32 - B(E1) strength of the ^{90}Zr PDR transitions measured with our setup (red circles) compared to the values in [34] (black diamonds); the blue dashed line represents the sensitivity limit of our measurement.

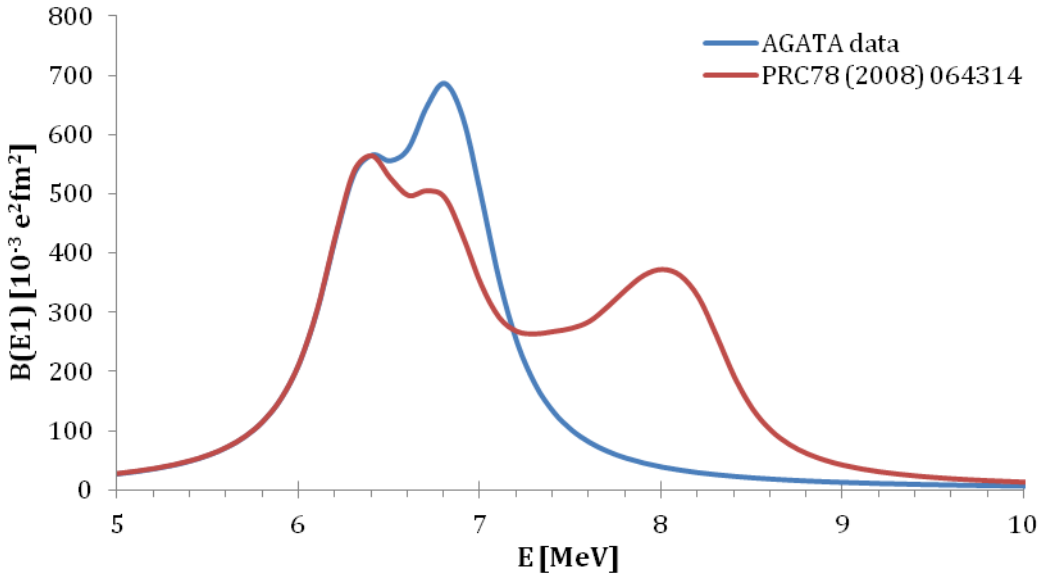

Fig. 6.33 - Experimental values of the B(E1) of the PDR in ^{90}Zr measured with our setup (in blue) and with the NRF technique (in red), convoluted with a Lorentzian curve with a width of 500 keV.

Conclusions

This thesis work has concerned the experimental study of pygmy resonance states in the ^{208}Pb and ^{90}Zr nuclei, excited by the inelastic scattering of a ^{17}O beam at the energy of 20 MeV/u. The gamma decay from such states has been measured with the AGATA (Advanced GAmma-ray Tracking Array) Demonstrator HPGe array, coupled to an array of $LaBr_3$:Ce and BaF_2 scintillators. The beam-like ejectiles were measured, in coincidence with the gamma-rays, by two segmented Si telescopes, in order to identify the reaction channel. The experiment has been performed at the Legnaro National Laboratories in June 2010, and was one of the first physics measurements exploiting the gamma-ray tracking capabilities of the AGATA detectors.

The analysis focused on the identification and selection of inelastic scattering events and on the correlation between the ejectile energy and the gamma-ray energy. This was first used to perform various consistency checks, in particular testing our selectivity for the ground state decay of the target nucleus, and then to study the gamma decay from highly excited states.

While it was not the main physics aim of the experiment, the gamma decay from the projectile-like ejectiles was also studied, by performing the appropriate correction for the Doppler effect. The energy resolution obtained at the energy of the first excited state of ^{16}O, at 6129 keV, was of 58 keV FWHM. This value was limited by the relatively poor angular resolution of the Si telescopes, and more than 10 times better than what we could have achieved with a traditional HPGe array.

Concerning the gamma decay from the PDR states, a number of strong transitions in the pygmy region was observed for both target nuclei, and the possibility of evaluating their multipolarity through angular distribution measurements has been verified. A relative measurement of the strength of the observed transitions was performed, comparing the measured intensities to the B(E1) values reported in literature. In both target nuclei, there are several transitions which should be above our sensitivity limit but are not visible in the data, all in the high-energy region of

the PDR, while most low-energy transitions are confirmed: this points to a splitting of the resonance analogous to what has been observed in the N=82 isotones with the *(α,α'γ)* technique. This is the first time such an effect has been measured in a different mass region and with a different probe.

The analysis performed in this work has demonstrated the unique possibility offered by heavy-ion scattering studies, in coincidence with an efficient gamma-detection, to obtain important structure information on the underlying nature of the pygmy states. A follow-up experiment has been recently performed with the same setup, focusing on the gamma decay from the pygmy resonance of ^{124}Sn and ^{140}Ce: this will allow for a direct comparison of the *(^{17}O,^{17}O'γ)* measurement with the *(α,α'γ)* data.

The experimental technique employed in this experiment could also be used at future facilities such as SPIRAL2 and SPES, which will be able to produce neutron-rich radioactive beams at energies of ~20 MeV/u, at least for some ions. It will then be possible to use the inelastic scattering of such beams on solid, weakly bound targets such as ^{13}C to study, in inverse kinematics, the structure of the pygmy resonance in more neutron-rich systems.

Appendix A. Binary reaction kinematics

This appendix will discuss the kinematics of a binary interaction of the type:

$$a + A \rightarrow b + B \qquad (A.1)$$

where a is an incoming beam ion of mass m_a and velocity $\overrightarrow{v_a}$, A is a target nucleus of mass m_A, at rest in the laboratory frame of reference, and the reaction products are a lighter, beam-like ejectile b with mass m_b and velocity $\overrightarrow{v_b}$, and a heavier, target-like recoil B with mass m_B and velocity $\overrightarrow{v_B}$.

First, we will give expressions that relate quantities appropriate for the laboratory coordinate system; afterwards, we will give formulas for the transformation of quantities between laboratory and centre-of-mass frames of reference.

For simplicity, only classical kinematics have been considered, neglecting relativistic effects.

A.1. Laboratory frame of reference

The assuming that A is at rest, the laws of energy and momentum conservation imply that:

$$K_a = K_b + K_B - Q \qquad (A.2)$$

and

$$\begin{aligned} m_a v_a &= m_b v_b \cos\theta_b + m_B v_B \cos\theta_B \\ m_b v_b \sin\theta_b &= m_B v_B \sin\theta_B \end{aligned} \qquad (A.3)$$

where the angles θ_b and θ_B are defined in Fig. A.1, left panel. K_a, K_b, K_B are the kinetic energies of a, b, and B; Q is the Q-value of the reaction, that is the difference between the initial and final mass of the system:

$$Q = (m_a + m_A - m_b - m_B)c^2 - E_{ex} \qquad (A.4)$$

where E_{ex} is the excitation energy transferred to the internal degrees of freedom of either nuclei.

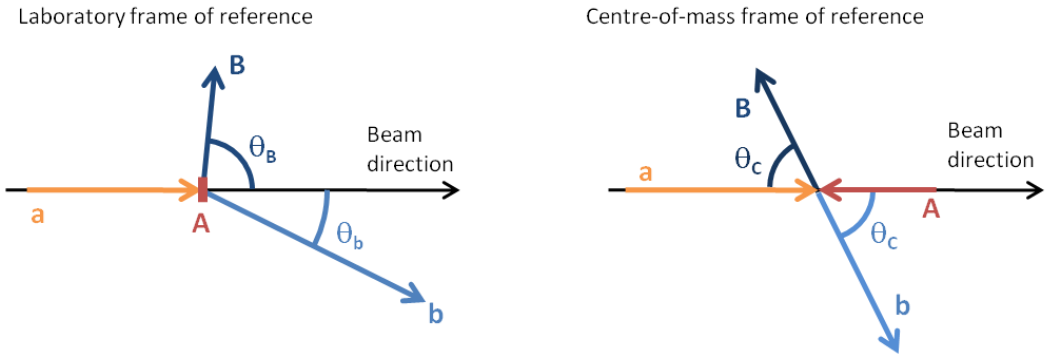

Fig. A.1 - Schematic view of a binary reaction in the laboratory and in the centre-of-mass frame of reference.

From Eq. A.3, it is very easy to calculate that

$$\tan\theta_B = \frac{\sin\theta_b}{\sqrt{\frac{m_a K_a}{m_b K_b} - \cos\theta_b}} \qquad v_B = v_b \frac{m_b \sin\theta_b}{m_B \sin\theta_B} \qquad (A.5)$$

Making use of Eq. A.2 it is also possible to calculate the relation between K_b and θ_b for given values of Q and K_a, but that is outside of our interest.

A.2. CENTRE-OF-MASS FRAME OF REFERENCE

In experimental nuclear physics, all observations take place in a reference frame that is at rest in the laboratory, referred to as the laboratory frame of reference. From the theoretical point of view, however, the motion of the centre of mass is of no consequence for the properties of a nuclear reaction. It is then often more convenient to use a moving coordinate frame in which the centre of mass of the two colliding nuclei is at rest, called the centre-of-mass coordinate system.

In the centre-of-mass frame of reference, both nuclei are moving towards each other with equal and opposite momenta:

$$m_a v'_a = m_A v'_A \qquad (A.6)$$

where v'_a and v'_A are projectile and target speed in the centre-of-mass system.

If v_{CM} is the speed of the centre of mass in the laboratory frame of reference, then by definition of centre of mass one has

$$v_{CM} = v_a \frac{m_a}{m_a + m_A} \qquad (A.7)$$

meaning that the velocities of a and A in the centre-of-mass system are:

$$\begin{aligned} v'_a &= v_a - v_{CM} = v_a \frac{m_A}{m_a + m_A} \\ v'_A &= -v_{CM} = -v_a \frac{m_a}{m_a + m_A} \end{aligned} \qquad (A.8)$$

After the collision, b and B move in opposite direction in the centre-of-mass frame, due to momentum conservation, as shown in Fig. A.1, right panel; their direction forms an angle θ_C with the direction before the collision (that is the beam direction). This implies that

$$m_b v'_b = m_B v'_B \qquad (A.9)$$

where v'_b and v'_B are the speeds of b and B in centre-of-mass system, related to the speeds in the laboratory system by:

$$\begin{aligned} v'_b \cos\theta_C &= v_b \cos\theta_b - v_{CM} \\ v'_b \sin\theta_C &= v_b \sin\theta_b \end{aligned} \qquad (A.10)$$

It should be noted that, if the Q-value is non-zero, the velocity of the centre of mass changes between the initial and final state, with the relation:

$$v_{CM,f} = v_{CM,i} \frac{m_a + m_A}{m_b + m_B} \qquad (A.11)$$

Typically, however, the Q-value is only $\sim 10^{-3}$-10^{-5} of the total mass of the system and we can assume $v_{CM,f} \cong v_{CM,i}$.

Using Eq. A.10 one obtains the relation between the angles in the laboratory and centre-of-mass systems:

$$\tan\theta_b = \frac{\sin\theta_C}{\cos\theta_C + \gamma} \qquad (A.12)$$

where γ is the ratio of the velocities of the centre of mass and of the particle b in the centre-of-mass frame of reference:

$$\gamma = \frac{v_{CM}}{v'_b} = \sqrt{\frac{m_a m_b}{m_A m_B} \frac{K_a}{(1 + m_a/m_A)Q + K_a}} \qquad (A.13)$$

The second equality has been derived using Eq. A.2.

Appendix B. PTOLEMY input files

We show here the input files used for the PTOLEMY calculations described in §2.4 and §6.8. The main keywords are:

- `REACTION`: specifies entrance and exit channel of the reaction, as well as the beam energy and the the energy, spin and parity of the excited state
- `BETA` or `BELX`: specifies the deformation parameter or the reduced transition strength for the excited state
- `PRINT`: sets the verbosity level of the output
- `PARAMETERSET`: sets a number of parameters used for controlling the calculations (such as various cutoffs) with the appropriate values
- `LSTEP`: if different than 1, only some partial wave functions are calculated and the rest are interpolated
- `ANGLEMIN`, `ANGLEMAX`, `ANGLESTEP`: specifies the range of scattering angles (in the centre-of-mass frame of reference) for which to perform the calculation
- `INCOMING`, `OUTGOING`: specifies the parameters of the optical potentail for the incoming and outgoing distorted waves

The first ";" means that the description of the incoming elastic potential is complete, the second that the outgoing potential is equal to the incoming, and the third that all parameters are specified and that the code can start calculating the scattering amplitudes.

pto_208Pb_17O_20AMeV_GQR.in

```
HEADER: INELASTIC
REACTION: 208PB(17O, 17O)208PB(2+ 11.0) ELAB = 340.
BETA=0.081
PRINT = 2
PARAMETERSET INELOCA1
LSTEP=1
ANGLEMIN= 0 ANGLEMAX= 20 ANGLESTEP=0.1
INCOMING
V=60 R0=1.17 A=0.665
```

```
VI=38. RI0=1.17 AI=0.665
RC0=1.2
;
OUTGOING
;
;
END
```

pto_208Pb_17O_20AMeV_pygmy_5512_B1.in

```
HEADER: INELASTIC
REACTION: 208PB(17O, 17O)208PB(1- 5.512) ELAB = 340.
BELX=1.0
PRINT = 2
PARAMETERSET INELOCA1
LSTEP=1
ANGLEMIN= 8 ANGLEMAX= 26 ANGLESTEP=0.1
INCOMING
V=60.0 R0=1.17 A=0.67
VI=38.0 RI0=1.17 AI=0.67
RC0=1.2
;
OUTGOING
;
;
END
```

Appendix C. Sorting code

This appendix will discuss the structure of the sorting code that was developed specifically for this thesis work. The code was written in C++ and is based on the ROOT software package, see [97], [98] for a reference guide on the various ROOT classes referenced in this appendix.

The code processes all the events of a given dataset, calibrates the ancillary detectors, performs a selection on the events of physical interest, and fills the 1D spectra and 2D matrices used for the interpretation of the data.

The analysis is performed by executing the ROOT macro `RunSort.C`, which takes care of opening the input files (produced by the Narval emulator) corresponding to the desired dataset and of processing them as defined by the `Sort` class, which is inherits from the ROOT `TSelector` class.

The code makes use of some helper classes, in particular the `Event` class which holds all the data acquired for an event, the `AssignationManager` class that applies a lookup table to the ancillary data, and the `CalibrationManager` class that applies calibration and drift correction to the ancillary data. The structure of the input `TTree` and of the various classes used by our code will now be described in more detail.

C.1. The input data

The `TTree` ROOT class is used to store list-mode data in a memory-efficient way. A tree is divided in a number of branches, corresponding to various data read event-by-event in the `Sort::Process` method. The branches of the tree used as input for our analysis code are:

- `EventNumber`: identification number of the event
- `TimeStamp`: timestamp of the event
- `lenrawBuf`: length of the `rawBuf` array, is always `358` in our case

- `rawBuf[358]`: array containing all the data words read from the VME crate
- `has_rawBuf`: flag for the `rawBuf` array, if false the data in `rawBuf` have no meaning
- `rawBufTstamp[1]`: 1-dimensional array with the timestamp of the AGAVA module
- `number_of_gammas`: number of gamma-rays reconstructed by the tracking; the following arrays contain values relative to all the reconstructed gammas, and the values after `number_of_gammas` have no meaning
- `gammaE[max_n_Agata_Gamma]`: energy of the reconstructed gamma-rays
- `gammaT[max_n_Agata_Gamma]`: start time of the gamma-rays obtained with a linear interpolation
- `gammaTstamp[max_n_Agata_Gamma]`: timestamp associated to the gamma-rays
- `gammaTrType[max_n_Agata_Gamma]`: interaction used to reconstruct the gamma-ray (1=photoelectric, 2=Compton, 3=pair production)
- `gammaX1[max_n_Agata_Gamma]`: x coordinate of the 1st interaction point
- `gammaY1[max_n_Agata_Gamma]`: y coordinate of the 1st interaction point
- `gammaZ1[max_n_Agata_Gamma]`: z coordinate of the 1st interaction point
- `gammaX2[max_n_Agata_Gamma]`: x coordinate of the 2nd interaction point
- `gammaY2[max_n_Agata_Gamma]`: y coordinate of the 2nd interaction point
- `gammaZ2[max_n_Agata_Gamma]`: z coordinate of the 2nd interaction point
- `number_of_hits`: number of interaction points reconstructed by the PSA; the following arrays contain values relative to all the interaction points, and the values after `number_of_hits` have no meaning
- `hitE[max_n_Agata_Hits]`: energy deposition
- `hitX[max_n_Agata_Hits]`: x coordinate
- `hitY[max_n_Agata_Hits]`: y coordinate
- `hitZ[max_n_Agata_Hits]`: z coordinate
- `hitT[max_n_Agata_Hits]`: start time obtained with a linear interpolation
- `hitTstamp[max_n_Agata_Hits]`: timestamp
- `hitId[max_n_Agata_Hits]`: identification number of the crystal in which the interaction is detected

- `hitSg[max_n_Agata_Hits]`: identification number of the segment in which the interaction is detected

C.2. THE EVENT CLASS

This class is basically a simple data structure, holding all the values measured by all detectors for a specific event. The Reset method of the class is used to zero all the data from one event before reading the next. Each detector is defined by its own class, whose members reflect the information that is read out from that detector. An helper class called `Si_id` is used to identify a TRACE pad in terms of its position.

For consistency, the `Event` class contains also structures for the AGATA data, even though they are already present as branches of the `TTree`. This means that during the `Sort::Process` method, before evaluating the logic conditions of the AGATA data, the energies, times, and positions of each reconstructed gamma-ray are copied in the event structure. Note that for the time information the operations described in §6.2 are performed at this point.

C.3. THE ASSIGNATIONMANAGER CLASS

The ancillary data are treated by the AGATA DAQ as a whole block, which is written in the output `TTree` as an array called `rawBuf`. This array corresponds to the data words read from all the channels of all VME boards (ADCs and TDCs).

The `AssignationManager` class implements a lookup table for the ancillary detectors: it associates each element of the `rawBuf` array to the corresponding detector, be it one pad of the Si telescopes or a scintillator. The Init method, called by `Sort::Begin`, loads the lookup tables from disk. At the beginning of `Sort::Process`, the `rawBuf` array is passed as the `data` argument of the `Assign` method, which fills an `Event` instance with the correct data.

C.4. THE CALIBRATIONMANAGER CLASS

This class applies a calibration and, if needed, a drift correction, to all the ancillary detectors. Note that the ancillary data in the `TTree` are always raw, and the calibration is performed every time a sort is performed. While it would be possible

to have the NARVAL emulator perform the calibration and write calibrated data to the `TTree`, or to write a new `TTree` with the calibrated data, the performance increase was found rather small, and we decided to keep this more flexible solution.

The `Init` method, called by `Sort::Begin`, loads the calibration coefficients from disk, using the global variables `Si_setting` and `scint_setting` to determine whether to use the values for the ^{208}Pb or the ^{90}Zr measurements. The `Calibrate` method, called by `Sort::Process`, reads the raw values from an `Event` object and writes them to another `Event` object (note that the two can also be the same instance of the `Event` class).

The drift correction is applied by rescaling the slope calibration coefficient of the detectors that need it (indicated by `list_of_pads_drift`) every `block_size` events, where `block_size` is the ratio between the number of events for the dataset and the number of blocks in which it is divided (50 for both ^{208}Pb and ^{90}Zr datasets).

The definition of the `CalibrationManager` class was left inside the `Sort.h` and `Sort.C` files.

C.5. THE SORT CLASS

The `Sort` class has 5 main methods, inherited from `TSelector`:

- `Begin` and `SlaveBegin`, which perform the pre-loop operations such as opening the output file, instantiating the histograms, reading the calibration coefficients and the 2D gates from disk, and so on. If using PROOF (Parallel ROOT Facility, an extension of ROOT allowing to perform the analysis in parallel on computer clusters or multi-core computers), `Begin` is called only on the master node, while `SlaveBegin` is called on all the nodes.
- `Process`, which performs all the loop operation; in our code, it is roughly divided in two parts: a "logic" section in which it is determined if the event is good or has to be rejected, and a "fill" section in which all histograms are incremented
- `Terminate` and `SlaveTerminate`, which take care of the post-loop operations, namely writing the histograms to an output file.

At the beginning of `Sort.C`, some global Boolean variables are declared, each determining if a certain gating condition is in use or not. In `Sort::Begin` the name of the output file is built in such a way that it reflects which conditions are in use. There are two types of conditions:

- conditions relative to the event as a whole, such as the requirement that at least one ^{17}O ion is detected in the Si telescopes; if such a condition is "in use" , the whole event is discarded if it does not satisfy such condition.
- conditions relative to a specific detector, such as the requirement that a gamma-ray is detected in a certain time window: if such a condition is "in use" , only the specific detector that does not satisfy the condition is discarded.

At the beginning of `Sort::Process`, all conditions are evaluated, and the event is discarded if any "global" condition in use is not satisfied. If the event has not been discarded, all histograms are filled: in this way all histograms are under the same global conditions. Detector-level gates in use are applied at this point.

Two global variables, called `Si_setting` and `scint_setting`, are used to know if the dataset under analysis corresponds to the ^{208}Pb or to the ^{90}Zr target, and what were the corresponding settings for Si and scintillator detectors. The variables are set at the beginning of `Sort::Begin` by the `determine_setting` function, using the name of the run, passed by the `RunSort` macro, to determine the appropriate values.

Due to the large number of channels of the Si detector pads, and the fact than only a part of those pads was in good working conditions, a list of what pads are in use is read in `Sort::Begin`; what list is to be used out of several possible is specified in the `RunSort` macro. In this way, the only histograms to be instantiated are those corresponding to the pads in use, saving a large quantity of memory.

C.6. THE RUNSORT MACRO

The NARVAL emulator produces one or more ROOT files for each run of the experiment. In this macro, all the files associated with a single run specified by the

variable `runnumber` (if the Boolean variable `use_list` is false) or to all the runs specified in a text file (if `use_list` is true) are added to a `TChain` object.

The data are processed by calling the `TChain::Process` method, whose first argument is the `TSelector` to be used for the analysis (defined in the file `Sort.C`), and the second is a comment string, which contains in our case information about which input files were used, the total number of events, and what pads to use for the sorting (all the pads that should be acquired, only those working correctly, etc, as specified by `pads_list`.).

C.7. STEP-BY-STEP FLOW OF THE CODE

Schematically, the code passes through the following steps:

`RunSort`

1. the code for the `Event` and `AssignationManager` classes is compiled and dynamically linked
2. the path in which the input files will be found is defined
3. the list of pads to use for the analysis is defined
4. a `TChain` object is instantiated
5. the run to analyse if not using a list of runs is defined
6. if using a list, the file containing the list is opened and all the corresponding runs are added to the `TChain`
7. if not using the list, the run defined above is added to the `TChain`
8. an options string is formed, with information about the input data
9. the `Process` method of the `TChain` is called: the file `Sort.C` is compiled and dynamically linked, and the data are processed

`Sort::Begin`

10. the options from `RunSort` are read
11. the ouput file name is built and the file is opened
12. the list of pads in use is read
13. the 2D cuts are read
14. the Si detector coordinates are read

`Sort::SlaveBegin`

15. `AssignationManager` object `am` and `CalibrationManager` object `cm` (if `CAL` is defined) are instantiated
16. all histogram objects are instantiated

`Sort::Process`

17. the values for the current event are read by calling Sort::GetEntry
18. lookup table is applied by calling the `am->Assign` method
19. if `CAL` is defined, calibration is applied by calling the `cm->Calibrate` method
20. all logic conditions are evaluated and stored in Boolean variables
21. global conditions are applied: if any condition in use is false the event is discarded
22. histograms are filled
23. event structure is cleared
24. the program goes on to process the next event until the end of the file

`Sort::Terminate`

25. subfolders for each detector are created in the output file
26. histograms are written in the appropriate subfolder of the output file
27. output file is closed, cleanup of remaining objects

Bibliography

[1] P. F. Bortignon, A. Bracco, and R. Broglia, *Giant Resonances: Nuclear Structure at Finite Temperature*. Amsterdam: Harwood Academic Publishers, 1998.

[2] M. N. Harakeh and A. van der Woude, *Giant Resonances: Fundamental High-Frequency Modes of Nuclear Excitation*. Oxford University Press, USA, 2001.

[3] W. Bothe and W. Gentner, "Atomumwandlungen durch g-Strahlen," *Zeitschrift für Physik*, vol. 106, pp. 236-248, Mar. 1937.

[4] M. Goldhaber and E. Teller, "On Nuclear Dipole Vibrations," *Physical Review*, vol. 74, no. 9, pp. 1046-1049, Nov. 1948.

[5] H. Steinwedel and J. H. D. Jensen, "Hydrodynamik von Kerndipolschwingungen," *Zeitschrift Naturforschung Teil A*, vol. 5, p. 413, 1950.

[6] E. Lipparini and S. Stringari, "Sum rules and giant resonances in nuclei," *Physics Reports*, vol. 175, no. 3-4, pp. 103-261, Apr. 1989.

[7] G. Kühler et al., "Electroexcitation of 208Pb, distribution of electric dipole and quadrupole strength and fragmentation of the isoscalar quadrupole giant resonance," *Physics Letters B*, vol. 104, no. 3, pp. 189-193, Aug. 1981.

[8] S. Kamerdzhiev, J. Lisantti, P. von Neumann-Cosel, A. Richter, G. Tertychny, and J. Wambach, "Fine structure of the giant isoscalar quadrupole resonance in 208Pb observed in high-resolution (e,e') and (p,p') experiments," *Physical Review C*, vol. 55, no. 4, pp. 2101-2104, Apr. 1997.

[9] A. Shevchenko et al., "Global investigation of the fine structure of the isoscalar giant quadrupole resonance," *Physical Review C*, vol. 79, no. 4, p. 044305, Apr. 2009.

[10] A. Richter, "Giant resonances — experiments at highest resolution, wavelets and scales," *Progress in Particle and Nuclear Physics*, vol. 55, pp. 387-396, Jul. 2005.

[11] D. E. Bainum et al., "Observation of Giant Particle-Hole Resonances in 90Zr(p, n)90Nb," *Physical Review Letters*, vol. 44, no. 26, pp. 1751-1754, Jun. 1980.

[12] S. Strauch et al., "Giant Resonances in the Doubly Magic Nucleus 48Ca from the (e,e'n) Reaction," *Physical Review Letters*, vol. 85, no. 14, pp. 2913-2916, Oct. 2000.

[13] P. von Neumann-Cosel et al., "Spin and Orbital Magnetic Quadrupole Resonances in 48Ca and 90Zr from 180° Electron Scattering," *Physical Review Letters*, vol. 82, no. 6, pp. 1105-1108, Feb. 1999.

[14] Y. Kalmykov et al., "Fine Structure of the Gamow-Teller Resonance in 90Nb and Level Density of 1+ States," *Physical Review Letters*, vol. 96, no. 1, p. 012502, Jan. 2006.
[15] A. Shevchenko et al., "Fine Structure in the Energy Region of the Isoscalar Giant Quadrupole Resonance: Characteristic Scales from a Wavelet Analysis," *Physical Review Letters*, vol. 93, no. 12, p. 122501, 2004.
[16] H. Aiba, M. Matsuo, S. Nishizaki, and T. Suzuki, "Fluctuation properties of strength functions associated with giant resonances," *Physical Review C*, vol. 68, no. 5, p. 054316, Nov. 2003.
[17] H. Aiba and M. Matsuo, "Scaling analysis of the fluctuating strength function," *Physical Review C*, vol. 60, no. 3, p. 034307, 1999.
[18] D. Lacroix and P. Chomaz, "Multiscale fluctuations in the nuclear response," *Physical Review C*, vol. 60, no. 6, p. 064307, Nov. 1999.
[19] D. Lacroix, A. Mai, P. von Neumann-Cosel, A. Richter, and J. Wambach, "Multiple scales in the fine structure of the isoscalar giant quadrupole resonance in 208Pb," *Physics Letters B*, vol. 479, no. 1-3, pp. 15-20, Apr. 2000.
[20] A. Shevchenko et al., "Analysis of fine structure in the nuclear continuum," *Physical Review C*, vol. 77, no. 2, p. 024302, Feb. 2008.
[21] O. Wieland et al., "Search for the Pygmy Dipole Resonance in 68Ni at 600 MeV/nucleon," *Physical Review Letters*, vol. 102, no. 9, p. 092502, Mar. 2009.
[22] P. Adrich et al., "Evidence for Pygmy and Giant Dipole Resonances in 130Sn and 132Sn," *Physical Review Letters*, vol. 95, no. 13, p. 132501, 2005.
[23] A. Klimkiewicz et al., "Dipole response of neutron-rich Sn isotopes," *Nuclear Physics A*, vol. 788, no. 1-4, pp. 145-152, May 2007.
[24] A. Carbone et al., "Constraints on the symmetry energy and neutron skins from pygmy resonances in 68Ni and 132Sn," *Physical Review C*, vol. 81, no. 4, p. 041301, Apr. 2010.
[25] J. Piekarewicz, "Pygmy dipole resonance as a constraint on the neutron skin of heavy nuclei," *Physical Review C*, vol. 73, no. 4, p. 044325, Apr. 2006.
[26] I. Daoutidis and S. Goriely, "Impact of the nuclear symmetry energy on the pygmy dipole resonance," *Physical Review C*, vol. 84, no. 2, p. 027301, 2011.
[27] S. Goriely, "Radiative neutron captures by neutron-rich nuclei and the r-process nucleosynthesis," *Physics Letters B*, vol. 436, no. 1-2, pp. 10-18, Sep. 1998.
[28] S. Goriely and E. Khan, "Large-scale QRPA calculation of E1-strength and its impact on the neutron capture cross section," *Nuclear Physics A*, vol. 706, no. 1-2, pp. 217-232, Jul. 2002.
[29] S. Goriely, "The r-process nucleosynthesis: a continued challenge for nuclear physics," *Nuclear Physics A*, vol. 718, pp. 287-294, May 2003.
[30] T. Hartmann, J. Enders, P. Mohr, K. Vogt, S. Volz, and A. Zilges,

"Measurement of the Dipole and Electric Quadrupole Strength Distributions up to 10 MeV in the Doubly Magic Nuclei 40Ca and 48Ca," *Physical Review Letters*, vol. 85, no. 2, pp. 274-277, 2000.
[31] R. Schwengner et al., "Dipole response of 88Sr up to the neutron-separation energy," *Physical Review C*, vol. 76, no. 3, p. 034321, 2007.
[32] D. Vretenar, N. Paar, P. Ring, and G. Lalazissis, "Pygmy dipole resonances in the relativistic random phase approximation," *Physical Review C*, vol. 63, no. 4, Feb. 2001.
[33] D. Savran et al., "Fine Structure of the Pygmy Dipole Resonance in Xe136," *Physical Review Letters*, vol. 100, no. 23, Jun. 2008.
[34] N. Ryezayeva et al., "Nature of Low-Energy Dipole Strength in Nuclei: The Case of a Resonance at Particle Threshold in 208Pb," *Physical Review Letters*, vol. 89, no. 27, Dec. 2002.
[35] T. Shizuma et al., "Fine structure of the magnetic-dipole-strength distribution in 208Pb," *Physical Review C*, vol. 78, no. 6, p. 061303, Dec. 2008.
[36] D. Savran et al., "Nature of the Pygmy Dipole Resonance in 140Ce Studied in (α,α'γ) Experiments," *Physical Review Letters*, vol. 97, no. 17, p. 172502, Oct. 2006.
[37] D. Savran et al., "Investigation of the Pygmy Dipole Resonance in (α,α'γ) coincidence experiments," *Nuclear Physics A*, vol. 788, no. 1-4, pp. 165-170, 2007.
[38] J. Endres et al., "Splitting of the pygmy dipole resonance in 138Ba and 140Ce observed in the (α,α'γ) reaction," *Physical Review C*, vol. 80, no. 3, Sep. 2009.
[39] J. Endres et al., "Isospin Character of the Pygmy Dipole Resonance in 124Sn," *Physical Review Letters*, vol. 105, no. 21, Nov. 2010.
[40] N. Paar, Y. F. Niu, D. Vretenar, and J. Meng, "Isoscalar and Isovector Splitting of Pygmy Dipole Structures," *Physical Review Letters*, vol. 103, no. 3, p. 032502, Jul. 2009.
[41] E. G. Lanza, A. Vitturi, M. V. Andrés, F. Catara, and D. Gambacurta, "Excitations of pygmy dipole resonances in exotic and stable nuclei via Coulomb and nuclear fields," *Physical Review C*, vol. 84, no. 6, p. 064602, Dec. 2011.
[42] R. Mohan, M. Danos, and L. C. Biedenharn, "Three-Fluid Hydrodynamical Model of Nuclei," *Physical Review C*, vol. 3, no. 5, pp. 1740-1749, May 1971.
[43] H. Steinwedel, J. H. D. Jensen, and P. Jensen, "Nuclear Dipole Vibrations," *Physical Review*, vol. 79, no. 6, p. 1019, 1950.
[44] H. Steinwedel and J.H.D. Jensen, *Zeitschrift für Naturforschung A*, vol. 5, p. 413, 1950.
[45] Y. Suzuki, K. Ikeda, and H. Sato, "New Type of Dipole Vibration in Nuclei," *Progress of Theoretical Physics*, vol. 83, pp. 180-184, Feb. 1990.

[46] J. Chambers, E. Zaremba, J. P. Adams, and B. Castel, "Pygmy dipole resonances in the calcium isotopes," *Physical Review C*, vol. 50, no. 6, p. R2671-R2674, Dec. 1994.
[47] J. P. Adams, B. Castel, and H. Sagawa, "Neutron halos and E1 resonances in 208Pb," *Physical Review C*, vol. 53, no. 2, pp. 1016-1017, Feb. 1996.
[48] G. Bertsch and J. Foxwell, "Dipole strength function in 11Li," *Physical Review C*, vol. 41, no. 3, pp. 1300-1302, Mar. 1990.
[49] F. Catara, E. G. Lanza, M. A. Nagarajan, and A. Vitturi, "Effect of large neutron excess on the dipole response in the region of the giant dipole resonance," *Nuclear Physics A*, vol. 624, no. 3, pp. 449-458, Oct. 1997.
[50] T. Hartmann et al., "Microscopic Nature of the Pygmy Dipole Resonance: The Stable Ca Isotopes," *Physical Review Letters*, vol. 93, no. 19, Nov. 2004.
[51] S. Volz et al., "The photoresponse of stable N=82N=82 nuclei below 10 MeV," *Nuclear Physics A*, vol. 779, pp. 1-20, 2006.
[52] N. Paar, D. Vretenar, E. Khan, and G. Colò, "Exotic modes of excitation in atomic nuclei far from stability," *Reports on Progress in Physics*, vol. 70, pp. 691-793, May 2007.
[53] N. Paar, P. Ring, T. Nikšić, and D. Vretenar, "Quasiparticle random phase approximation based on the relativistic Hartree-Bogoliubov model," *Physical Review C*, vol. 67, no. 3, p. 034312, Mar. 2003.
[54] I. Daoutidis and P. Ring, "Relativistic continuum quasiparticle random-phase approximation in spherical nuclei," *Physical Review C*, vol. 83, no. 4, p. 044303, Apr. 2011.
[55] E. Litvinova, P. Ring, and V. Tselyaev, "Relativistic quasiparticle time blocking approximation: Dipole response of open-shell nuclei," *Physical Review C*, vol. 78, no. 1, p. 014312, Jul. 2008.
[56] E. G. Lanza, F. Catara, D. Gambacurta, M. V. Andrés, and P. Chomaz, "Multiphonon excitations and pygmy resonances in tin isotopes," *Physical Review C*, vol. 79, no. 5, p. 054615, May 2009.
[57] M. H. Macfarlan and S. C. Pieper, "PTOLEMY a program for Heavy-ion Direct reaction Calculation," *Argonne National Laboratory*, 1978.
[58] M. Rhoades-Brown, M. H. Macfarlane, and S. C. Pieper, "Techniques for heavy-ion coupled-channels calculations. I. Long-range Coulomb coupling," *Physical Review C*, vol. 21, no. 6, p. 2417, Jun. 1980.
[59] M. Rhoades-Brown, M. H. Macfarlane, and S. C. Pieper, "Techniques for heavy-ion coupled-channels calculations. II. Iterative solution of the coupled radial equations," *Physical Review C*, vol. 21, no. 6, p. 2436, Jun. 1980.
[60] F. E. Bertrand, J. R. Beene, and D. J. Horen, "Heavy ion excitation of giant resonances -- The next generation," *Nuclear Physics A*, vol. 482, no. 1-2, pp. 287-303, May 1988.
[61] T. P. Sjoreen et al., "Inelastic excitation of giant resonances by 400-MeV

16O," *Physical Review C*, vol. 29, no. 4, p. 1370, Apr. 1984.
[62] J. R. Beene et al., "Heavy-ion excitation and photon decay of giant resonances in 208Pb," *Physical Review C*, vol. 39, no. 4, p. 1307, Apr. 1989.
[63] J. R. Beene et al., "Heavy-ion Coulomb excitation and photon decay of the giant dipole resonance in 208Pb," *Physical Review C*, vol. 41, no. 3, p. 920, Mar. 1990.
[64] M. Jääskeläinen et al., "The spin spectrometer: Design, instrumentation and response characteristics of 4π γ-ray multidetector system," *Nuclear Instruments and Methods in Physics Research*, vol. 204, no. 2-3, pp. 385-405, Jan. 1983.
[65] A. Gadea et al., "Conceptual design and infrastructure for the installation of the first AGATA sub-array at LNL," *Nuclear Instruments and Methods in Physics Research Section A: Accelerators, Spectrometers, Detectors and Associated Equipment*, vol. 654, pp. 88-96, Oct. 2011.
[66] S. Akkoyun et al., "AGATA—Advanced GAmma Tracking Array," *Nuclear Instruments and Methods in Physics Research Section A: Accelerators, Spectrometers, Detectors and Associated Equipment*, no. 0, 2011.
[67] G. R. Satchler, *Introduction to Nuclear Reactions*, 2nd ed. Oxford: Oxford University Press, USA, 1990.
[68] G. R. Satchler, *Direct Nuclear Reactions*. Oxford: Oxford University Press, 1983.
[69] Puglierin G., "Accelerator facilities for pure and applied physics at Legnaro Italian Nuclear Physics National Lab," *Nuclear Physics A*, vol. 834, no. 1-4, p. 713c-716c, 2010.
[70] D. Bazzacco, "The Advanced Gamma Ray Tracking Array AGATA," *Nuclear Physics A*, vol. 746, pp. 248-254, Dec. 2004.
[71] A. M. Stefanini et al., "The heavy-ion magnetic spectrometer PRISMA," *Nuclear Physics A*, vol. 701, no. 1-4, pp. 217-221, Apr. 2002.
[72] X. Grave, R. Canedo, J.-F. Clavelin, S. Du, and E. Legay, "NARVAL a modular distributed data acquisition system with Ada 95 and RTAI," in *Real Time Conference, 2005. 14th IEEE-NPSS*, 2005.
[73] http://www.sparrowcorp.com/products/software, "Kmax - Advanced Tools for Industry, Education and Research." .
[74] E. Farnea et al., "Conceptual design and Monte Carlo simulations of the AGATA array," *Nuclear Instruments and Methods in Physics Research Section A: Accelerators, Spectrometers, Detectors and Associated Equipment*, vol. 621, no. 1-3, pp. 331-343, 2010.
[75] J. Simpson, "The Euroball Spectrometer," *Zeitschrift für Physik A Hadrons and Nuclei*, vol. 358, pp. 139-143, Jul. 1997.
[76] A. Georgiev, W. Gast, and R. M. Lieder, "An analog-to-digital conversion based on a moving windowdeconvolution," *IEEE Transactions on Nuclear*

Science, vol. 41, no. 4, pp. 1116-1124, Aug. 1994.
[77] F. Recchia et al., "Position resolution of the prototype AGATA triple-cluster detector from an in-beam experiment," *Nuclear Instruments and Methods in Physics Research Section A: Accelerators, Spectrometers, Detectors and Associated Equipment*, vol. 604, no. 3, pp. 555-562, Jun. 2009.
[78] A. Olariu, P. Desesquelles, C. Diarra, P. Medina, C. Parisel, and C. S. O. . Collaboration, "Pulse shape analysis for the location of the γ-interactions in AGATA," *IEEE Transactions on Nuclear Science*, vol. 53, no. 3, pp. 1028- 1031, Jun. 2006.
[79] T. Kröll and D. Bazzacco, "A genetic algorithm for the decomposition of multiple hit events in the -ray tracking detector MARS," *Nuclear Instruments and Methods in Physics Research Section A: Accelerators, Spectrometers, Detectors and Associated Equipment*, vol. 565, no. 2, pp. 691-703, Sep. 2006.
[80] F. C. L. Crespi et al., "A pulse shape analysis algorithm for HPGe detectors," *Nuclear Instruments and Methods in Physics Research Section A: Accelerators, Spectrometers, Detectors and Associated Equipment*, vol. 570, no. 3, pp. 459-466, Jan. 2007.
[81] A. J. Boston et al., "Gamma-ray tracking: Characterisation of the AGATA symmetric prototype detectors," *Nuclear Instruments and Methods in Physics Research Section B: Beam Interactions with Materials and Atoms*, vol. 261, no. 1-2, pp. 1098-1102, Aug. 2007.
[82] K. Vetter et al., "Three-dimensional position sensitivity in two-dimensionally segmented HP-Ge detectors," *Nuclear Instruments and Methods in Physics Research Section A: Accelerators, Spectrometers, Detectors and Associated Equipment*, vol. 452, no. 1-2, pp. 223-238, Sep. 2000.
[83] I. Kojouharov, S. Tashenov, T. Engert, J. Gerl, and H. Schaffner, "The GSI HPGe detector scanner - a sophisticated device based on PET technique," in *IEEE Nuclear Science Symposium Conference Record, 2007. NSS '07*, 2007, vol. 3, pp. 2213-2215.
[84] T. Kröll and D. Bazzacco, "Simulation and analysis of pulse shapes from highly segmented HPGe detectors for the $\hat{I}^3$-ray tracking array MARS," *Nuclear Instruments and Methods in Physics Research Section A: Accelerators, Spectrometers, Detectors and Associated Equipment*, vol. 463, no. 1-2, pp. 227-249, May 2001.
[85] http://mgs2005.in2p3.fr/Mgs.php, "Mgs software." .
[86] F. C. L. Crespi et al., "HPGe detectors timing using pulse shape analysis techniques," *Nuclear Instruments and Methods in Physics Research Section A: Accelerators, Spectrometers, Detectors and Associated Equipment*, vol. 620, no. 2-3, pp. 299-304, 2011.
[87] J. van der Marel and B. Cederwall, "Backtracking as a way to reconstruct Compton scattered γ-rays," *Nuclear Instruments and Methods in Physics*

Research Section A: Accelerators, Spectrometers, Detectors and Associated Equipment, vol. 437, no. 2-3, pp. 538-551, Nov. 1999.

[88] A. Lopez-Martens, K. Hauschild, A. Korichi, J. Roccaz, and J.-P. Thibaud, "γ-ray tracking algorithms: a comparison," *Nuclear Instruments and Methods in Physics Research Section A: Accelerators, Spectrometers, Detectors and Associated Equipment*, vol. 533, no. 3, pp. 454-466, Nov. 2004.

[89] R. Nicolini et al., "Investigation of the properties of a 1''×1'' LaBr3:Ce scintillator," *Nuclear Instruments and Methods in Physics Research Section A: Accelerators, Spectrometers, Detectors and Associated Equipment*, vol. 582, no. 2, pp. 554-561, Nov. 2007.

[90] F. Camera et al., "Investigation of the self activity and high energy γ-rays response of a 1" × 1" and 3" × 3" LaBr3:Ce scintillators," in *IEEE Nuclear Science Symposium Conference Record, 2007. NSS '07*, 2007, vol. 2, pp. 1386-1388.

[91] F. C. L. Crespi et al., "Alpha-gamma discrimination by pulse shape in LaBr3:Ce and LaCl3:Ce," *Nuclear Instruments and Methods in Physics Research Section A: Accelerators, Spectrometers, Detectors and Associated Equipment*, vol. 602, no. 2, pp. 520-524, Apr. 2009.

[92] F. Birocchi et al., "Position sensitivity of large volume LaBr3:Ce detectors," in *2009 IEEE Nuclear Science Symposium Conference Record (NSS/MIC)*, 2009, pp. 1403-1405.

[93] N. Blasi et al., "Analysis and first order correction of signal saturation effects in photomultiplier tubes for improved estimation of interacting radiation energy in Lanthanum bromide scintillators," in *2010 IEEE Nuclear Science Symposium Conference Record (NSS/MIC)*, 2010, pp. 1809-1812.

[94] F. Birocchi et al., "Position sensitivity in 3" × 3" LaBr3:Ce scintillators," in *2010 IEEE Nuclear Science Symposium Conference Record (NSS/MIC)*, 2010, pp. 198-200.

[95] A. Maj et al., "Angular distribution of photons from the delay of the GDR in hot and rotating light Yb nuclei from exclusive experiments," *Nuclear Physics A*, vol. 571, no. 1, pp. 185-220, Apr. 1994.

[96] C. Boiano, R. Bassini, F. Camera, B. Million, O. Wieland, and A. Giaz, "A 16 channel NIM module for a complete processing of fast scintillator signals," in *IEEE Nuclear Science Symposium Conference Record, 2008. NSS '08*, 2008, pp. 2068-2070.

[97] R. Brun and F. Rademakers, "ROOT - An object oriented data analysis framework," *Nuclear Instruments and Methods in Physics Research Section A: Accelerators, Spectrometers, Detectors and Associated Equipment*, vol. 389, no. 1-2, pp. 81-86, Apr. 1997.

[98] http://root.cern.ch/drupal/, "ROOT | A Data Analysis Framework." .

[99] O. Tarasov and D. Bazin, "LISE++: Radioactive beam production with in-

flight separators," *Nuclear Instruments and Methods in Physics Research Section B: Beam Interactions with Materials and Atoms*, vol. 266, no. 19-20, pp. 4657-4664, Oct. 2008.

[100] http://groups.nscl.msu.edu/lise/lise.html, "LISE++ : a simulation of fragment separators." .

[101] D. C. Radford, I. Ahmad, R. Holzmann, R. V. F. Janssens, and T. L. Khoo, "A prescription for the removal of Compton-scattered gamma rays from gamma-ray spectra," *Nuclear Instruments and Methods in Physics Research Section A: Accelerators, Spectrometers, Detectors and Associated Equipment*, vol. 258, no. 1, pp. 111-118, Jul. 1987.

[102] http://agata.pd.infn.it/documents/simulations/agataCode.html, "AGATA Simulation Code." .

[103] R. Schwengner et al., "Pygmy dipole strength in Zr90," *Physical Review C*, vol. 78, no. 6, Dec. 2008.

[104] H. Morinaga, *In-Beam Gamma-Ray Spectroscopy*. Elsevier Science Ltd, 1977.

[105] http://nrv.jinr.ru/nrv/webnrv/stat_model/default.php, "NRV: Decay of excited nuclei." .

Acknowledgements

No man is an island, and working on a nuclear physics experiment sure makes you realize that. There's very long list of people who made this experiment and its analysis possible, and I apologize to anyone who may have been left out.

First of all, I would like to thank my advisor, Prof. Angela Bracco, for the expert guidance she gave me throughout the years and for the independence she has granted me. As the end of this thesis also marks the end of my years with the gamma spectroscopy group of Milan, I would also like to thank Prof. Franco Camera for following me as an undergraduate, not such a long time ago, and for the help with the setup and with the scintillators. Many thanks also go to Prof. Silvia Leoni, for all the preparation work she's done before the experiment, and for all the help she's given me afterwards.

I am also in debt to Dr. Oliver Wieland, whose help was critical for obtaining the final results, and to the rest of the group; in particular, I thank Dr. Fabio Crespi and Luna Pellegri for their contribution to the data analysis. I would also like to acknowledge Ciro Boiano and Sergio Brambilla, as their expertise was fundamental.

I gratefully acknowledge the AGATA groups of Padova and Legnaro, who were very helpful both before the experiment for the preparations, and after the experiment for the analysis of the AGATA data; in particular, I thank Dr. Dino Bazzacco, Dr. Daniele Mengoni, Dr. Francesco Recchia, Dr. Enrico Farnea, Dr. Javier Valiente, Caterina Michelagnoli and Andrea Gottardo. I also thank Prof. Santo Lunardi for agreeing to referee this thesis and for the constructive comments.

Finally, I thank my family for supporting me through all these years, and my friends for all the good moments we've shared, because it's important to have a life outside the lab. And the most important thanks go to Agnese Giaz, for the help during the experiment and for always being there for me afterwards. Getting to know you is, for me, the most important result of the experiment.